ResearchGate

See discussions, stats, and author profiles for this publication at: https://www.researchgate.net/publication/251443201

Active Isolation and Damping of Vibrations via Stewart Platform

Article · January 2003

CITATIONS
30

READS
66

1 author:

Ahmed Mohammed Abu Hanieh
Birzeit University
30 PUBLICATIONS **229** CITATIONS

SEE PROFILE

All content following this page was uploaded by Ahmed Mohammed Abu Hanieh on 31 January 2014.

The user has requested enhancement of the downloaded file. All in-text references underlined in blue are added to the original document and are linked to publications on ResearchGate, letting you access and read them immediately.

Active Isolation and Damping of Vibrations via Stewart Platform

Ahmed Abu Hanieh

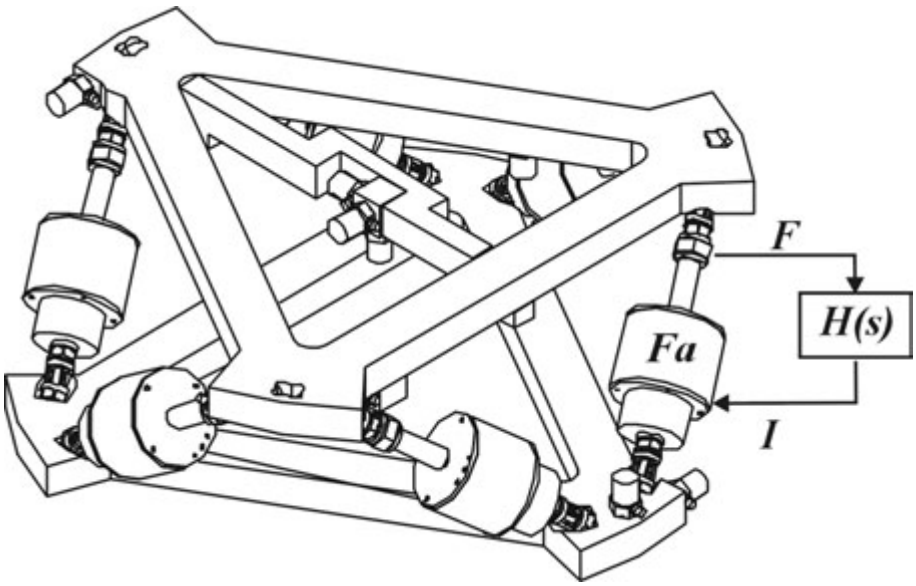

ULB

Active Structures Laboratory

2003

ULB

Université Libre de Bruxelles

Faculty of Applied Sciences

Active Isolation and Damping of Vibrations via Stewart Platform

Ahmed Abu Hanieh

April 2003

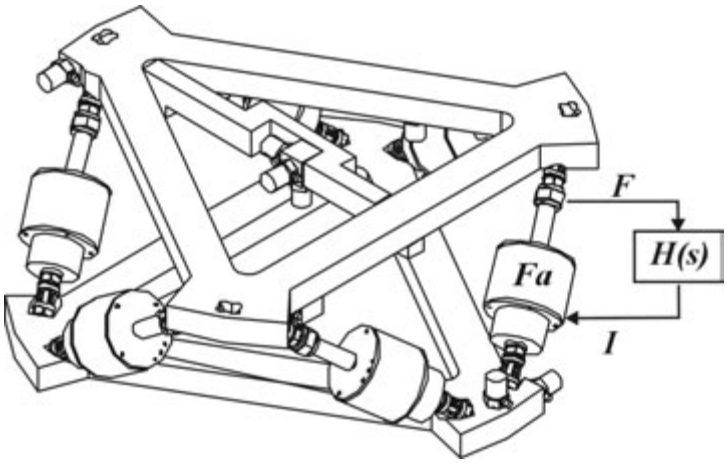

Thesis submitted in candidature for the degree of
Doctor in Applied Sciences
Academic year 2002 - 2003

Active Structures Laboratory
Department of Mechanical Engineering and Robotics

Acknowledgements

In the beginning, I would like to express my sincere gratitude to my supervisor professor André Preumont, the head of the *Active Structures Laboratory* for his patience, wise advices, brilliant ideas and suggestions and for his strong insistance and high pressure to achieve better work.

I would like to thank my colleagues: Frédéric Bossens for putting my feet on the right way, Mihaita Horodinca for his big efforts in manufacturing the Stewart platform, Vincent Piefort for his advices in the finite element modelling, Ioanica Burda and Salvator Dusabimana for their efforts in building the electronics needed for the flight test, Pierre De Man, Arnaud François, Ioan Doroftei and Xavier Pitoiset for their help and friendship. Special thanks to Mihaita and Ioanica for their support and participation in the parabolic flight test.

I am grateful to the team of Micromega Dynamics, in particular, Nicolas Loix, Jean Phillippe Verschueren and Serge Cattoul for their continuous help and cooperation and for their endless industrial and practical advices specially in the electronics.

I am also grateful to the other space and vibration isolation research groups who provided us with helpful ideas in the construction of the Stewart platform.

I am deeply thankful to my family in Palestine, particularly, my beloved mother and I send a ray of love and blessing to the memory of my father who died during the period of this work. The words are too little to describe my thanks to my wife and children for their patience and endless support to withstand the challenges of life and work.

Summary

In this work, we investigate the active vibration isolation and damping of sensitive equipment. Several single-axis isolation techniques are analyzed and tested. A comparison between the sky-hook damper, integral force feedback, inertial velocity feedback and Lag-Lead control techniques is conducted using several practical examples.

The study of single-axis systems has been developed and used to build a six-axis isolator. A six degrees of freedom *active isolator* based on Stewart platform has been designed manufactured and tested for the purpose of active vibration isolation of sensitive payloads in space applications. This six-axis hexapod is designed according to the cubic configuration; it consists of two triangular parallel plates connected to each other by six active legs orhtogonal to each other; each leg consists of a voice coil actuator, a force sensor and two flexible joints. Two different control techniques have been tested to control this isolator: integral force feedback and Lag-Lead compensator, the two techniques are based on force feedback and are applied in a decentralized manner. A micro-gravity parabolic flight test has been done to test the isolator in micro-gravity environment.

In the context of this research, another hexapod has been produced; a generic *active damping* and precision pointing interface based on Stewart platform. This hexapod consists of two parallel plates connected to each other by six active legs configured according to the cubic architecture. Each leg consists of an amplified piezoelectric actuator, a force sensor and two flexible joints. This Stewart platform is addressed to space applications where it aims at controlling the vibrations of space structures while connecting them rigidly. The control technique used here is the decentralized integral force feedback.

Contents

Chapter 1

Introduction

1.1 Motivation of the research

This research began at the Free University of Brussels (ULB), in the Active Structures Laboratory (ASL), in 1998 to find a solution for the six-degree-of-freedom vibration isolation and suppression. Both ground and space applications have been taken into account during this research.
Vibrations propagating into the mechanical systems can cause many problems at different levels causing performance degradation for sensitive systems [1]. The proposed solution in this work is to use a six-axis active hexapod based on Stewart platform configuration. The rigidity of the legs of this hexapod determines the application to be used for; a stiff hexapod, for example, is used as a rigid interface for active damping and precision pointing applications while a soft hexapod is used, in general, for the purpose of active isolation of vibrations. Notice here that introducing the appropriate design, soft Stewart platform can be used for both precision pointing and vibration isolation.
One should avoid the confusion between the definitions of damping and isolation of vibrations. In a few words, *damping* is defined as the reduction of the response amplitude of the system within a limited bandwidth near the natural frequencies of the system. Vibration *isolation* is defined as the attenuation of the response of the system after its corner frequency to cut-off all the disturbances after that frequency allowing all the signals below it to pass faithfully. The objective of this active vibration isolation research is to develop a generic modular 6 degrees of freedom (d.o.f) isolator for space applications. A similar project was developed at the Jet Propulsion Laboratory (JPL) in the mid '90s [2]. The objective of this project was to develop a generic multi-purpose 6 d.o.f. isolator with standardized architecture and voice coil actuators. The application considered is interferometry with independent pointing telescopes as represented in Fig.1.1.

1.2 Isolation objectives

The isolation objectives are illustrated in Fig.1.2; the ideal 6 d.o.f. isolation platform should transmit the attitude control torque within the bandwidth ω_c of the attitude control system and filter all the high frequency components coming from vibrating equipment

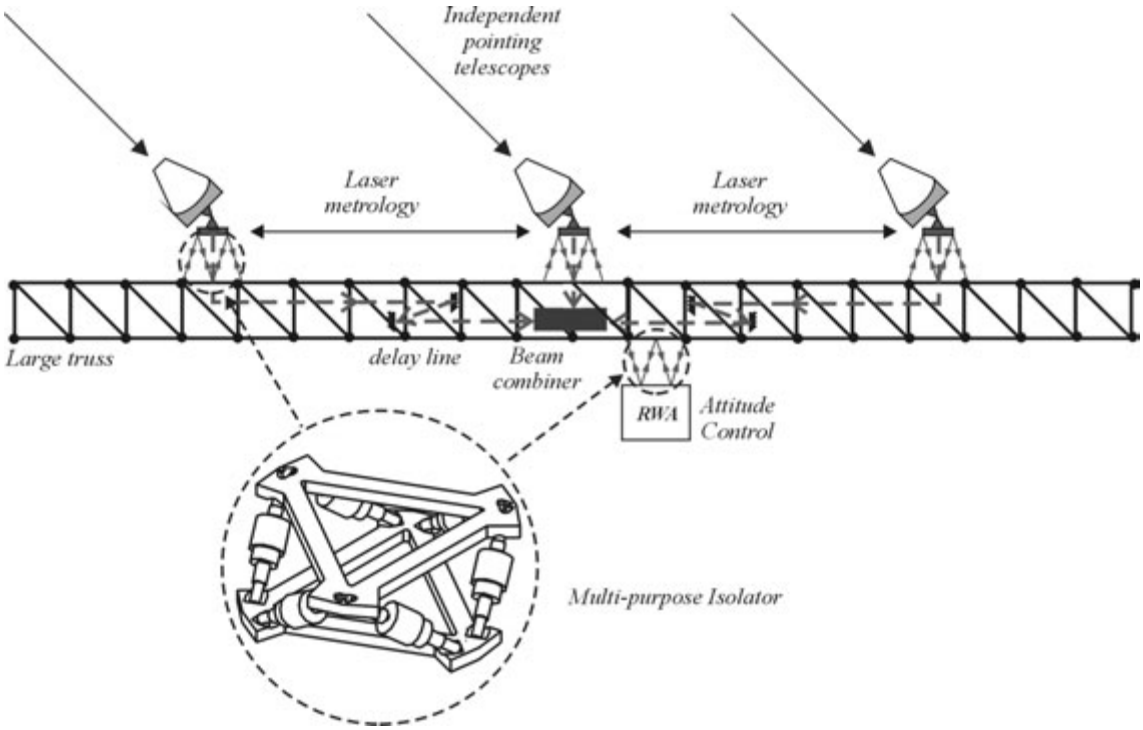

Figure 1.1: *Schematic view of a future interferometric mission and possible locations for a multi-purpose isolator*

above ω_c [3]. A single-axis active isolator combines a high attenuation rate in the roll-off region with no overshoot at the corner frequency as will be shown in the next chapters. To fully isolate two rigid bodies with respect to each other, we need six such isolators judiciously placed, that can be controlled either in a centralized or decentralized manner.

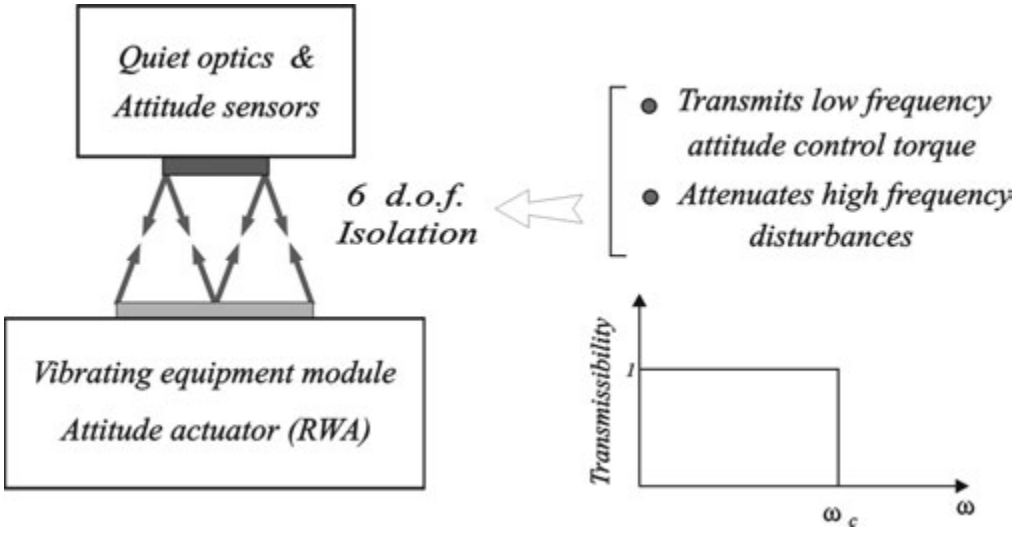

Figure 1.2: *Principle of the 6 d.o.f. vibration isolation and isolation objectives*

1.3 Various isolation architectures

There are two main cases where vibration isolation is necessary [4]:

- The operating equipment can generate an oscillating disturbance (force) propagating into the supporting structure.
- The disturbance can be generated by the supporting structure propagating into the sensitive equipment.

Car suspension can be considered as the most famous ground application of vibration isolation. Many researchers focused their attention on vibration control in car suspension to improve the riding comfort and to reduce the jerk effect on the body and components of the car [5]. Other examples can be found in machine tools and other precision machines. Machine tools need to function in high accuracy to achieve high precision in metal removal processes, this is why there is a need to have efficient vibration isolation between the machine and the noisy floor [6].
More attention in this research has been paid to sensitive optical payloads application. The main principle of vibration isolation of sensitive payloads is to place an isolation stage in the vibration transmission path (between the vibrating base and the sensitive payload) so as to prevent the transmission of high-frequency vibratory forces between them [7]. To discuss the concept of isolation in space applications, a review of the main ideas developed in [8, 9] can be done here. Two architectures are proposed to isolate the sensitive payload from the disturbing spacecraft carrier: multi-level actuation architecture and soft-mount architecture.

1.3.1 Multi level actuation architecture

The multi level actuation architecture is depicted in Fig.1.3. It consists of three layers:

1. A coarse gimbal mechanism which acts as a high-pass filter and compensates for major changes in attitude. Such a system passes all the disturbances beyond its control bandwidth.
2. A soft mount dynamic isolation acting as a low-pass filter to isolate the disturbances coming from the carrier. This can be achieved with flexural blades or magnetic suspension (e.g. [10, 11])
3. An image motion compensation mechanism consisting of fast steering mirrors for high bandwidth filter rejection.

1.3.2 Soft mount architecture

The soft mount architecture approach consists of interchanging the coarse gimbal and the dynamic isolation of the multi level actuation architecture (Fig.1.4). The corner frequency of the dynamic isolation is chosen as low as practically possible (at the limit, if the stiffness of the soft mount is zero, the payload is a free flyer).

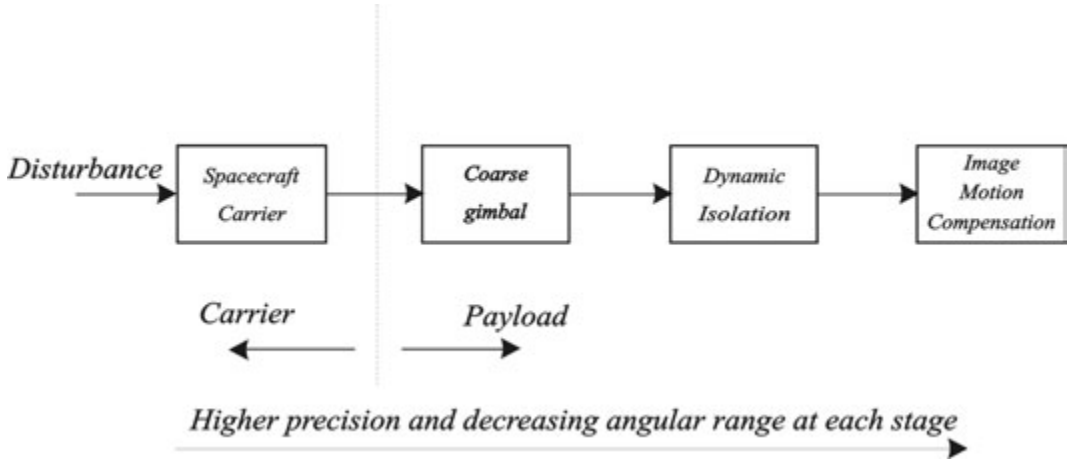

Figure 1.3: *Multi level actuation architecture*

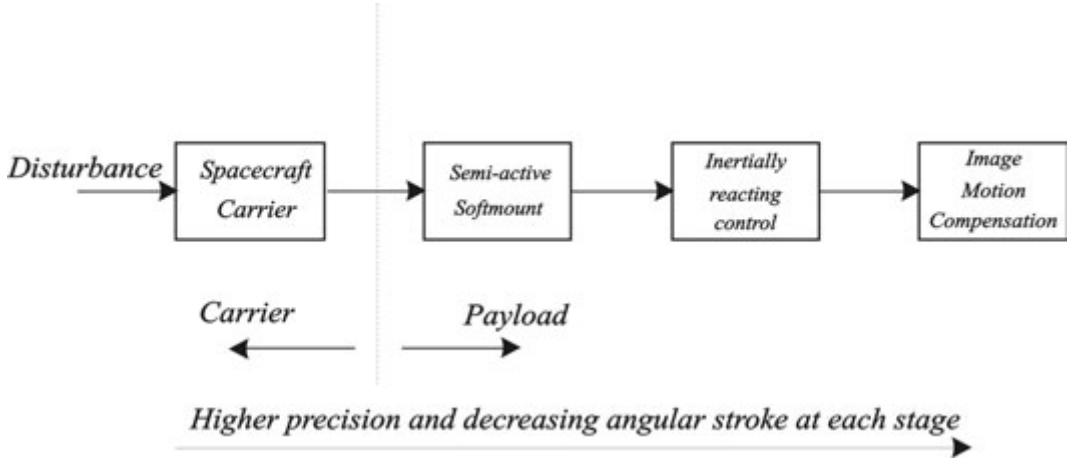

Figure 1.4: *Soft mount architecture*

The inertially reacting control is necessary because the semi-active soft mount cannot pass the control torque necessary to point the payload (Fig.1.5). The Control Moment Gyro (CMG) or Reaction Wheel control of the payload allows fast slews of the payload with minimum carrier/payload interaction, but introduces a potential disturbance source on the payload.

The preceeding discussion shows the need to have a generic multi-purpose 6 d.o.f. isolator with standardized architecture, which could be used to isolate noisy components such as a Reaction Wheel Assembly (RWA) as well as quiet ones (payloads). The isolator would also have a pointing functionality to augment the pointing accuracy beyond that of the reaction wheel assembly. The objective of this generic multi-purpose 6 d.o.f. isolator is to integrate all the functionality of the three stages in Figures 1.3 and 1.4. This is practically achieved through a **Stewart platform** [12, 13] with soft springs and active augmentation. Figure 1.6 shows the six-axis active vibration isolator done by the JPL for the purpose of active isolation in space applications, which was seminal in our project.

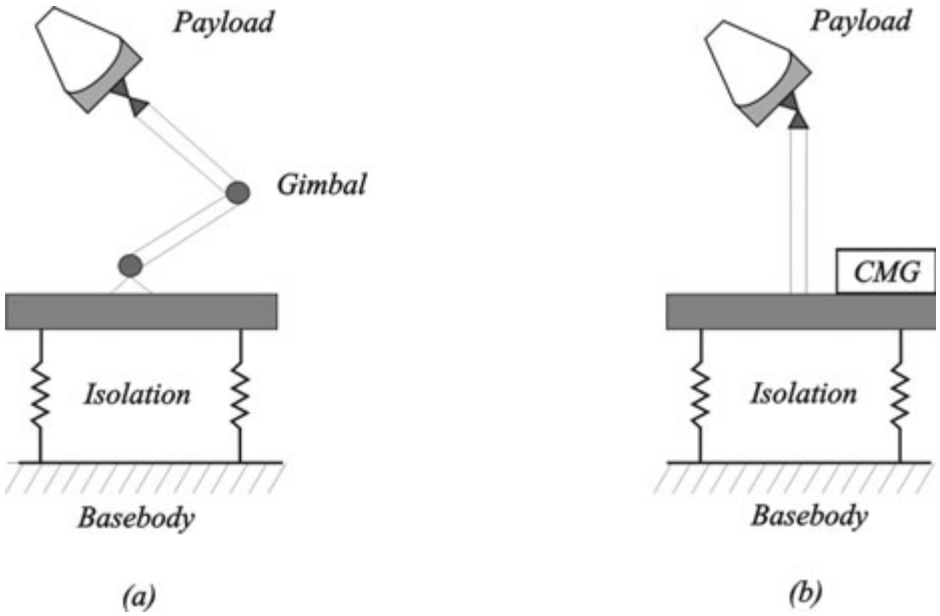

Figure 1.5: *(a) The slewing torque is provided by the base body and is transmitted through the isolation; (b) the slewing torque is provided by the Control Moment Gyro (CMG) and not by the base body*

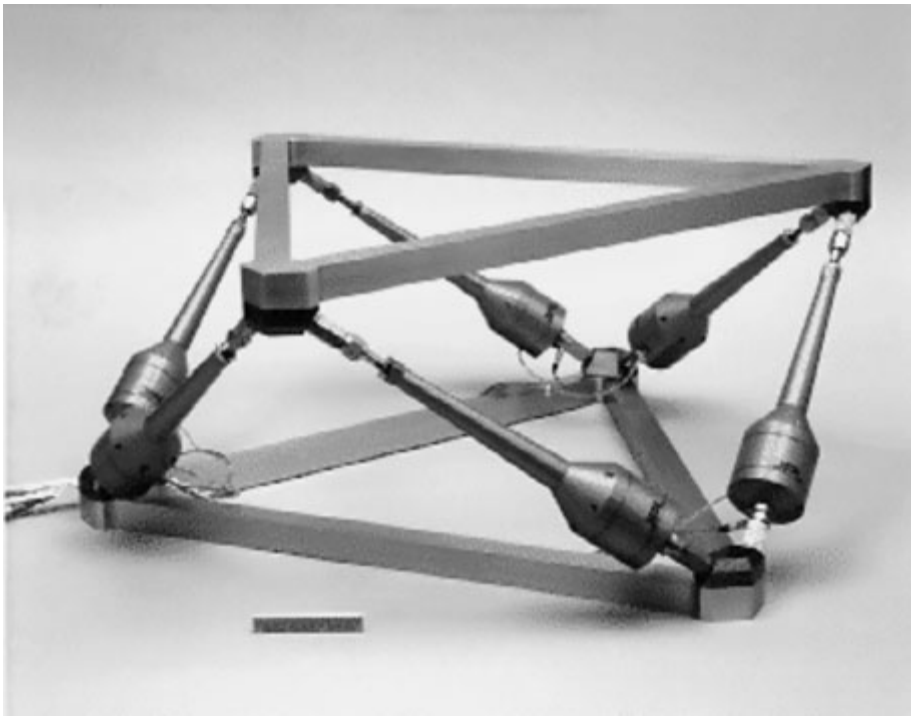

Figure 1.6: *JPL Multi-purpose generic active isolator based on Stewart platform with voice coil actuators*

A general pointing/isolation control strategy is illustrated in Fig.1.7 where the same actuators are used for isolation and pointing.

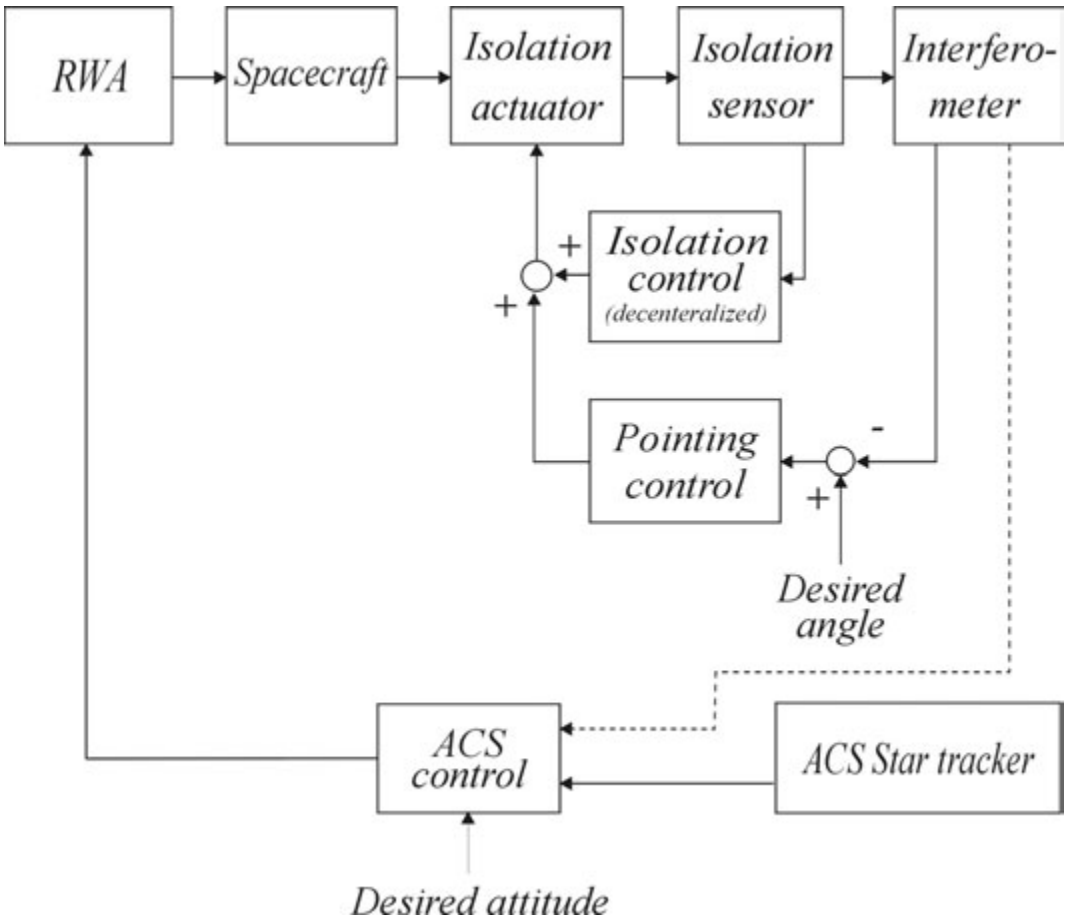

Figure 1.7: *Pointing/isolation control strategy for the generic multi-purpose 6 d.o.f. isolator*

1.4 Active damping of structures

Future space structures are likely to be assembled of mechanical trusses. These truss structures need to be made of strong, lightweight materials. However, to achieve the requirements of high accuracy and performance for the sensitive payloads installed on these structures, vibrations generated in the structures have to be damped using passive or active control techniques. Active damping of space trusses can be achieved in various ways; some of them have been studied extensively at the ASL over the past 15 years:

1. Integrating active struts in the structure by replacing some of its passive members with active ones (Fig.1.8) [14]. The active strut consists of a force sensor and displacement (piezoelectric) actuator; various configurations are shown in Fig.1.9.

2. By reinforcing the truss by a network of cables controlled by tendons (Fig.1.10) [15, 16]. Both techniques have been tested very successfully in laboratory experiments and simple techniques for predicting the closed-loop performance have been developed [4].

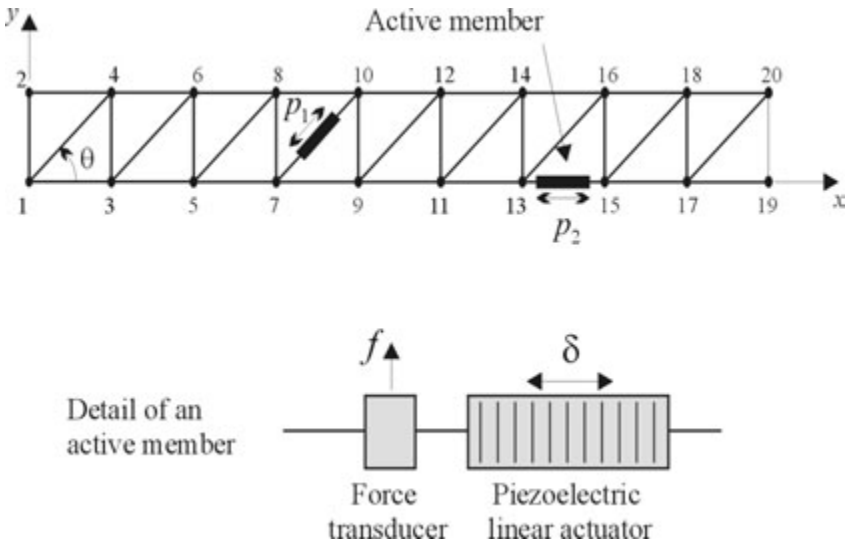

Figure 1.8: *A schematic view showing an integrated active strut in a truss structure*

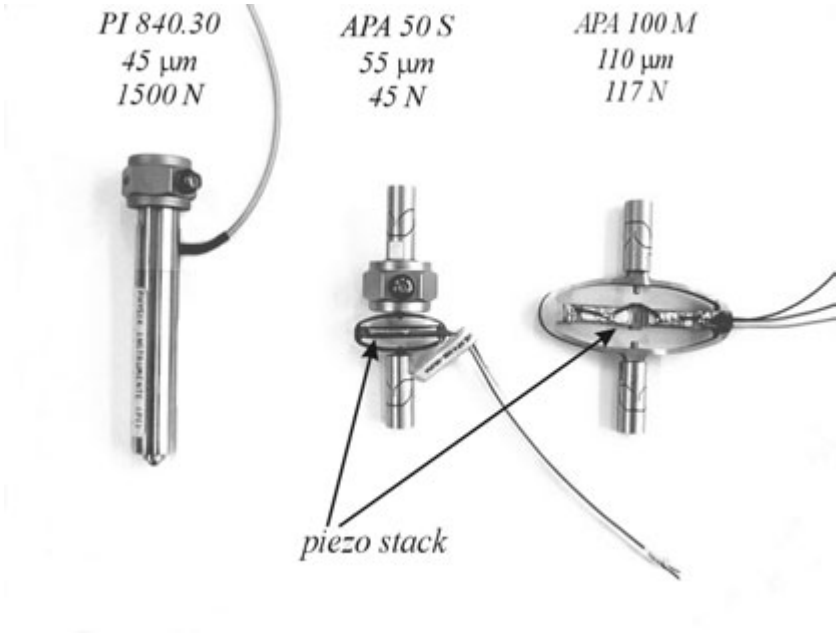

Figure 1.9: *Various designs of piezoelectric actuators (a) classical linear actuator (from PI) collocated with a force sensor, (b) amplified design (from CEDRAT) collocated with a force sensor, (c) amplified design equipped with flexible tips*

An alternative way is explored in this thesis in the form of a generic active damping interface which can be used to connect substructures together (Fig.1.11). The interface consists of Stewart platform; every leg is an active strut formed of a force sensor and a piezoelectric actuator controlled in a decentralized manner. The closed-loop poles can be predicted by the same technique as in the previous configurations. Figure 1.12 shows the ULB generic active damping interface designed and manufactured for this purpose.

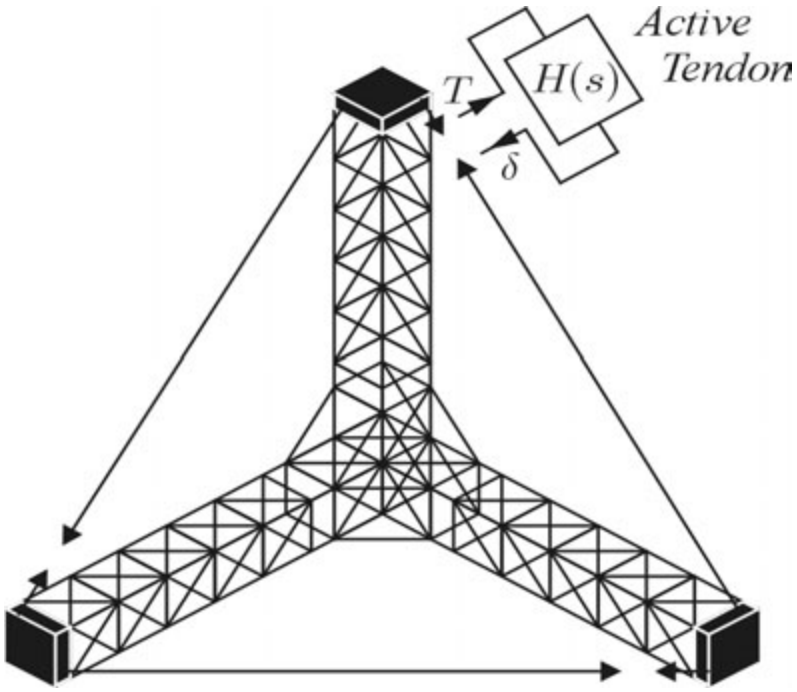

Figure 1.10: *A schematic view showing a cable structure with active tendons*

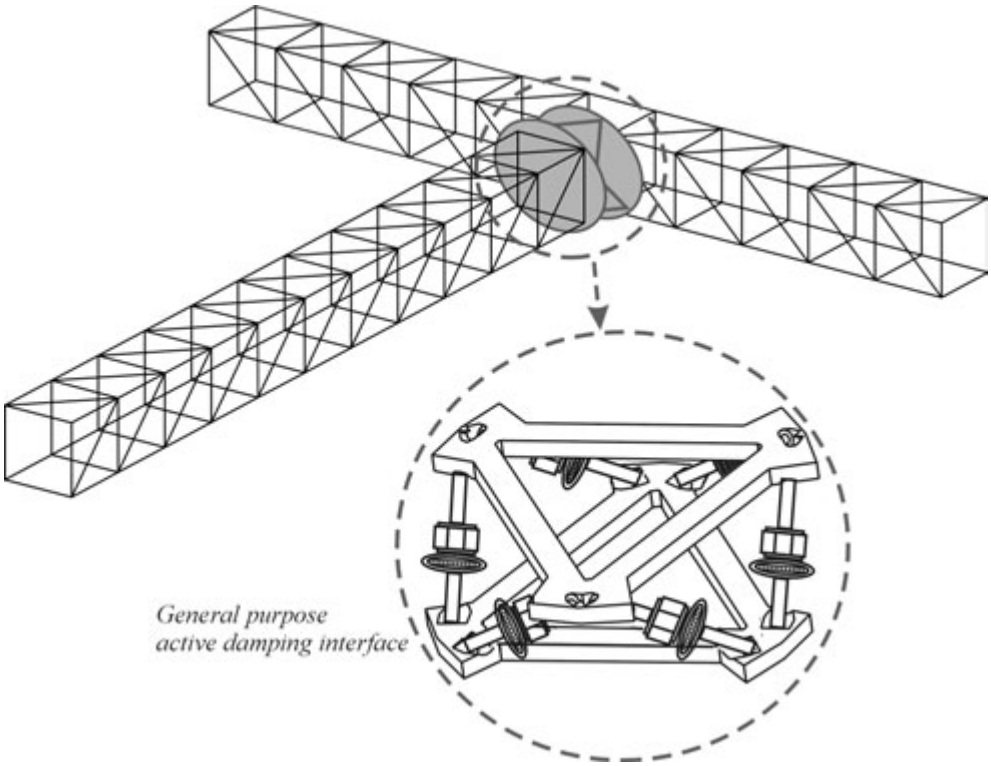

Figure 1.11: *An active damping interface between two truss structures*

Figure 1.12: *The ULB generic active damping interface*

1.5 Organization of the thesis

This thesis consists mainly of six main chapters. After this introduction, chapter 2 will include analysis of single-axis systems using soft actuators. The chapter begins with a discussion of passive isolation and then advances to talk about active vibration isolation discussing different control techniques. Experimental examples of single-axis systems will be discussed showing the modelling and the experimental results. Six-axis active isolation of vibrations is discussed, in general, in chapter 3. The chapter will show the general configuration of Stewart platform besides the general kinematic and dynamic analysis of the hexapods and it will concentrate on the soft Stewart platform. In this chapter, the design, technology, modelling and experimental testing of the ULB soft hexapod will be discussed in details; this hexapod has been designed, built and tested during this research period. Chapter 4 will talk about systems using hard piezoelectric actuators. In this chapter, the use of active struts in damping of vibrations will be disucussed. Another application for the active struts is stiffness reduction; a control technique will be presented to reduce the corner frequency of the system using proportional plus integral control strategy. This chapter will also handle another piezoelectric Stewart platform which is also designed, built and tested during the same period of this research to be used for the purpose of active damping and precision pointing. Technological aspects, modelling and experimental testing will be shown for this hexapod too. Conclusions and future work will be discussed in the last chapter.

1.6 References

[1] C. Crede. *Vibration and shock isolation.* John Wiley and Sons Inc., New York, 1951.

[2] J. Spanos, Z. Rahman, and G. Blackwood. A soft 6-axis active vibration isolator. In *Proceedings of the American Control Conference*, Seattle, Washington, USA, June 1995.

[3] A. Preumont. Modular payload isolation mounts based on Stewart platforms. Draft report prepared in support of the GSTP proposal, 1999.

[4] A. Preumont. *Vibration Control of Active Structures*. Kluwer Academic Publishers, Netherlands, 2nd edition, 2002.

[5] R.M. Chalasani. Ride performance potential of active suspension systems - PART 1: Simplified analysis based on a quarter-car model. In *Symposium on Simulation and Control of Ground Vehicles and Transportation Systems*, pages 187–204. ASME, December 1986.

[6] E.I. Rivin. Principles and criteria of vibration isolation of machinery. *Trans. of the ASME, Journal of Mechanical Engineering*, 101:682–692, October 1979.

[7] C.E. Kaplow and J.R. Velman. Active local vibration isolation applied to a flexible space telescope. *AIAA J. Guidance and Control*, 3(3):227–233, May-June 1980.

[8] R. Laskin and S. Sirlin. Future payload isolation and pointing system technology. *AIAA, J. Guidance and Control*, 9(4):469–477, July-August 1986.

[9] S.A. Collins and A.H. von Flotow. Active vibration isolation for spacecraft. In *42nd Congress of the International Astronautical Federation*, volume IAF-91-289, Montreal, Canada, October 1991.

[10] W. Anderson, N. Groom, and C. Woolley. Annular suspension and pointing system. *AIAA, J. Guidance and Control*, 2(5):367–373, September-October 1979.

[11] C. Keckler. ASPS preformance with large payloads onboard shuttle orbiter. *AIAA, J. Guidance*, 5(1):32–36, January-February 1979.

[12] V.E. Gough and S.G. Whitehall. Universal tyre testing machine. *Proc. Ninth International Technical Congress F.I.S.I.T.A.*, 117, May 1962.

[13] D. Stewart. A platform with six degrees of freedom. *Proc. Instn. Mech. Engrs.*, 180(15):371–386, 1965-66.

[14] A. Preumont, J.-P. Dufour, and C. Malekian. Active damping by a local force feedback with piezoelectric actuators. *AIAA, J. Guidance, Control and Dynamics*, 15(2):390–395, March-April 1992.

[15] A. Preumont, Y. Achkire, and F. Bossens. Active tendon control of large trusses. *AIAA Journal*, 38(3), March 2000.

[16] A. Preumont and Y. Achkire. Active damping of structures with guy cables. *AIAA Journal of Guidance, Control and Dynamics*, 20(2):320–326, March-April 1997.

Chapter 2

Single-axis vibration isolation

2.1 Introduction

Mechanical vibrations are present in varying levels in all locations where equipment work. The adverse effect of these disturbances can range from negligible to catastrophic depending on the severity of the disturbance and the sensitivity of the equipment [1]. Vibration control techniques in the form of vibration isolators have been developed to provide dynamic protection to all types of equipment [2]. In discussing vibration isolation, it is useful to identify the three basic elements:

- The sensitive equipment (payload needed to be isolated).
- The support structure (disturbance source).
- The isolation mount.

Many vibration isolation systems using mixed types of actuators and control techniques can be found in the literature (e.g. [3, 4]) but we will not go into details about them in this work. In this chapter, we are going to concentrate on three main single-axis systems of vibration isolation and only one of them will be developed and discussed in the context of this thesis,

- The first system is the single-axis soft isolator connecting two rigid bodies. This system will be developed into a six-axis isolator and will be discussed later in other chapters.
- The second system is the single-axis soft isolator based on using inertial (seismometer) feedback.
- The third system is the single-axis isolator using hard piezoelectric actuator and intermediate passive mount.

To simplify the problem of vibration isolation, we begin in this chapter with the discussion of a single-axis vibration isolation. In the next section we will show a detailed analysis for a single-axis isolator providing a technique for the selection of a passive isolator [1, 5]. Next, some active control techniques will be discussed showing a comparison between them

and the effect of the flexibility of the sensitive equipment on the stability of the system. The last sections talk about two alternative isolators based on using seismometers as feedback sensors for active vibration isolation with a practical example on using soft voice coil actuator and another example using a hard piezoelectric actuator and intermediate passive mount.

2.2 Single-axis passive isolator

Consider the single-axis isolator shown in Fig.2.1, where M is the mass of sensitive equipment, k and c are the stiffness and damping of the isolator respectively.

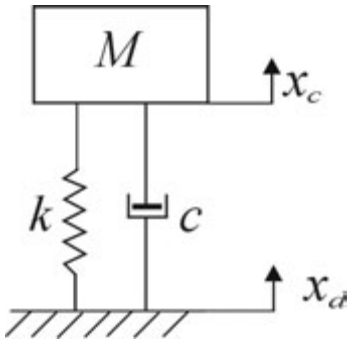

Figure 2.1: *Sensitive equipment mounted on a vibrating structure via passive isolator*

The isolation mount consists of a linear spring in parallel with a passive damper. The corner frequency of the system is $\omega_n = \sqrt{k/M}$ and the amount of damping in the isolator is defined by the damping ratio ξ; where $c/M = 2\xi\omega_n$. The transfer function in Laplace transform, between the disturbance displacement x_d and the payload displacement x_c is given by

$$\frac{x_c(s)}{x_d(s)} = \frac{1 + 2\xi s/\omega_n}{1 + 2\xi s/\omega_n + s^2/\omega_n^2} \tag{2.1}$$

Figure 2.2 shows a general plot for the transmissibility Frequency Response Function (FRF) of Equ.(2.1) where the abscissa is the ratio between the disturbing frequency ω and the natural frequency ω_n . Many lessons can be learned from this FRF:

1. When the disturbing frequency coincides with the the natural frequency of the system, an overshoot appears showing that the system vibrates at this frequency with high amplitudes.

2. The frequency where the curve crosses over the 0 dB line is reached when the disturbing frequency is equal to $\omega = \sqrt{2}\omega_n$ [2]. This critical frequency is the point where the influence of vibration isolation begins.

3. At very low frequency and much below the resonance, the displacement of the sensitive payload follows faithfully the displacement of the disturbance source as if the

isolator were infinitely rigid. However, at frequencies much higher than the resonance, the curve rolls-off and the displacement of the payload decreases gradually while the disturbance is constant.

4. When we increase the damping ratio ξ, the overshoot that appears at the natural frequency decreases but, unfortunately, the sharpness of the roll-off at high frequency decreases too.

5. To maintain the sharp roll-off at high frequency while decreasing the overshoot at the resonance, active control is needed. Discussion of the active control of vibrations will begin later in this chapter.

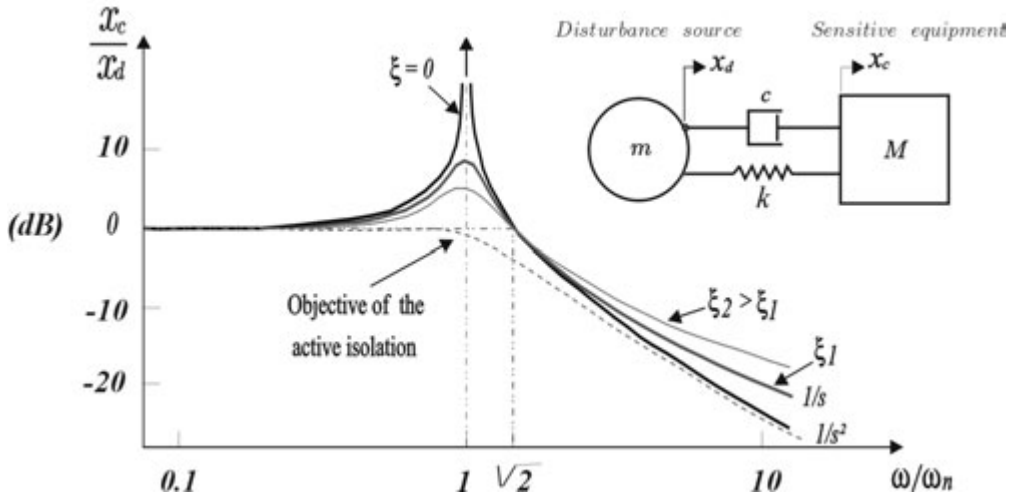

Figure 2.2: *Transmissibility FRF of a passive damper for various values of damping ratio* ξ

From Fig.2.2, one can see that when $\xi = 0$, the high frequency roll-off is $1/s^2$ (-40 dB/decade) while very large amplitude is seen near the natural frequency ω_n. On the other hand, when the damping ratio ξ is increased we reduce the overshoot at the resonance but we reduce also the roll-off to $1/s$ (-20 dB/decade) [5, 6]. As a result, the design of a passive damper involves a trade-off between the resonance amplification and the high frequency attenuation.

2.3 Passive isolator selection

Isolation is attained primarily by maintaining the proper relationship between the disturbing frequency and the system natural frequency. In order to design a passive isolator for a vibrating system, the following technique can be followed:

1. Determine the minimum disturbing frequency ω_d. For rotating equipment, the disturbing frequency is equal to the angular speed of rotation. If there are several disturbing frequencies one should take into account the one with the minimum frequency which is the most important.

2. Determine the maximum isolator natural frequency, ω_n, that can provide isolation. This natural frequency can be calculated by using the following equation

$$\omega_n = \frac{\omega_d}{\sqrt{2}} = 0.707\omega_d \tag{2.2}$$

If the natural frequency of the isolator exceeds ω_n calculated in this equation the isolation will not perform properly, even it is quite possible that it will amplify the vibrations. This step narrows the range of isolators to be selected from, but it tells nothing about the level of isolation.

3. Determine, specifically, what natural frequency of the isolator gives the required level of isolation. The desired level of isolation determines the transmissibility of the system; if the level of isolation is 80% then the transmissibility T is 0.2. The transmissibility FRF can be calculated from the following formula:

$$T = \sqrt{\frac{1 + (2\xi\frac{\omega_d}{\omega_n})^2}{(1 - \frac{\omega_d^2}{\omega_n^2})^2 + (2\xi\frac{\omega_d}{\omega_n})^2}} \tag{2.3}$$

Neglecting the damping ($\xi = 0$), T reads:

$$T = \left| \frac{1}{1 - (\frac{\omega_d}{\omega_n})^2} \right| \tag{2.4}$$

For $\xi > 0$ and at the resonance, $\omega_d/\omega_n = 1$, the transmissibility T has its maximum value and is related to the damping ratio ξ by

$$T_{max} = \frac{1}{2\xi} \tag{2.5}$$

Reciprocating Equ.(2.4), one can calculate the natural frequency as given by

$$\omega_n = \frac{\omega_d}{\sqrt{1 + \frac{1}{T}}} \tag{2.6}$$

Equ.(2.6) gives the natural frequency ω_n as a function of the disturbance frequency ω_d and the required attenuation T for an undamped isolator; it is valid only when $\omega_d/\omega_n > 1$.

4. Eventually, knowing the required natural frequency of the isolator, one can select the material and dimensions of the passive isolator that fits for the system according to the application and the surrounding conditions of the system. There are many commercial catalogues to select from (e.g. [7, 8, 9, 10]).

2.4 Active vibration isolation

We have seen in the previous section that applying passive damping in the isolator leads to reduce the overshoot at the resonance but it reduces the high-frequency attenuation rate. This leads to the objective in designing an active isolation system, that is to achieve a transmissibility which provides a -40 dB/decade attenuation at high frequency and at the same time has no amplification in the vicinity of the corner frequency as presented in dotted line in Fig.2.2. Active isolation is considered in space and terrestrial applications like those in [11, 12].

2.4.1 The sky-hook damper

Consider the single-axis soft isolator connecting two rigid bodies as shown in Fig.2.3(a); It consists of a soft spring k acting in parallel with a force actuator F_a, to isolate the sensitive payload M from the disturbance source m. There is an accelerometer to measure the acceleration of the payload and the signal is integrated and fed back to the force actuator. The equations governing the system are as follows:

disturbance source:

$$x_d(s) = \frac{1}{ms^2}(-F_a - F_k) + \frac{1}{ms^2}F_d \tag{2.7}$$

Sensitive payload

$$x_c(s) = \frac{1}{Ms^2}(F_a + F_k) \tag{2.8}$$

Spring

$$F_k = -(x_c - x_d)k \tag{2.9}$$

In the sky-hook damper technique, the feedback is based on the absolute acceleration of the sensitive payload, s^2x_c, with integral controller g/s leading to the feedback equation:

$$F_a = -\frac{g}{s}s^2x_c = -gsx_c \tag{2.10}$$

It can be clearly seen that the active control force is proportional to the absolute velocity of the payload; this is why this technique is called "*skyhook damper*", an equivalent representation is shown in Fig.2.3(b); imagining that the payload is suspended by a damper to a point in the sky [13, 14]. Combining the above equations, we obtain the transmissibility of the active isolation:

$$[Ms^2 + gs + k]x_c = kx_d \tag{2.11}$$

or

$$\frac{x_c}{x_d} = [\frac{M}{k}s^2 + \frac{g}{k}s + 1]^{-1} \tag{2.12}$$

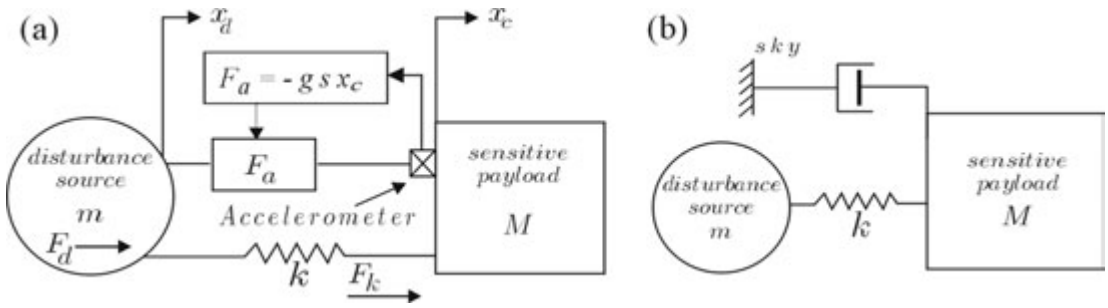

Figure 2.3: *(a):Single-axis soft isolator with acceleration feedback, (b): Equivalent sky-hook damper*

From the foregoing equations, the corner frequency of the system is $\omega_n = \sqrt{k/M}$, the high frequency decay rate is $1/s^2$, that is -40 dB/decade, can be chosen in such a way that the isolator is critically damped ($\xi = 1$), this is achieved for a control gain $g = 2\sqrt{kM}$. This way, we achieve a low-pass filter without overshoot at the corner frequency and with a roll-off of -40 dB/decade as represented in dotted line in Fig.2.2. The open-loop transfer function, between the actuation force F_a and the acceleration of the payload s^2x_c, can easily be derived from the above equations and it reads:

$$G(s) = \frac{s^2 x_c(s)}{F_a(s)} = \frac{ms^2}{Mms^2 + k(M+m)} \tag{2.13}$$

The open-loop poles are the natural frequencies of the system without control. The rigid body modes do not appear in the transfer function (Equ.(2.13)) because they are not controllable from F_a. The root locus of the closed-loop poles when the gain is increased is shown in Fig.2.4.

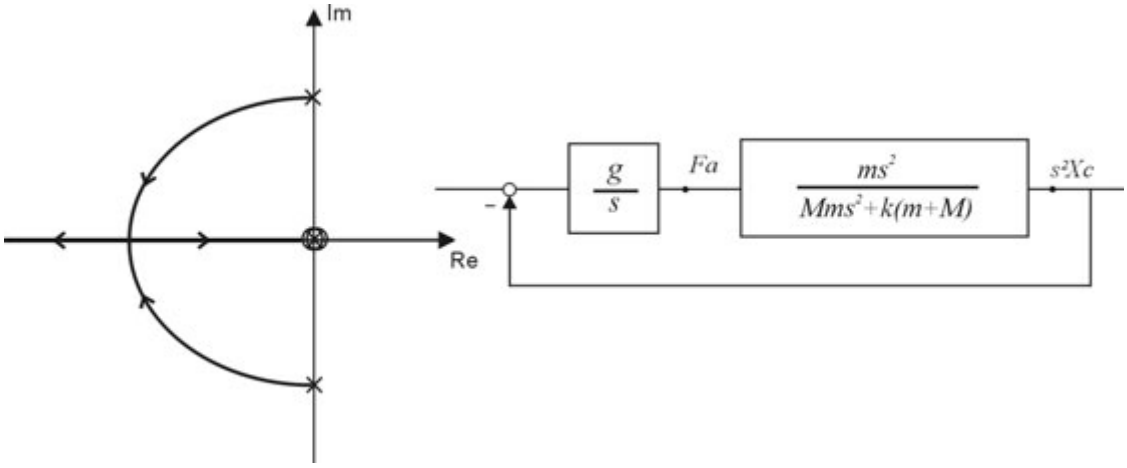

Figure 2.4: *Root locus of the sky-hook damper*

So far in the active isolator, we considered that the isolator contains only a spring. If we add to the isolator a passive damper (dash-pot) with a damping coefficient c, the isolator equation becomes:

$$F_k = -(x_c - x_d)(k + cs) \tag{2.14}$$

and the equation of motion becomes

$$[Ms^2 + (g + c)s + k]x_c = (k + cs)x_d \tag{2.15}$$

The transmissibility, then, reads

$$\frac{x_c}{x_d} = \frac{k + cs}{Ms^2 + (g + c)s + k} \tag{2.16}$$

This equation shows that the damping adds a zero at $(s = k/c)$ that corresponds to +20 dB/decade and, thus, decreases the high frequency attenuation rate to -20 dB/decade. This means that the passive damping in the active isolator decreases the performance of vibration isolation at high frequency.

2.4.2 Integral Force feedback

Looking at Equ.(2.8), one can see that the acceleration of the sensitive equipment is proportional to the total force transmitted by the interface, $F = F_a + F_k$.

$$s^2 x_c = \frac{1}{M}(F_a + F_k) = \frac{F}{M} \tag{2.17}$$

Accordingly, the sky-hook damper can be obtained alternatively with the control configuration of Fig.2.5, where a force sensor has been substituted to the acceleration sensor on the payload side of the interface. The governing equations (2.7) to (2.9) still hold and we must add the sensor equation

$$F = F_a + F_k \tag{2.18}$$

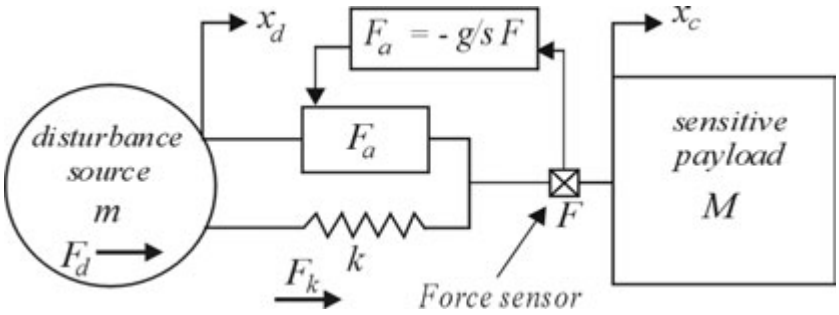

Figure 2.5: *Force feedback isolator*

It follows that the open-loop transfer function between the actuator force F_a and the sensor force F is:

$$G(s) = \frac{F}{F_a} = \frac{mMs^2}{mMs^2 + (m + M)k} \tag{2.19}$$

The open-loop poles are the natural frequencies of the system without control. Equ.(2.19) is identical to Equ.(2.13), except for the constant M relating the total force F to the acceleration of the payload. As a result, the root locus of Fig.2.4 also applies to the integral force feedback (IFF) controller which is totally equivalent to the acceleration feedback. Taking into account the constant M relating the payload acceleration and the total transmitted force, the transmissibility of the active isolator now reads

$$\frac{x_c}{x_d} = [\frac{M}{k}s^2 + \frac{M}{k}gs + 1]^{-1} \tag{2.20}$$

Assuming $H(s)$ as an arbitrary feedback controller, the transmissibility can be given in a more general form by:

$$\frac{x_c}{x_d} = [1 + \frac{M}{k}s^2(1 + H(s))]^{-1} \tag{2.21}$$

This result is interesting and could possibly be used in the design and selction of the appropriate feedback controller for a given transmissibility. Although the control strategies based on acceleration and force sensors are equivalent for the isolation of rigid bodies, the force feedback has two advantages:

- *Sensitivity:* Force sensors with a sensitivity of $10^{-3}N$ are commonplace and commercially available; if we consider a sensitive payload equipment with a mass of $1000kg$ (e.g. telescope), the corresponding acceleration is $10^{-6}m/s^2$. Accelerometers with such a sensitivity are more difficult to find; for example, the most sensitive accelerometer available in the Bruel & Kjaer catalogue is $2\times10^{-5}m/s^2$, (model 8318)
- *Stability:* When the payload is flexible, the behaviour of the acceleration and force feedback are no longer the same; this is discussed below in the next section.

2.4.3 Sensitive payload with flexible appendage

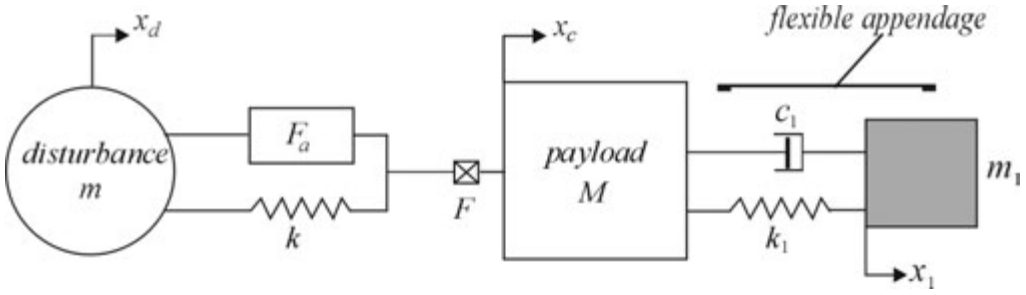

Figure 2.6: *Sensitive payload with flexible appendage*

When the sensitive equipment is a flexible body, the behaviour of the acceleration feedback and the force feedback are no longer the same, due to different poles/zeros configurations of the two control strategies [15]. In fact, different sensor configurations correspond to different locations of the zeros in the s-plane. To analyse this situation, consider the system shown in Fig.2.6. The nominal numerical values used in the calculations of this

example are $m = 1.1kg$, $M = 1.7kg$, $k = k_1 = 12000N/m$, $c_1 = 0$; the mass m_1 of the flexible appendage is taken as a parameter to analyse the interaction between the flexible appendage and the isolation system. When m_1 is small, the flexible appendage is much more rigid than the isolation system and the situation is not much different from that of a rigid body. Figure 2.7 shows the root locus plots for $m_1 = 0.5kg$; the acceleration feedback and the force feedback have similar root locus plots, with a new pole/zero pair appearing higher on the imaginary axis; the only difference between the two plots is the distance between the pole and the zero which is larger for the acceleration feedback; as a result, the acceleration feedback produces a larger damping of the higher mode. On the contrary, when m_1 is large, the root locus plots are reorganized as shown in Fig.2.8 for $m_1 = 3.5kg$. In the case of force feedback (Fig.2.8.a), the poles and zeros still alternate on the imaginery axis, leading to a stable root locus; this property is lost for the acceleration feedback (Fig.2.8.b), leading to an unstable loop for the lower mode. In practice, however, this loop is moved slightly to the left by the structural damping and the control system can still operate for small gains (conditionally stable).

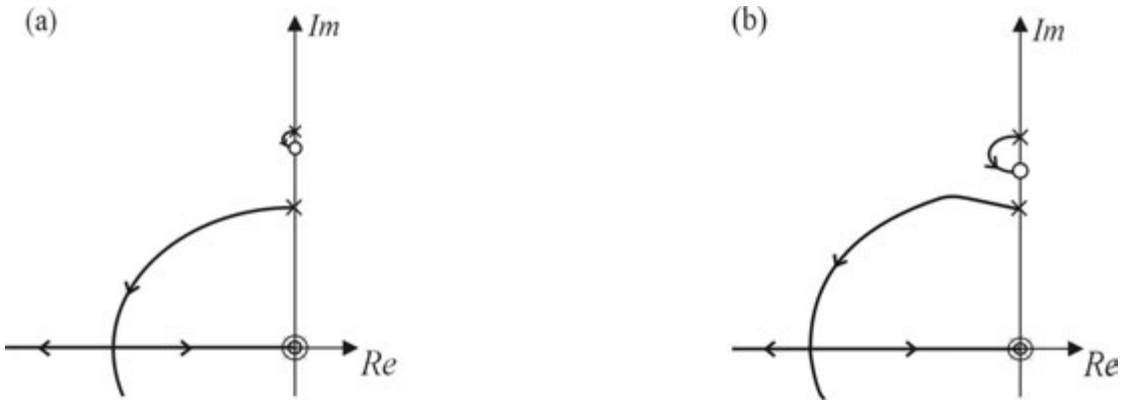

Figure 2.7: *Root locus of the isolation system with a light flexible appendage ($m_1 = 0.5kg$). (a)Force feedback, (b)Acceleration feedback*

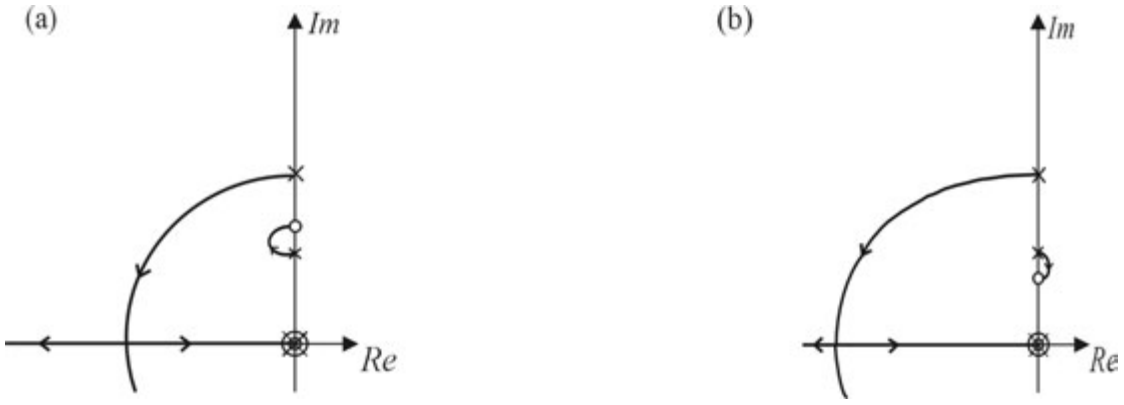

Figure 2.8: *Root locus of the isolation system with a heavy flexible appendage ($m_1 = 3.5kg$). (a)Force feedback, (b)Acceleration feedback*

2.4.4 Open-loop pole/zero pattern of a soft isolator with force feedback

The following result confirms the observation of the previous example:
If two arbitrary flexible, undamped structures are connected with a single axis soft isolator with force feedback (Fig.2.9), the poles and zeros in the open-loop transfer function $F(s)/F_a(s)$ alternate on the imaginary axis [15].

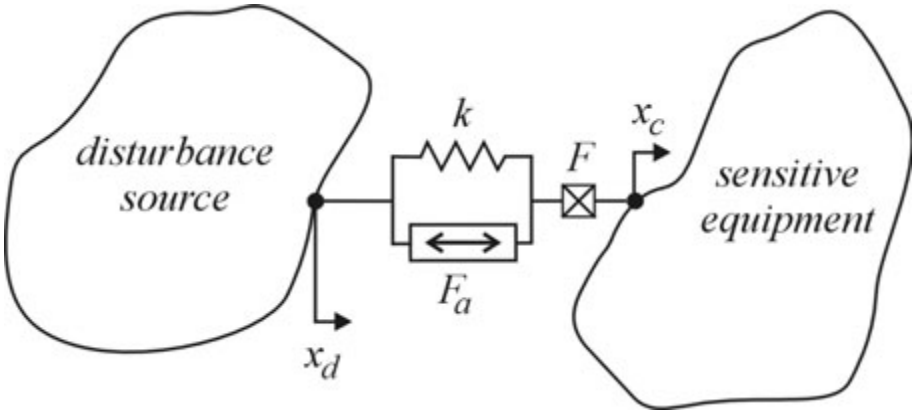

Figure 2.9: *Two arbitrary flexible structures connected with a single axis soft isolator with force feedback*

The proof stems from the property of the collocated systems with *energetically conjugated* input and output variables (e.g. force input and displacement output, or torque input and angle output): For such a system, all the residues in the modal expansion of the transfer function have the same sign and this results in alternating poles and zeros on the imaginary axis [16, 17]. If we now examine the transfer function between the control force F_a and the output of the force sensor F (Fig.2.9), although the actuator and sensor are collocated, F and F_a are not energetically conjugated and the preceding property does not apply. However, the total force F transmitted by the isolator is the sum of the control force F_a and the spring force, $k\Delta x$, where Δx is the relative displacement of the two structures along the isolator axis,

$$F = k\Delta x - F_a$$

or

$$\frac{F(s)}{F_a(s)} = k\frac{\Delta x(s)}{F_a(s)} - 1 \tag{2.22}$$

Thus, the open-loop transfer function F/F_a is the sum of $k\Delta x/F_a$ and a negative unit feedthrough. The input F_a and the output Δx involved in the transfer function $\Delta x/F_a$ are energetically conjugated and, as a result, the transfer function $\Delta x/F_a$ has all its residues positive and possesses alternating poles and zeros along the imaginary axis. The addition of a feedthrough term does not affect the residues in the modal expansion; the frequency response function (FRF) $F(\omega)/F_a(\omega)$ (obtained from the transfer function by setting $s = j\omega$, and which is purely real if the system is undamped) is obtained from the FRF $\Delta x(\omega)/F_a(\omega)$ by moving it along the ordinate axis by the amount of feedthrough;

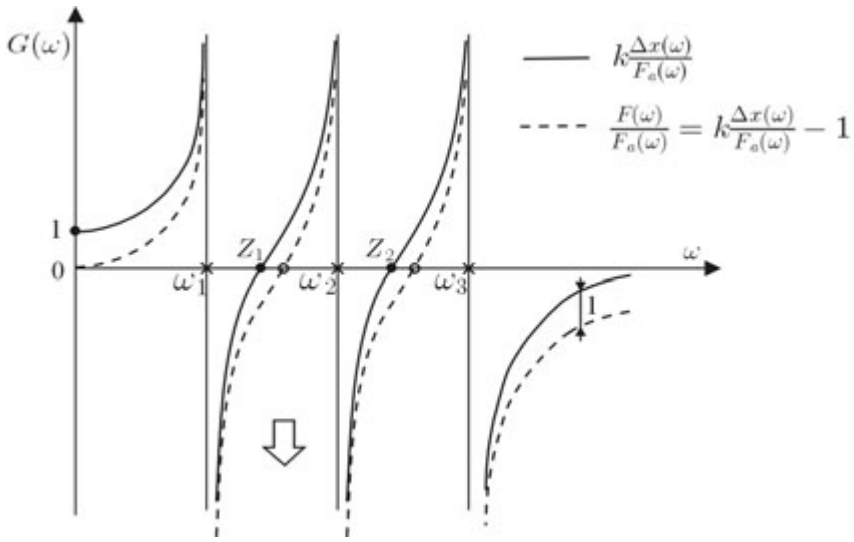

Figure 2.10: *FRFs* $k\frac{\Delta x(\omega)}{F_a(\omega)}$ *and* $\frac{F(\omega)}{F_a(\omega)}$ *for an undamped structure (they are purely real).* ω_i *are the resonance frequencies and* Z_i *are the transmission zeros. The unit feedthrough component which appears in* F/F_a *alters the location of the zeros (from* $\bullet$ *to* $\circ$*) without changing the interlacing property.*

this changes the location of the zeros, without, however, changing the interlacing property (Fig.2.10).

2.5 Experiment with a single-axis isolator using force feedback

2.5.1 Experimental set-up

The concept of single-axis isolation has been verified experimentally with the setup shown in Fig.2.11 [18, 19]. At the right hand side of this figure, we see a shaker used to produce the disturbance signals to excite the system. The mass at the left hand side represents the sensitive payload to be isolated; the payload has a mass of 0.5 kg. The mass in the middle is exposed directly to the disturbance source and has a mass of 1.1 kg. The voice coil soft actuator used for active isolation is imbedded inside the middle mass for better alignment and to avoid the excitation of the lateral and torsional modes. A force sensor is collocated axially between the actuator and the payload mass. Flexible tips, with high axial stiffness and low bending stiffness, are used to connect the masses to the isolator to reduce the effect of the lateral modes. The whole system has been hanged to the ceiling by elastic springs to compensate for the gravity forces. It is worth saying here that the soft passive mount introduces a soft connection that may not support the launch loads in space applications without being locked, but it is necessary to attenuate a broad band of disturbances [20, 21]. Figure 2.12(a) is a symbolic representation of the system in Fig.2.11; the corresponding block diagram is shown in Fig.2.12(b) [12]. This model assumes that both, the disturbance source and the sensitive payload, are rigid bodies. This assumption neglects the effect of the flexible modes that may appear in the system affecting the control authority and the stability of the system in some cases. G_m here

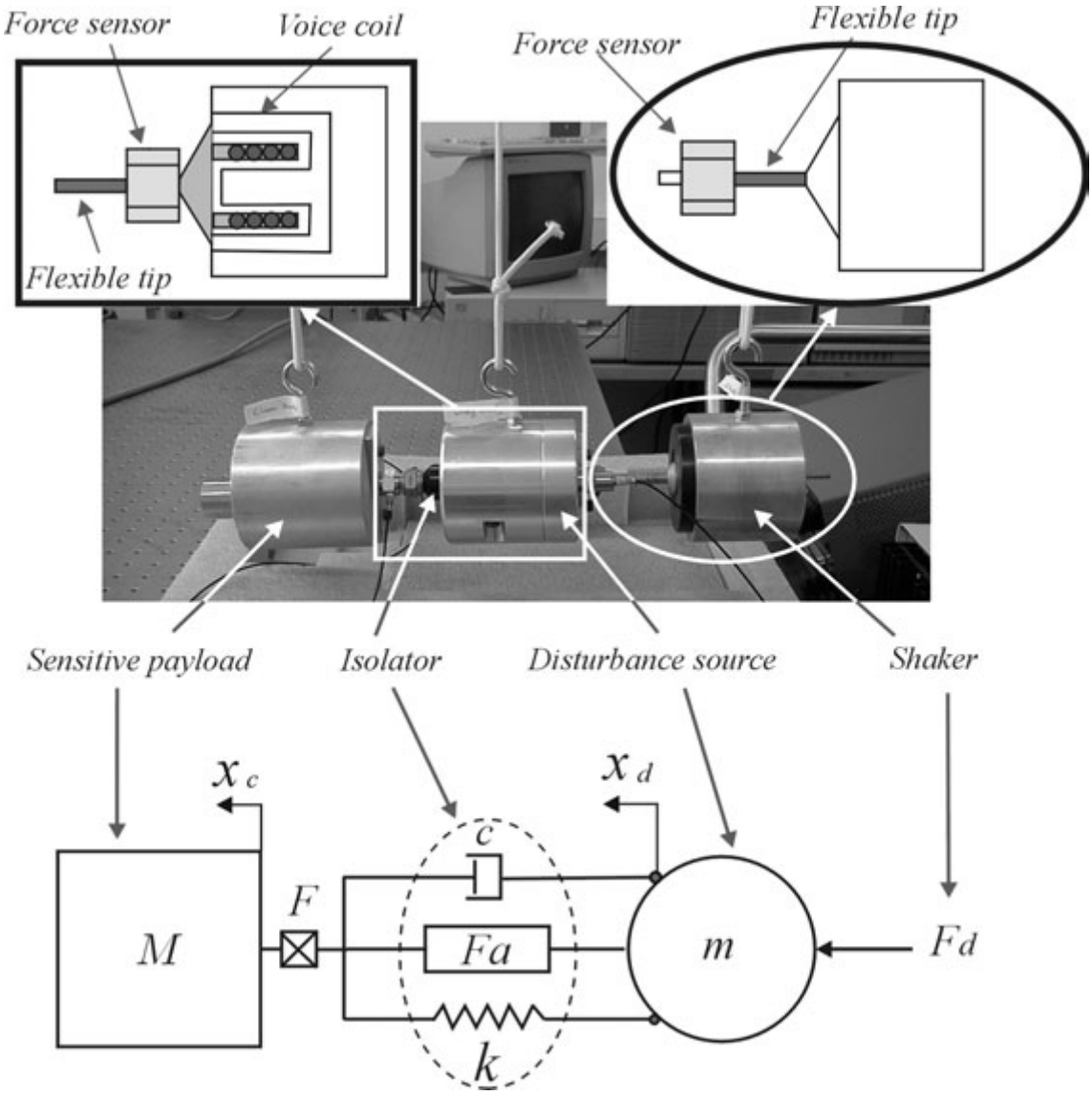

Figure 2.11: *Experimental setup of a single-degree-of-freedom isolator with a soft actuator*

denotes the transfer function between the disturbing force F_d and the displacement x_d. G_M denotes the transfer function between the force acting on the sensitive equipment F and its displacement x_c. The block denoted by $k + cs$ represents the passive spring and damper in the isolator. F_a denotes an active actuation force that can be added in parallel with the passive isolator. From this block model, one can see that both displacements of the disturbance and payload influence each other, this influence depends on the force in the isolator. In other words, if the disturbing frequency is much lower than the corner frequency of the isolator the payload will follow the disturbance source motion. On the other hand, the oscillations of the payload will be attenuated when the system is disturbed at a frequency much higher than its corner frequency. The predicted corner frequency of the system is 4.5 Hz as shown in the FRF (Fig.2.13). Figure 2.13 shows the transmissibility

function, between the displacement of the disturbance source and the displacement of the payload, without control (open-loop) and with applying the sky-hook damper (integral force feedback) with the proper gain (closed-loop). One can see that the signals before the corner frequency are passed while all the disturbances after the corner frequency are isolated with an attenuation rate of -40 dB/decade. Here, we assume a small passive damping in the isolator(less than 1%).

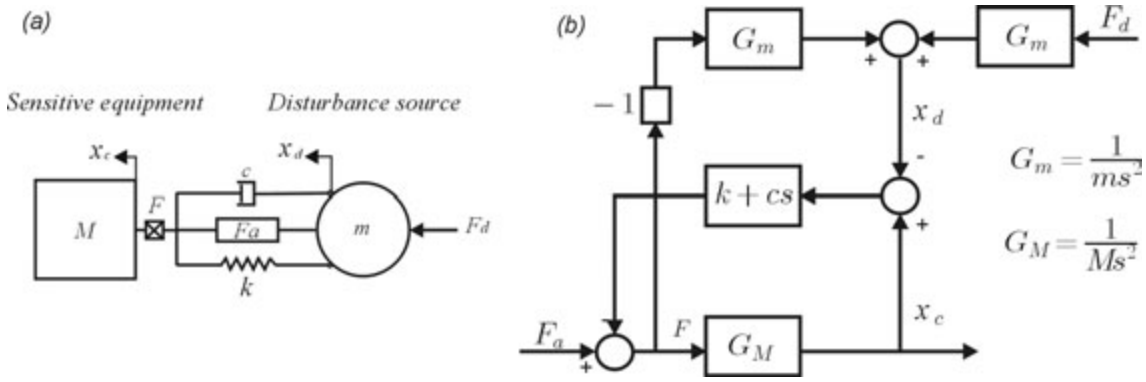

Figure 2.12: *(a)Single-axis isolator, (b)Dynamic model of the single-axis isolator*

2.5.2 Experimental results

The system has been excited with a random signal between 1 to 100 Hz. IFF controller, with the appropriate gain, is applied to the system. The force acting on the payload sensitive mass is measured by the feedback force sensor, integrated, amplified and fed back to the voice coil actuator (the integration is done analogically in the charge amplifier).

Figure 2.14 shows the transmissibility FRF between the displacement of the disturbance source and the displacement of the payload mass with and without applying the control. It is similar to the theoretical prediction in Fig.2.13 with one difference that the lateral modes at high frequency did not vanish completely from the curve because the decoupling and alignment of the system were not perfect. The experimental FRF shows, as well as the theoretical one, that the low frequency signals are passed with a unity magnitude up to the corner frequency where the vibration isolation begins and the curve attenuates at a rate of -40 dB/decade. The closed-loop curve follows the path of the open-loop one but without any overshoot at the resonance which is consistent with the theory of active vibration isolation discussed before. -40 dB/decade roll-off at high frequency has been obtained by minimizing the passive damping in the isolator. The passive damping is reduced by eliminating the eddy current from the actuator; this has been done by removing the metallic coil holder that produces this eddy current in the magnetic field. A detailed design of the voice coil actuator will be given in the next chapter.

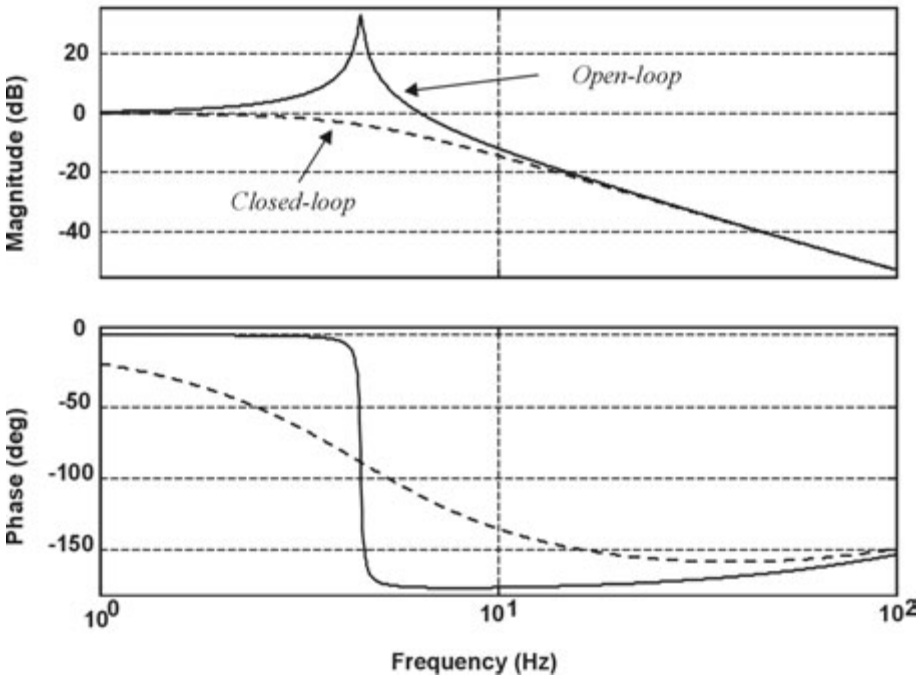

Figure 2.13: *Predicted transmissibility FRF (x_c/x_d), between the displacement x_d of the disturbance source and the displacement x_c of the payload, with and without control*

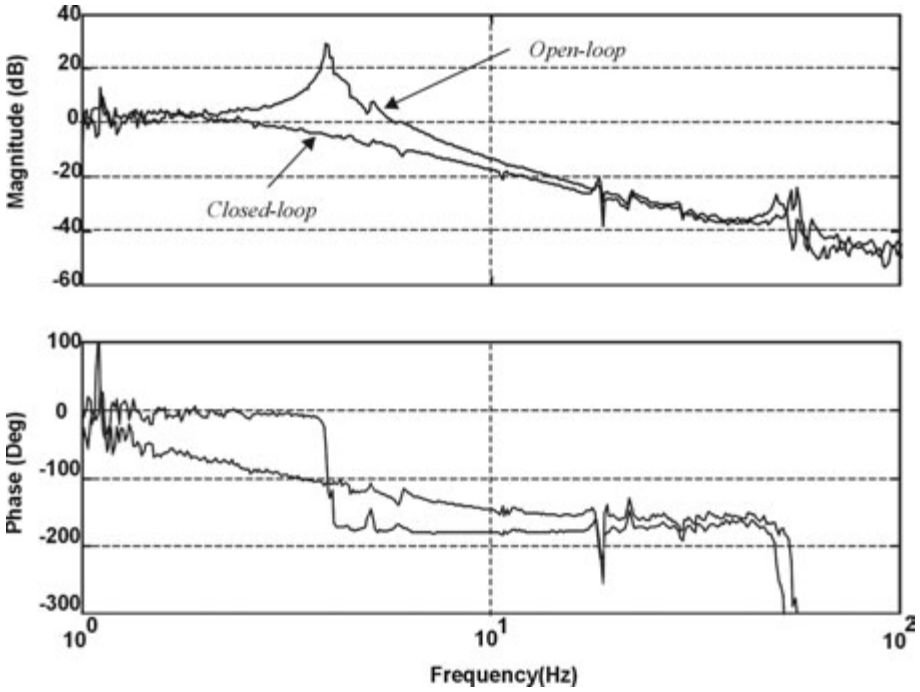

Figure 2.14: *Experimental transmissibility FRF (x_c/x_d), between the displacement x_d of the disturbance source and the displacement x_c of the payload, with and without control*

2.6 Single-axis vibration isolation using geophones

Geophones are the most commonly used velocity inertial sensors to measure seismic vibrations. It is an electromagnetic sensor that measures the velocity and produces a voltage signal thanks to the motion of a coil in a magnetic field (see appendix B). To discuss the effect of inertial feedback on vibration isolation, consider the single-axis isolation system shown in Fig.2.15 which consists of a disturbance mass m, a payload mass M, a force generating actuator (voice coil) and a velocity feedback sensor (geophone).

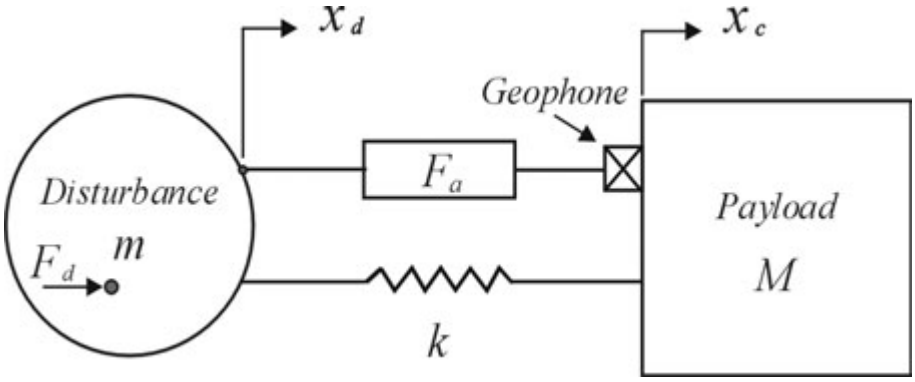

Figure 2.15: *Single-axis isolator using geophone sensor*

This figure is similar to Fig.2.3(a) with a geophone replacing the accelerometer. All the governing equations (2.7) to (2.9), therefore, still hold and the open-loop plant transfer function between the actuation force and the payload velocity reads

$$G(s) = \frac{sx_c(s)}{F_a(s)} = \frac{ms}{Mms^2 + k(M+m)} \tag{2.23}$$

This passive plant FRF has two conjugate poles near the imaginery axis and one zero at the origin. The dynamics of the geophone $D_g(s)$, between the payload velocity and the voltage output of the geophone, can be expressed as a second order high-pass filter

$$D_g(s) = \frac{Voltage}{Velocity} = \frac{s^2}{s^2 + 2\xi_g\omega_g s + \omega_g^2} \tag{2.24}$$

where ω_g is the resonance frequency and ξ_g is the damping factor of the geophone. This adds two more conjugate poles and two other zeros to the system as can be seen from Fig.2.16. When the velocity of the equipment is measured using the geophone, the geophone dynamics have an influence on the response and the poles of the geophone appear in the FRF as shown in Fig.2.17. A low-pass filter is added at higher frequency behind the corner frequency of the system to cut-off the high-frequency disturbances and increase the high-frequency attenuation rate. By increasing the control gain, the mode of the isolator moves deep to the left hand side while the pole of the geophone moves the other way towards the right half-plane leading the system to be conditionally stable. The damping in the geophone increases the stability margin of the system allowing a higher damping for

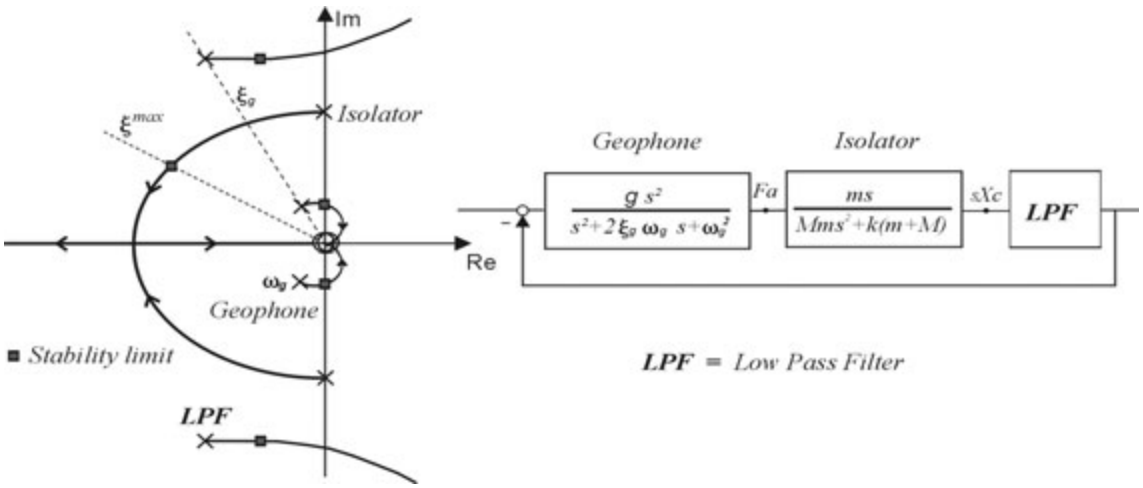

Figure 2.16: *root locus of the single-axis isolator using geophone feedback*

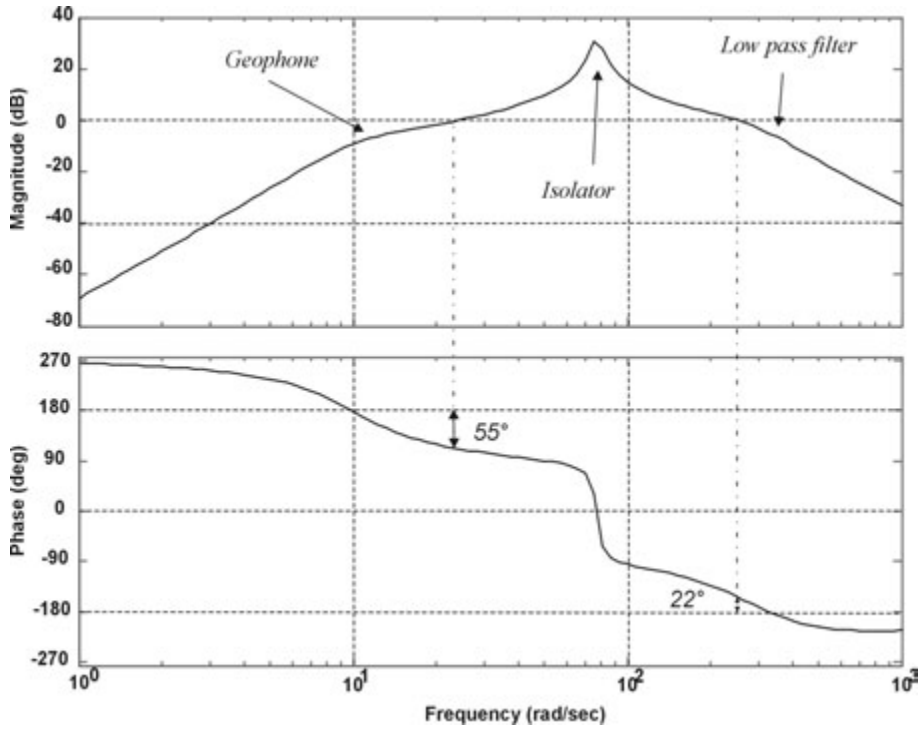

Figure 2.17: *FRF between the actuation force and the velocity of the payload in the single-axis isolator using geophone sensor*

the isolator pole before the arrival of the geophone pole to the right-half plane (stability limit).

Figure 2.18 shows a Nichols chart for the open-loop system (GH). The Nichols chart is convenient in a way that it shows a magnification for the vicinity of the stability limits where the 0 dB gain line meets the 180 degrees phase lines. Moving on the 0 dB line, the horizontal distance between the curve and the +180 degrees line represents the phase

margin at the lower unity gain point and the distance between the curve and the -180 degrees line represents the phase margin at the upper unity gain point. The constant gain curves around the unity gain points are the closed-loop magnitudes of the system where the maximum overshoot is fixed by the constant gain curve tangent to the open-loop FRF (GH).

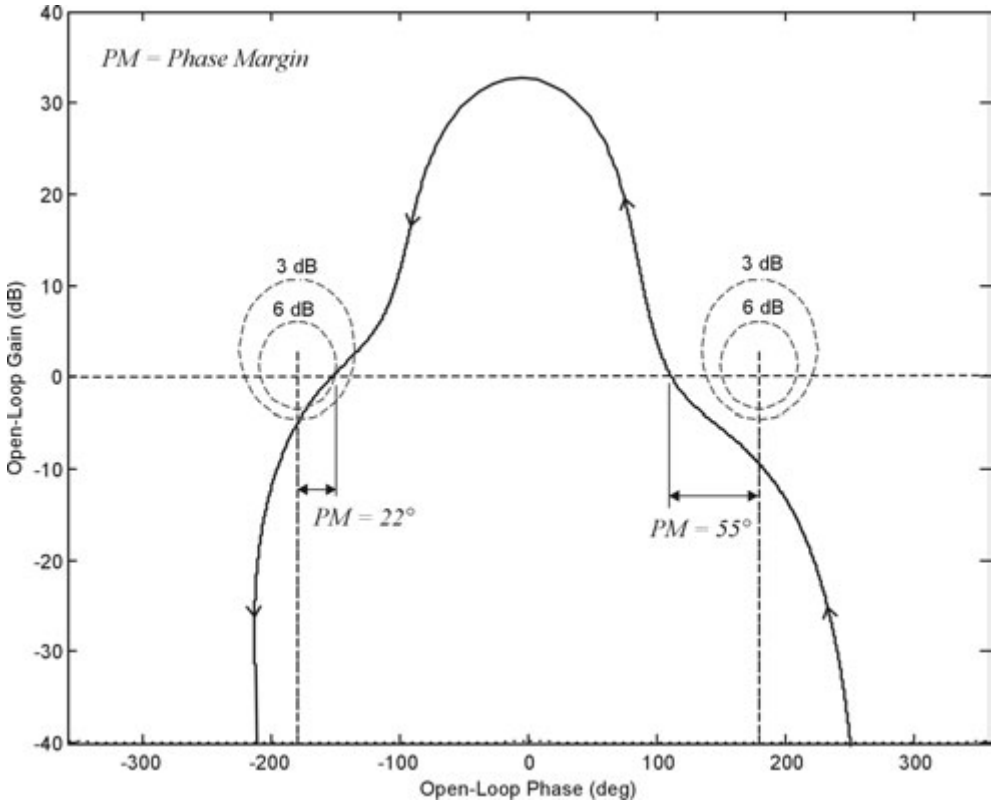

Figure 2.18: *Nichols chart between the open-loop gain and the open-loop phase of the system*

Looking at the open-loop FRF (Fig.2.17), one sees that the magnitude crosses the unity line (0 dB) twice. Amplification occurs in the closed-loop magnitude of the transmitted signal at the cross-over points if the phase at these points is close to 180 degrees. To explain the existence of the overshoots (amplifications) in the closed-loop response, consider the block diagram of the general feedback system shown in Fig.2.19. The plant passive mechanical FRF is denoted by G and the compensator is denoted by H. The characteristic equation of the system is $(1 + GH = 0)$. This characteristic equation represents the denominator of the closed-loop transfer function that represents the effect of the disturbance d on the output y and reads

$$\frac{y}{d} = \frac{1}{1 + GH} \tag{2.25}$$

The roots of the characteristic equation determine the stability of the system. When the loop gain $|GH| \ll 1$, the closed-loop gain (magnitude) equals to unity and follows the open-loop gain. When $|GH| \gg 1$, the closed-loop gain is reduced by increasing the gain of

the compensator. The range where $|GH| > 1$ is called the bandwidth of the servo system. In this range, the compensator has its highest effect on the response of the system. If the loop gain $|GH| \approx 1$ and the phase equals to 180 degrees, it changes its sign to be (≈ -1). This change in the sign makes the denominator very small and the closed-loop response very large which causes a rise (overshoot) in the gain appears as a new resonance at the unity gain points. These overshoots lead the system to be conditionally stable. On the contrary, using the acceleration feedback with integrator (sky-hook damper) leads to unconditional stability (if the sensitive payload is a rigid body and if the sensor dynamics are neglected). A comparison between geophone velocity feedback and sky-hook damper is shown in Figures 2.20 and 2.21. Figure 2.20 shows the transmissibility between the displacement of the disturbance source and the displacement of the sensitive equipment using sky-hook damper and Fig.2.21 shows the transmissibility between the displacement of the disturbance source and the displacement of the sensitive equipment using velocity (geophone) feedback. The main distinctive feature is that using a perfect geophone with proportional feedback would produce the same result as a perfect accelerometer with integral feedback (sky-hook). The piezo accelerometer, when connected to a charge amplifier (contains a high-pass filter), could have the same dynamics as the geophone.

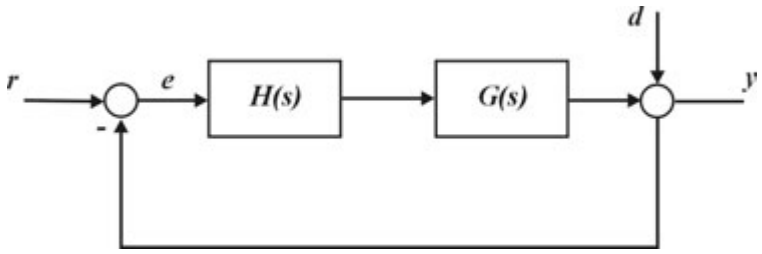

Figure 2.19: *Block diagram of feedback system*

To reduce the effect of the overshoots at the unity gain points on the stability of the system, the phase margin of the system should be increased; in other words, the phase difference should be increased between the closed-loop phase and the +180 degrees line near the lower unity gain point and between the closed-loop phase and the -180 degrees near the upper unity gain point. This overshoot phenomenon is inevitable in the inertial feedback systems because the amplification near the unity gain points happens for phase margin less than 60 degrees and most of the servos are designed with less phase margin because the increase in the phase margin decreases the gain which reduces the performance of the servo system. Here, the designer is advised to compromise between the servo gain and the phase margin. The solution offered here to reduce the effect of these unwanted overshoots is to use a phase lag and a phase lead compensators. The phase lag is addressed to the low frequency unity gain point and the phase lead is addressed to the high frequency unity gain point. The phase lag added to the feedback compensator serves to increase the compensation gain which results in decreasing the closed loop magnitude (overshoots) near to the low frequency unity gain point. The phase lead added at high frequency unity gain point shifts the phase of the closed-loop away from the line of -180 degrees which increases the phase margin and assures higher stability conditions. The use of the Lag-Lead filter is illustrated in the next section.

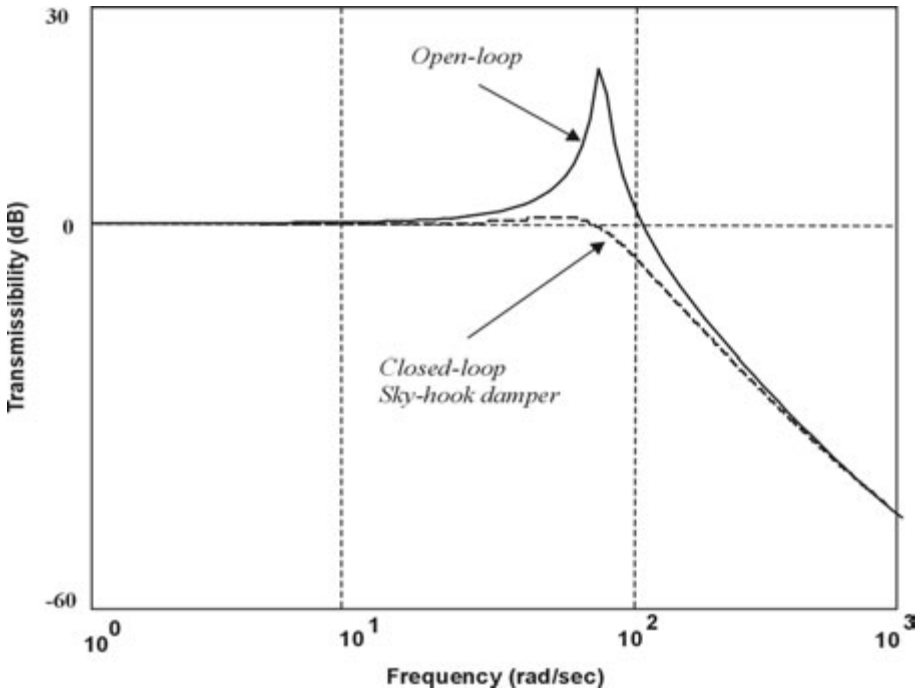

Figure 2.20: *Displacement transmissibility of a soft single-degree-of-freedom isolator with control (dashed line) and without control (solid line) using sky-hook damper*

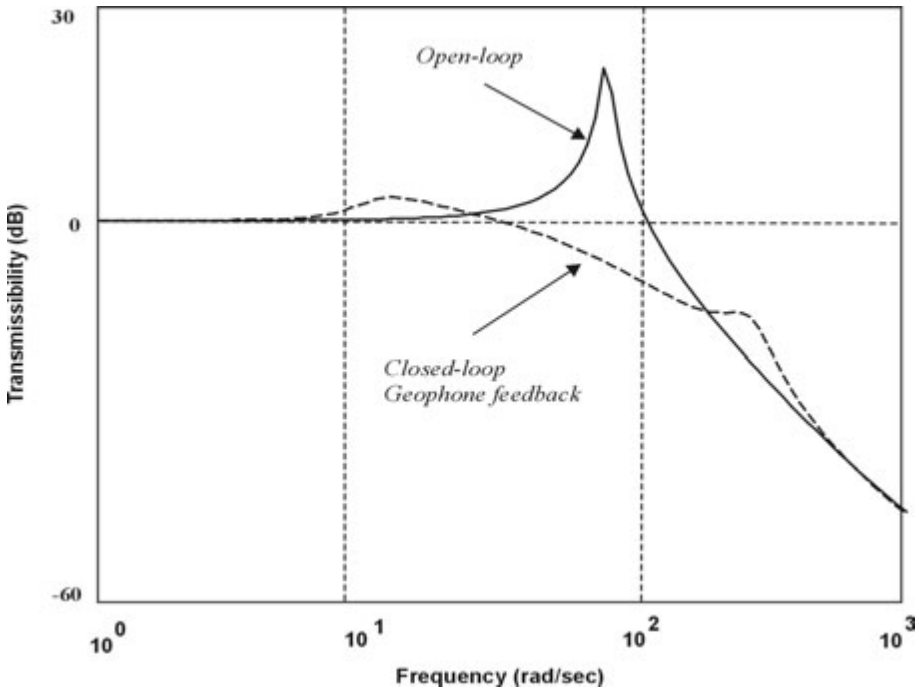

Figure 2.21: *Displacement transmissibility of a soft single-degree-of-freedom isolator with control (dashed line) and without control (solid line) using geophone feedback with Lag-Lead compensator*

2.7 Lag-Lead control using force feedback

The effect of the control law on the transmissibility of a single axis isolator is given by Equ.(2.21). In the project of the ULB soft Stewart platform (chapter 3), two decentralized feedback control laws have been tested; the Integral Force Feedback control (discussed earlier in this chapter) and the Lag-Lead control discussed here. Similar to the comparison between the sky-hook damper and the IFF discussed earlier in this chapter, the Lag-Lead compensator with force feedback is compared here to the geophone velocity feedback discussed in the previous section. The difference is that, although, a force feedback is used here but the stability is not guaranteed as it is in the IFF.
Consider the single-axis system shown in Fig.2.22, where the two rigid bodies are connected by an isolator and a force sensor is used to measure the force acting on the sensitive payload M. The open-loop transfer function F/F_a can be expressed by the equation

$$G(s) = \frac{F(s)}{F_a(s)} = \frac{Ms^2 x_c(s)}{F_a} = \frac{mMs^2}{mMs^2 + k(M+m)} \tag{2.26}$$

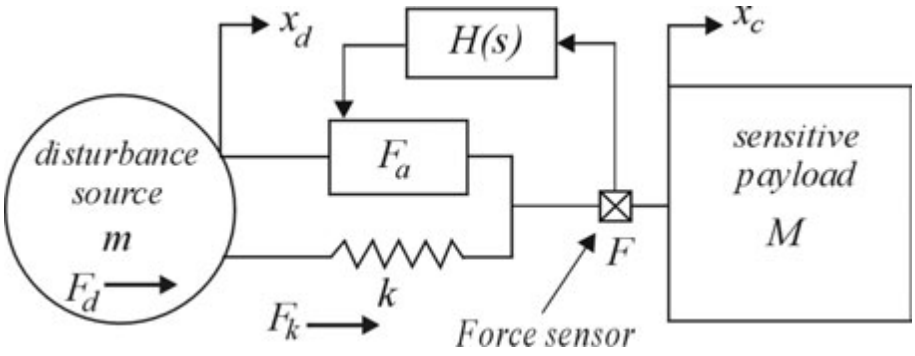

Figure 2.22: *A single-axis isolator using Lag-Lead feedback control technique*

This control technique is similar to the IFF technique but instead of using integral control in the feedback loop we use another compensator consisting of the following:

- High-pass filter HPF at 1 Hz, before the corner frequency of the isolator to attenuate the system at low frequency reducing the influence of the low frequency disturbances. If ω_{hpf} and ξ_{hpf} are the cut-off frequency and the damping ratio of the high-pass filter, respectively, then the HPF transfer function reads

$$HPF = \frac{s^2}{s^2 + 2\xi_{hpf}\omega_{hpf}s + \omega_{hpf}^2} \tag{2.27}$$

- Low-pass filter LPF at 11 Hz, beyond the corner frequency of the isolator to roll off the system at high frequency, increasing the isolation performance. If ω_{lpf} and ξ_{lpf} are the cut-off frequency and the damping ratio of the low-pass filter, respectively, then the LPF transfer function reads

$$LPF = \frac{\omega_{lpf}^2}{s^2 + 2\xi_{lpf}\omega_{lpf}s + \omega_{lpf}^2} \tag{2.28}$$

- Lag compensator near to the HPF to improve the transient response at low frequency. If z_{lag} and p_{lag} are, respectively, the zero and the pole of the Lag compensator ($z_{lag} > p_{lag}$), its transfer function reads

$$LAG = \frac{s + z_{lag}}{s + p_{lag}} \tag{2.29}$$

- Lead compensator after the LPF to increase the stability margin of the closed-loop system. If z_{lead} and p_{lead} are, respectively, the zero and the pole of the Lead compensator ($z_{lead} < p_{lead}$), its transfer function reads

$$LEAD = \frac{s + z_{lead}}{s + p_{lead}} \tag{2.30}$$

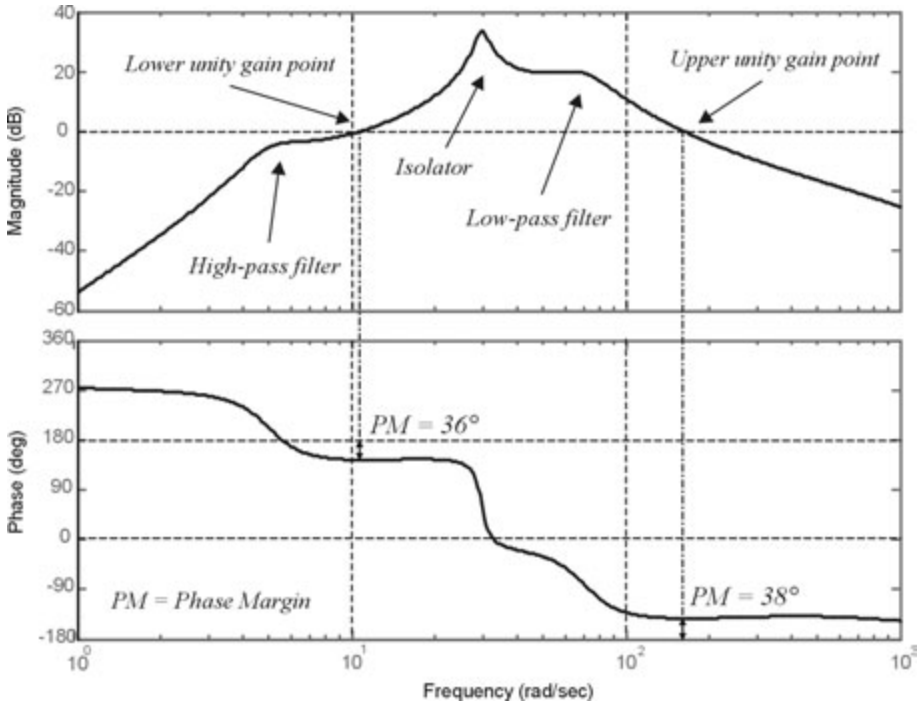

Figure 2.23: *Open-loop FRF between the force F on the payload and the actuation force F_a*

Figure 2.23 shows the open-loop FRF between the force F acting on the sensitive payload and the actuation force F_a with the Lag-Lead compensator connected in series with the plant (GH). From this bode plot, we can see that the gain curve crosses twice over the 0 dB line forming two unity gain points. At the lower unity gain point, the phase is close to +180 and at the upper unity gain point, the phase is close to -180 degrees. This causes a poor transient response at low frequency and a small phase margin at high frequency

point. This justifies the use of the Lag compensator near the low frequency unity gain point and a Lead compensator near the high frequency unity gain point to push the phase curve away from the stability limits. A clear representation of the open-loop system is shown in Fig.2.24 which shows a Nichols chart for the open-loop system. As explained before, Nichols chart magnifies out the vicinity of the stability limits where the 0 dB gain line meets the 180 degrees phase lines. The horizontal distance, on the 0 dB line between the curve and the +180 degrees line is the phase margin at the lower unity gain point and the distance between the curve and the -180 degrees line represents the phase margin at the upper unity gain point.

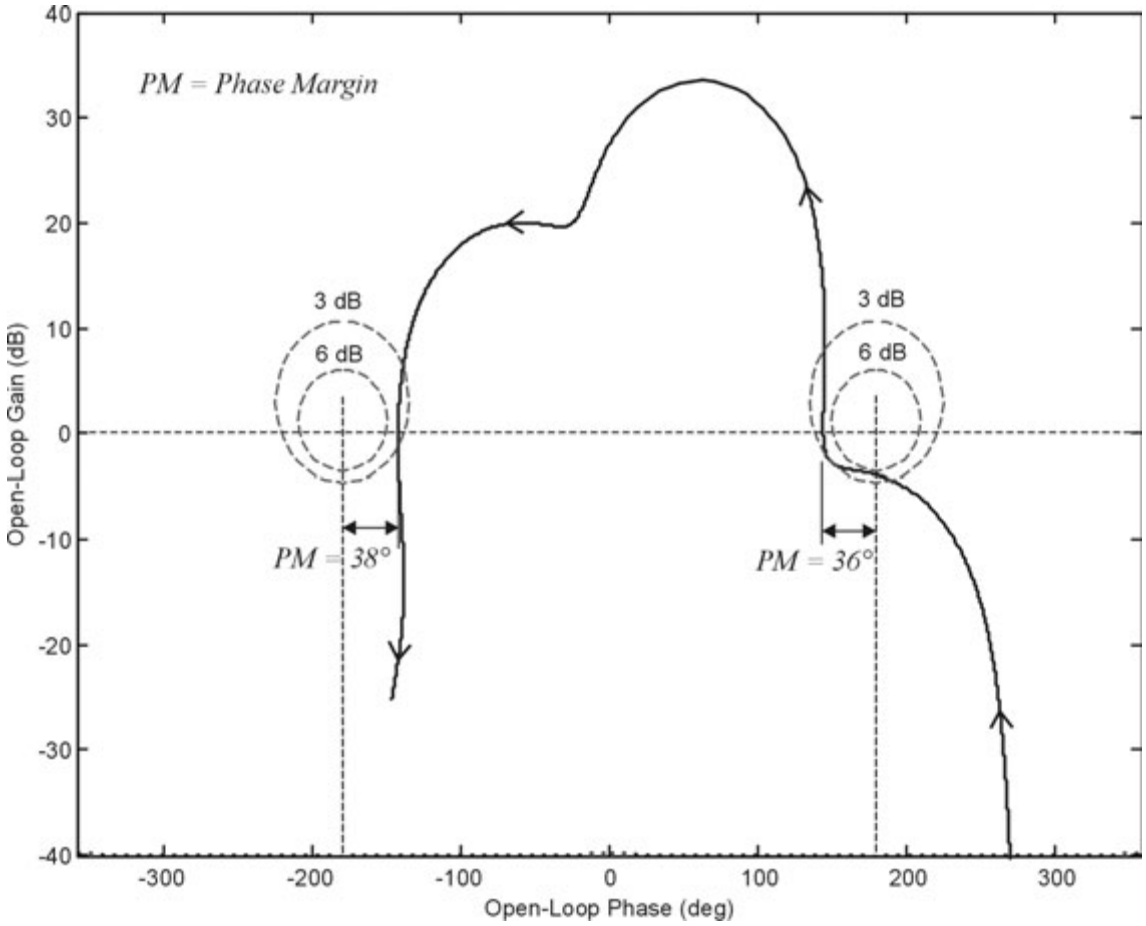

Figure 2.24: *Nichols chart between the open-loop phase and the open-loop gain of the system*

The advantage of using this controller is that it allows to have a lower corner frequency for the closed-loop system and provides better isolation performance along the controller bandwidth. The drawback of this control technique is that it is conditionally stable and it produces overshoots at the unity gain points where the open-loop FRF crosses over the 0 dB line. The reasons and effects of these overshoots are explained extensively in the previous section. In addition, on the contrary to the integral controller, there is

no guarantee that the controller will remain stable when the isolator is inserted in a complicated structure.
Figure 2.25 shows the transmissibility FRF between the displacement of the disturbance source x_d and the displacement of the payload x_c. The open-loop curve represents the transmissibility without control where it levels at 0 dB till reaching the corner frequency of the system. Beyond the corner frequency, the curve attenuates at -40 dB/decade. The closed-loop curve shows the case when the Lag-Lead controller is applied. The two overshoots seen here before and after the corner frequency correspond to the two unity gain points mentioned earlier.

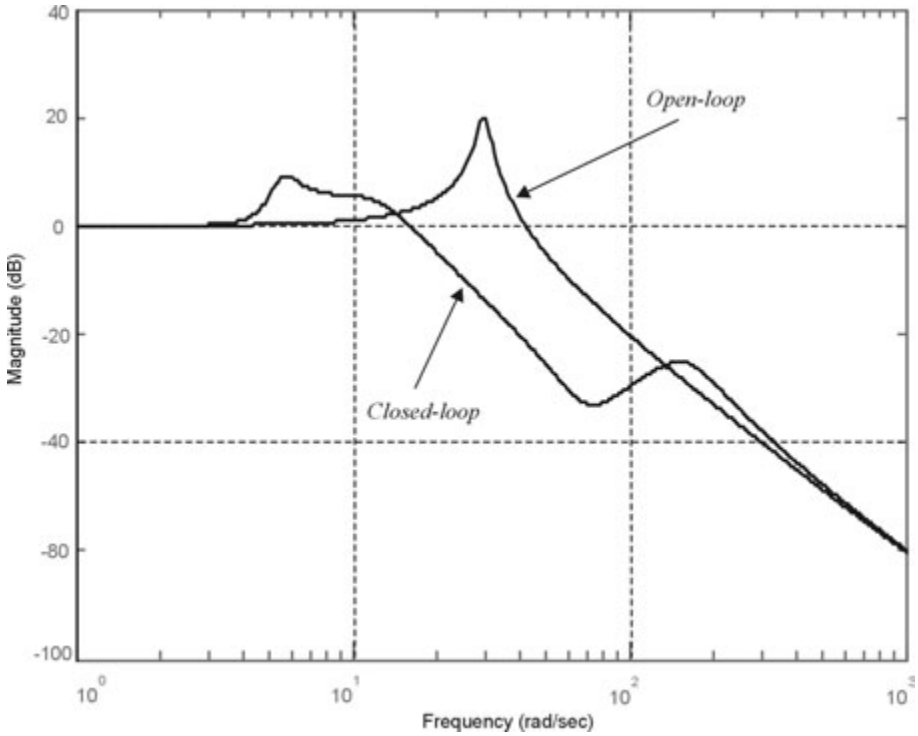

Figure 2.25: *Transmissibility FRF* x_c/x_d

2.8 Alternative concept of single-axis isolator

Reference [22] proposes a good example of vibration isolation instrument using inertial feedback. A symbolic representation of the instrument is shown in Fig.2.26(a). M_1 represents the payload mass to be isolated. Together, M_1 and M_2 form a seismometer; where M_1 is the inside mass and M_2 is the outside proof-mass of the seismometer (M_1 is about ten times heavier than M_2). M_2 is hanged to M_1 by a spring K_2. The system of M_1, M_2 and K_2 is mounted to the base platform through another spring K_1 and a force generator voice coil actuator represented by F.

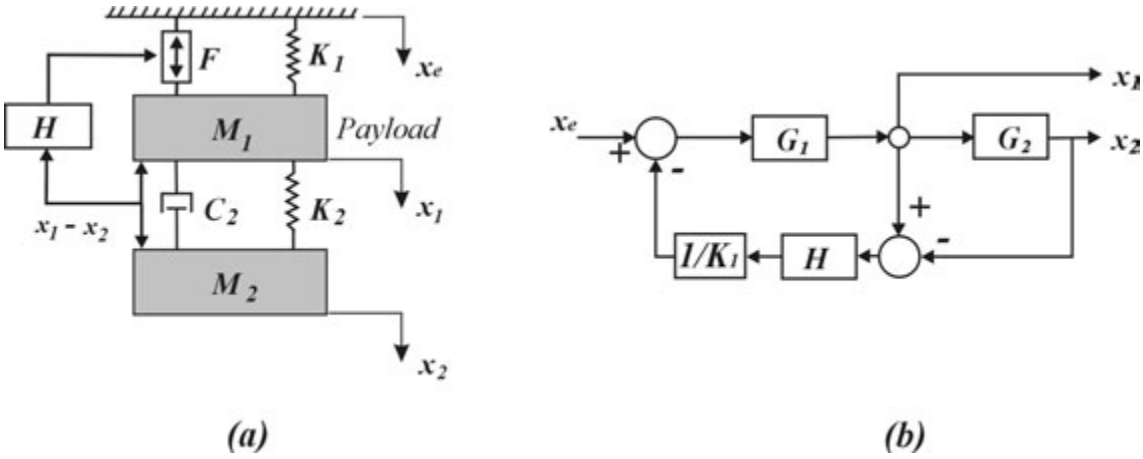

Figure 2.26: *The soft single-axis isolator: (a) A schematic diagram. (b) A block representation*

In order to quiet M_1, the relative motion of the the mass M_2 with respect to M_1 is measured, filtered and fed back to the voice coil actuator. To modelize the system, consider the block diagram shown in Fig.2.26(b); where G_1 represents the passive FRF (x_1/x_e), G_2 represents the passive FRF (x_2/x_1) and H is the filter that will be discussed later in this section. The displacement x_e is the motion of the earth while the terms x_1 and x_2 denote the displacements of the masses M_1 and M_2, respectively.
The system has been modelled and simulated; the plant passive FRF between the force acting on the mass M_1 and the relative diplacement $(x_1 - x_2)$ is shown in Fig.2.27. This FRF shows the two natural frequencies of the system; the first frequency formed by M_2 and K_2 appears at 1.3 rad/sec and the second frequency formed by M_1 and K_1 appears at 8.5 rad/sec.

A cascade filter is used to filter the measured signal of the relative displacement before feeding it back to the voice coil actuator. The FRF of this filter is shown in Fig.2.28; it consists of a high-pass filter, a Lag-Lead filter (a combination of a lag and a lead compensators) and a low-pass filter; with a quality factor $Q = 2$ or less for each filter; the quality factor is the reciprocal of the damping ratio divided by 2 ($Q = 1/2\xi$). Figure 2.29 shows the open-loop FRF of the system with the filter. The high-pass filter is used to increase the roll-off of the gain of the system at low frequency to avoid the quasi-static wandering signals from propagating into the system and the low-pass filter is used at high frequency to cut-off the high-frequency disturbances. The Lag and Lead compensators are used to reduce the effect of the overshoots at the closed-loop unity gain points.

Looking at Fig.2.30, one can see that the closed-loop transmissibility functions are dominated by peak overshoots at the unity gain frequencies. As explained in the previous section, these amplifications near the unity gain frequencies increase the settling time of the system and reduces the stability margin. To reduce the effect of these overshoots, the Lag-Lead compensation is used. The purpose of this compensator is to add a phase lag near the low frequency unity gain point and a phase lead near the high frequency unity

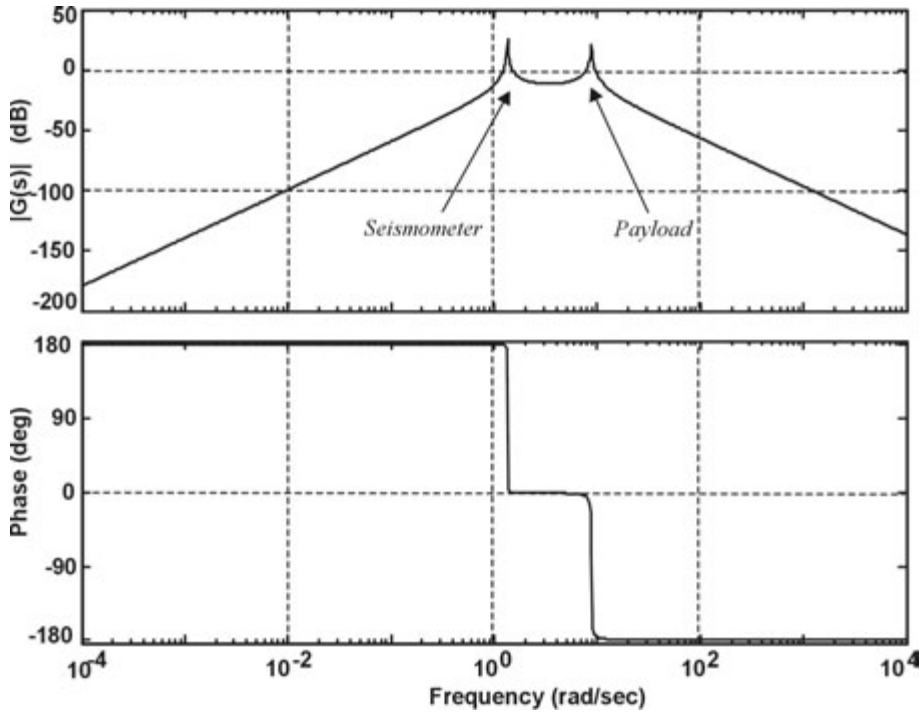

Figure 2.27: *The plant FRF of the soft single-axis isolator between the force on M_1 and the relative displacement $(x_1 - x_2)$.*

gain point. The phase lag serves to increase the compensation gain and, thus, decrease the closed-loop magnitude which, in turn, reduces the overshoot at low frequency. Thanks to the Lag compensation, the low frequency peak is reduced significantly which improves the settling time. The phase lead at the high frequency unity gain point shifts the phase of the closed-loop away from the line of -180 degrees increasing the phase margin and assuring higher stability for the system.

Using the previous notations shown in the block diagram in Fig.2.26(b), it can be easily shown that the closed-loop transfer functions for this system are

$$\frac{x_1}{x_e} = \frac{G_1}{1 + H(G_1 - G_1G_2)} \tag{2.31}$$

$$\frac{x_2}{x_e} = \frac{G_1G_2}{1 + H(G_1 - G_1G_2)} \tag{2.32}$$

Both transfer functions are plotted in the frequency domain in Fig.2.30. The open-loop gain rolls off after the low frequency resonant when we consider the transmissibility (x_2/x_e) while this occurs after the high frequency mode when one is interested in (x_1/x_e). In both cases the increase in the compensator H leads to a decrease in the closed-loop transfer function which rolls off one decade earlier than the lowest resonance.

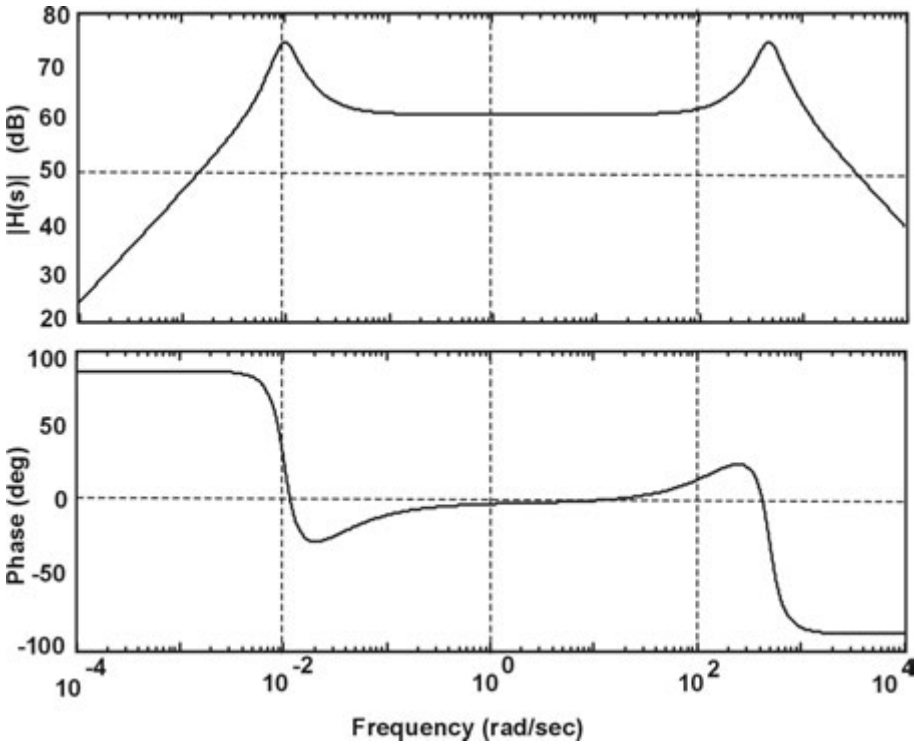

Figure 2.28: *The FRF of the filter used in the feedback loop*

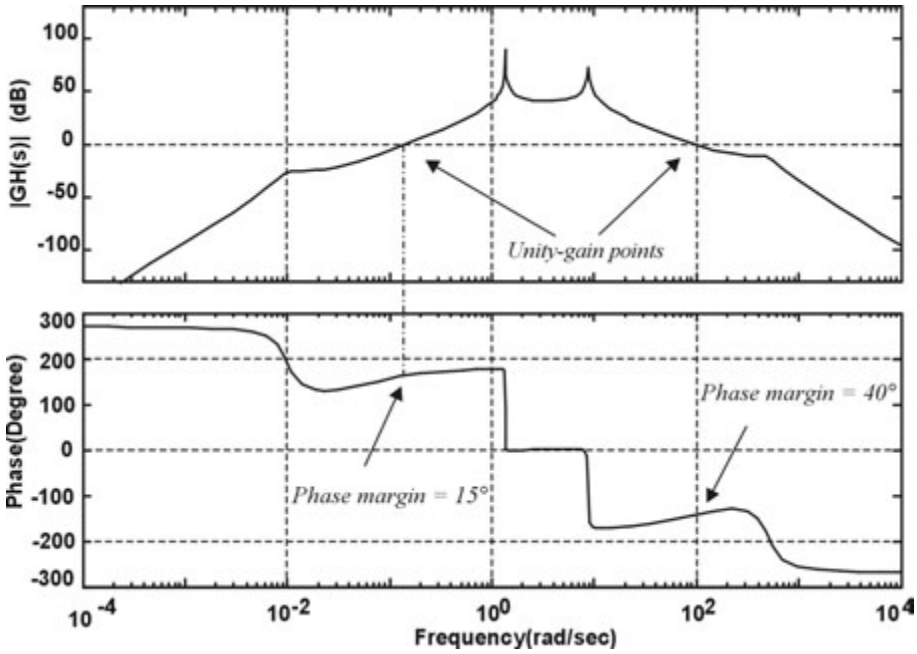

Figure 2.29: *The open-loop FRF of the system with the compensation filter*

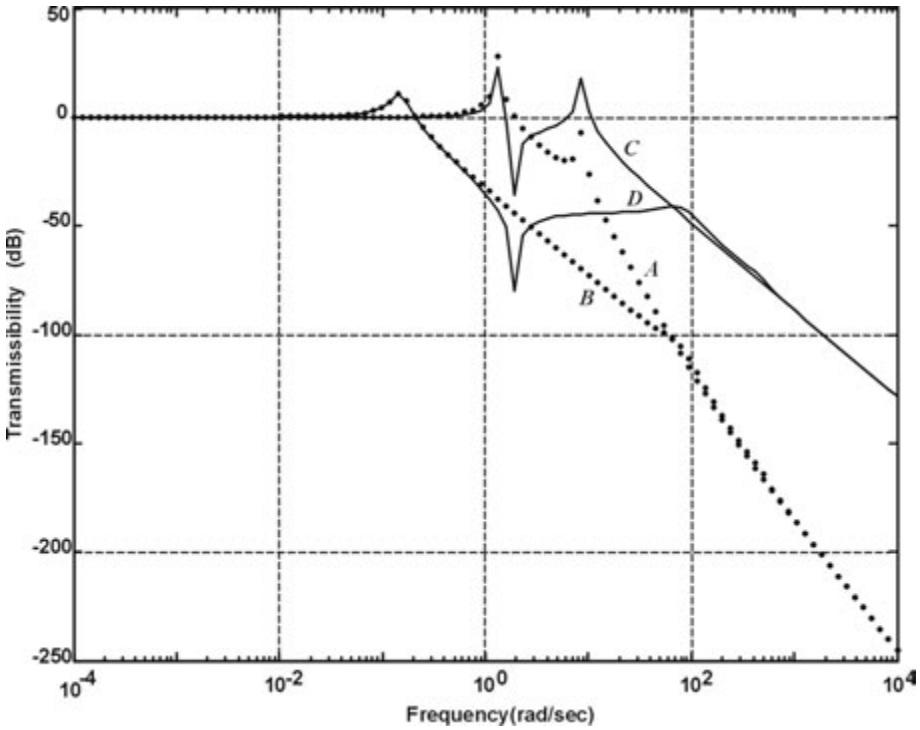

Figure 2.30: *The open-loop and close-loop transmissibility functions of the single-axis soft isolator. (A) Open-loop (x_2/x_e), (B) closed-loop (x_2/x_e), (C) Open-loop (x_1/x_e), (D) Closed-loop (x_1/x_e)*

2.9 Single-axis isolator using a piezo stack

In the previous section, we discussed a single-axis isolation system using a voice coil actuator. Here, we will discuss an alternative single-axis isolation concept based on a piezoelectric actuator. A single-axis vibration isolation system (Quiet pier) has been invented by the Technical Manufacturing Corporation (TMC) to solve the problem of the high corner frequency when using a piezoelectric actuator [23, 24]. This system (in Fig.2.31) consists of a piezoelectric actuator represented by its extension δ and stiffness k, a payload mass m_1 and an intermediate passive mount. The intermediate mount consists of a mass M and an elastomer with a stiffness k_1 and a damping factor c_1. The isolator frequency formed by the stiffness of the actuator k and the intermediate mass M is equal to 1000 Hz. The passive elastomer (represented by the spring k_1 and the dashpot c_1) forms a new resonance with the payload mass m_1 equals to 20 Hz. The two stiffness values, k and k_1, are in series; this results in having the corner frequency of the system corresponding to the lower stiffness k_1.

A geophone velocity sensor is installed at the intermediate mass M. The active control strategy is based on feeding the signal of the geophone back to the piezoelectric actuator after being properly filtered and amplified. This inertial feedback leads to quiet the intermediate mass M which results in isolating the motion x_{c1} of the payload mass m_1 from the seismic disturbance x_d. This system can be represented, in Laplace transform, by the following equations of motion:

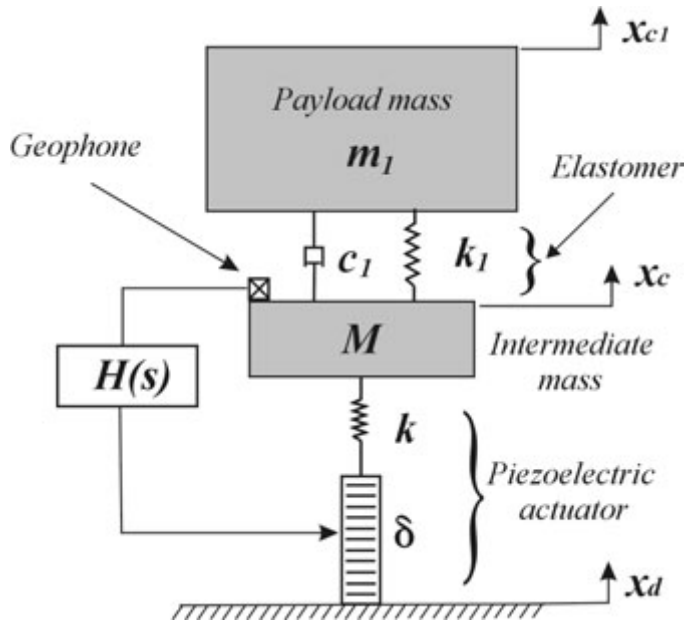

Figure 2.31: *A single-axis isolator using piezoelectric actuator and intermediate passive mount*

The intermediate mass

$$Ms^2x_c = k(x_d - x_c + \delta) - k_1(x_c - x_{c1}) - c_1s(x_c - x_{c1}) \tag{2.33}$$

The payload mass

$$m_1s^2x_{c1} = k_1(x_c - x_{c1}) + c_1s(x_c - x_{c1}) \tag{2.34}$$

The plant FRF between the voltage input to the actuator and the velocity measured at mass M is shown in Fig.2.32. From this FRF, one can see that the resonance formed by the stiffness of the piezoelectric actuator and the intermediate mass M appears at 1000 Hz, while the resonance formed by the passive elastomer and the payload is at 20 Hz. A zero appears just after the low frequency pole. Because of the high mass ratio between the payload and the intermediate mass, where the intermediate mass is about 1/50 to 1/200 of the payload mass, this zero stays close to the low frequency resonance. The FRF of the compensator is shown in Fig.2.33. It contains the geophone dynamics (high-pass filter at 4.5 Hz), a low-pass filter at 300 Hz, and the two lag and lead compensators are designed to be near the high-pass and the low-pass filters respectively.
Figure 2.34 shows the open-loop FRF between the voltage input to the actuator and the velocity measured by the geophone. The gain (magnitude) of the open-loop transfer function climbs at 40 dB/decade then levels at 40 dB when it reaches to 4.5 Hz at the resonance frequency of the geophone. The geophone acts as a second order high-pass filter that cuts the signals off below 4.5 Hz. The high frequency attenuation is achieved by locating a low-pass filter at 300 Hz (before the resonance of the piezoelectric actuator). A lag compensator is placed near the low frequency unity gain point (at 0.2 Hz), and a

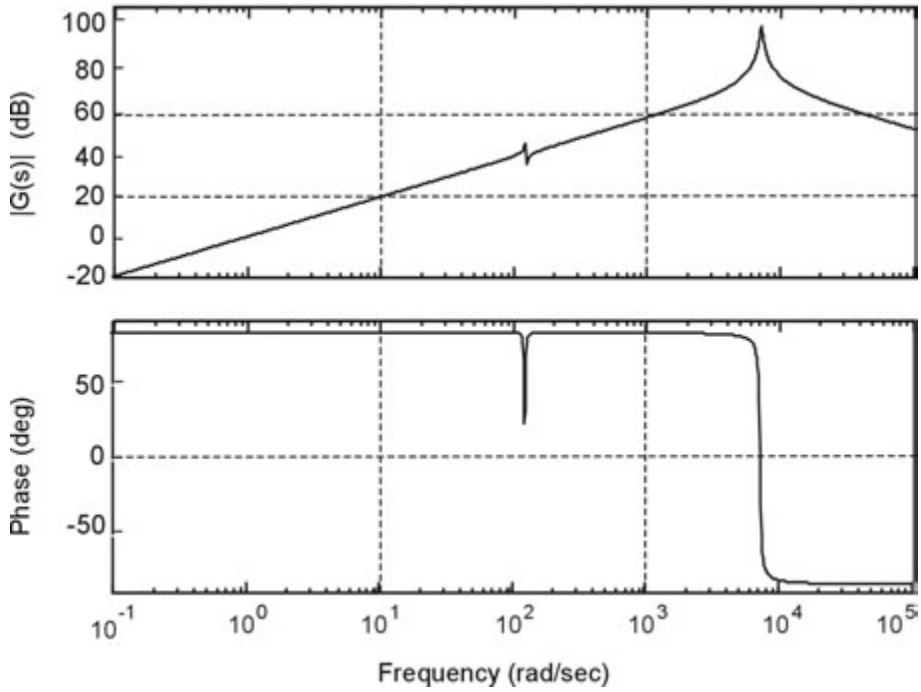

Figure 2.32: *Plant FRF, of the single-axis isolator with intermediate mount, between the voltage input to the actuator and the velocity of the mass M*

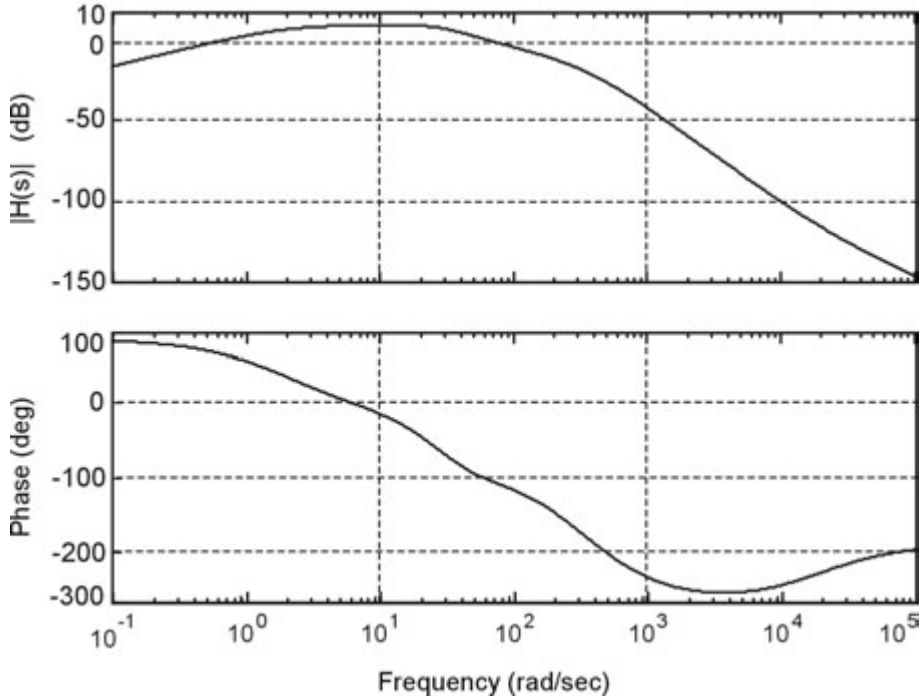

Figure 2.33: *FRF of the compensator*

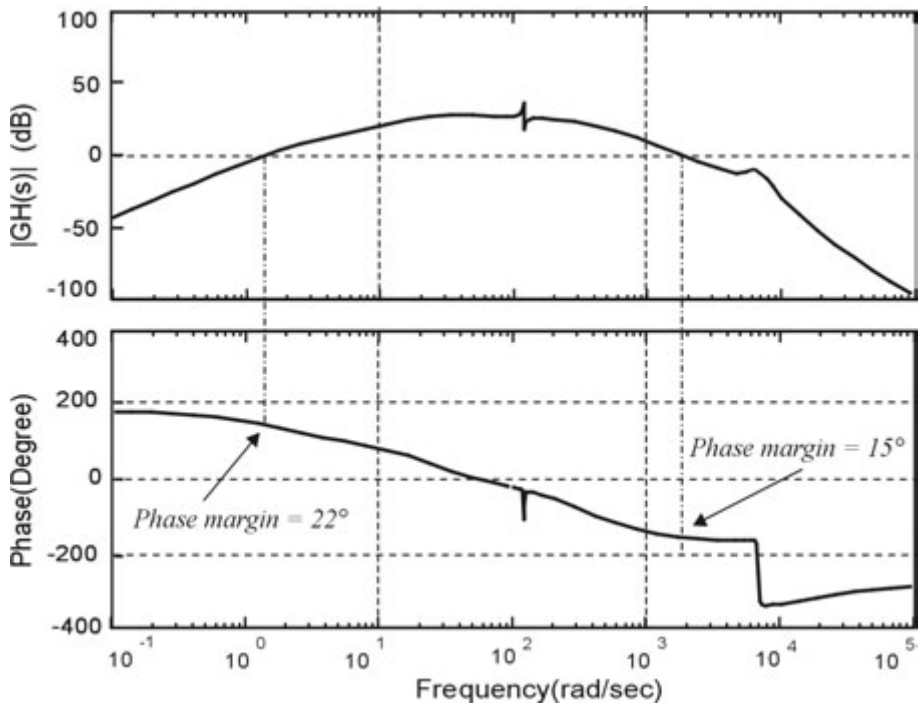

Figure 2.34: *Open-loop FRF of the system, between the voltage input to the actuator and the velocity output of the geophone, with the compensator*

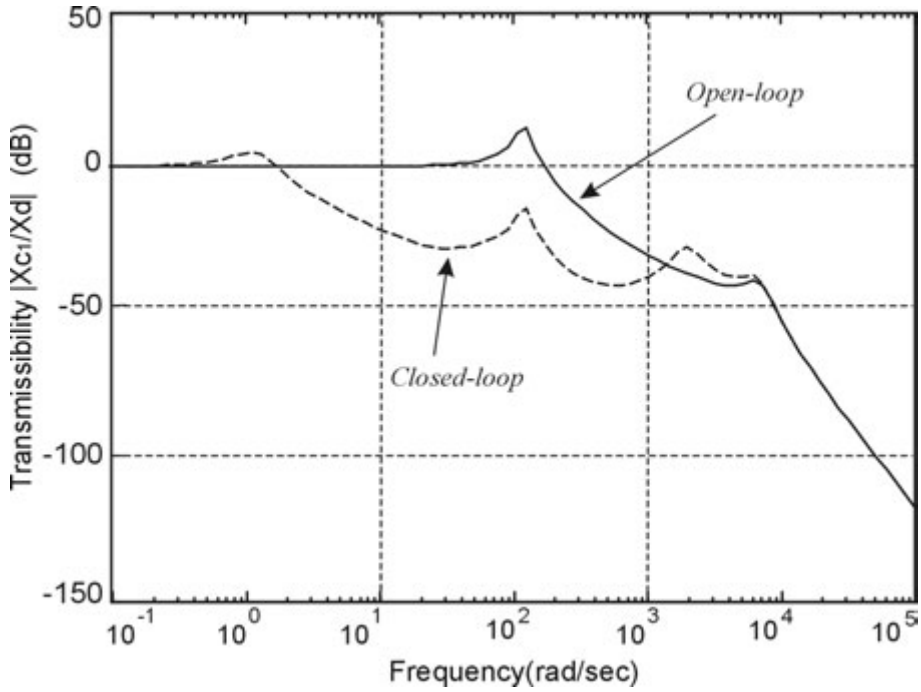

Figure 2.35: *Transmissibility FRF between the seismic diplacement x_d and the payload displacement x_{c1}, with control (closed-loop) and without control (open-loop).*

lead compensator is placed near the high frequency unity gain point (at 350 Hz). The advantage of adding this lag-lead compensation is to reduce the amplifications (overshoots) that appear at the unity gain points when the loop is closed.
Figure 2.35 shows the transmissibility FRF between the seismic disturbance displacement x_d and the sensitive payload displacement x_{c1}. The overshoots caused by inertial feedback can be seen clearly on the two unity gain points of the closed-loop FRF. Using a phase lag compensator near the low unity gain frequency reduced the overshoot which means better transient response and lower settling time. Similarly, using a phase lead compensator near the upper unity gain frequency could increase the phase margin which improves the stability conditions of the system. One can see clearly that despite using a hard piezoelectric actuator, the passive vibration isolation occurs here near the low frequency resonance of the passive mount (20 Hz). Moreover, the closed-loop active vibration isolation occurs much lower than that (at 0.2 Hz) leading the system to have a high isolation performance for a wide band of disturbances.

2.10 References

[1] C. Crede. *Vibration and shock isolation.* John Wiley and Sons Inc., New York, 1951.

[2] W. Thomson. *Theory of Vibration with Applications.* George Allen and Unwin, 1981.

[3] H. Yoshioka, Y. Takashashi, K. Katayama, T. Imazzawa, and N. Murai. An active microvibration isolation system for hi-tech manufacturing facilities. *Journal of Vibration and Acoustics*, 123:269–275, April 2001.

[4] K.Y. Kim and Y.P. Park. Robust vibration control of air-spring isolation table. In *MOVIC 2000*, Sydney, Australia, December 2000.

[5] E.I. Rivin. Principles and criteria of vibration isolation of machinery. *Trans. of the ASME, Journal of Mechanical Engineering*, 101:682–692, October 1979.

[6] S.A. Collins and A.H. von Flotow. Active vibration isolation for spacecraft. In *42nd Congress of the International Astronautical Federation*, volume IAF-91-289, Montreal, Canada, October 1991.

[7] BARRY Controls. *Isolator selection guide.*

[8] TECH Products Corporation. *Vibration and noise control products.*

[9] GMT. *Gummi-Metal-Technik catalogue.*

[10] PAULSTRA. *Paulstra and Hutchison Catalogue.*

[11] R.M. Chalasani. Ride performance potential of active suspension systems - PART 1: Simplified analysis based on a quarter-car model. In *Symposium on Simulation and Control of Ground Vehicles and Transportation Systems*, pages 187–204. ASME, December 1986.

[12] C.E. Kaplow and J.R. Velman. Active local vibration isolation applied to a flexible space telescope. *AIAA J. Guidance and Control*, 3(3):227–233, May-June 1980.

[13] D. Karnopp and A.K. Trikha. Comparative study of optimization techniques for shock and vibration isolation. *Trans. of ASME, Journal of Engineering for Industry*, pages 1128–1132, November 1969.

[14] D. Karnopp, M.J. Crospy, and R.A. Harwood. Vibration control using semi-active force generators. *Trans. of ASME, Journal of Engineering for Industry*, pages 619–629, May 1974.

[15] A. Preumont, A. François, F. Bossens, and A. Abu-Hanieh. Force feedback vs. acceleration feedback in active vibration isolation. *Journal of Sound and Vibration*, 257(4), October 2002.

[16] A. Preumont. *Vibration Control of Active Structures*. Kluwer Academic Publishers, Netherlands, 2nd edition, 2002.

[17] G. D. Martin. *On the Control of Flexible Mechanical Systems*. PhD thesis, Stanford University, 1978.

[18] A. Abu Hanieh, M. Horodinca, and A. Preumont. A soft-actuator active hexapod for the purpose of vibration isolation. In *International Conference on Noise and Vibration Engineering*, KUL, Leuven, Belgium, September 2002.

[19] M. Horodinca, A. Abu Hanieh, and A. Preumont. A soft six degrees of freedom active vibration isolator based on Stewart platform. In *International Symposium on Active Control of Sound and Vibration (Active 2002)*, Southampton, UK, July 2002.

[20] Z. Rahman, J. Spanos, and D. Bayard. Multi-tone adaptive vibration isolation of engineering structures. In *36th AIAA/ASME/ASCE/AHS Structures, Structural Dynamics and Materials Conference*, New Orleans, USA, April 1995.

[21] Z. Rahman, J. Spanos, and G. Blackwood. Active narrow-band vibration isolation of large engineering structures. In *Proceedings of the First World Conference on Structural Control*, Pasadena, USA, August 1994.

[22] P. Nelson. An active vibration isolation system for inertial reference and precision measurement. *Rev. Sci. Instrm, American Institute of Physics.*, 62(9), September 1991.

[23] TMC. Technical background. Technical report, Technical Manufacturing Corporation.

[24] D. Schubert, A. Beard, S. Shedd, M. Earls, and A. von Flotow. Stiff actuator active vibration isolation system. In *United States Patent No. 5,660,255*. August 1997.

Chapter 3

Six-axis active isolation

3.1 Introduction

In this chapter, we intend to discuss the six-axis vibration isolation, particularly, the isolators based on Stewart platform. A detailed discussion about Stewart platform will be given in this chapter, concentrating on the cubic architecture, the general kinematics and dynamic modelling. To validate experimentally the multi-axis vibration isolation, a new six-axis Stewart platform has been designed, manufactured and tested. This design is based on implementing six soft electrodynamic (voice coil) actuators in the six legs of the hexapod. A brief review of the current efforts done by other groups in building soft Stewart platforms is shown here too. The general technological assembly of the ULB soft Stewart platform will be explained discussing extensively the design of the actuators, the membranes and the flexible joints. A finite element model and some analytical governing equations will be used to analyse the effect of the flexible joints on the control authority. Experimental results will be reviewed at the end of the chapter.

3.2 Stewart platform

A Stewart platform mechanism is an hexapod system consisting of six d.o.f. parallel manipulator with variable link length. It is named upon D. Stewart who used this configuration in 1965 to design a six d.o.f. flight simulator for training of pilots [1]. Others claimed reaching the invention before Stewart [2]. However, the idea seems to have been invented by V. Gough more than ten years before (in 1955), who designed a tyre testing machine based on the cubic configuration of a six d.o.f. hexapod [3] (the cubic configuration will be discussed in the next section).
In the context of large space structures discussed here (Fig.3.1) [4, 5], such a platform can be used as:

- Active mount for quiet components.
- Isolation mount for a disturbance source.
- Active structural element of trusses for vibration control or geometrical reconfiguration.

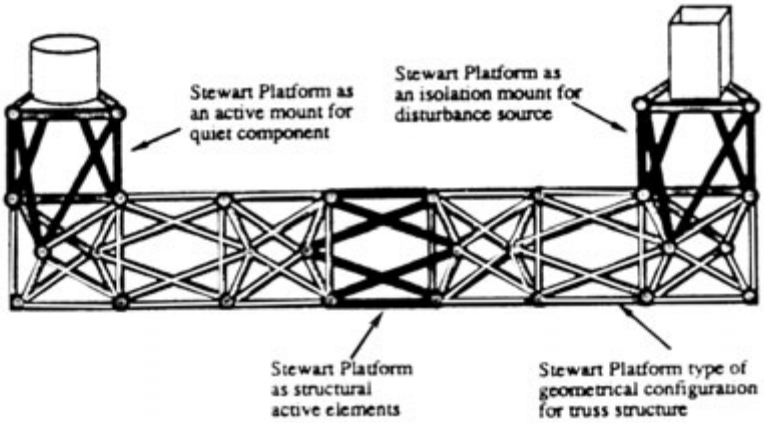

Figure 3.1: *Various uses of a Stewart platform in a truss structure(from [4])*

Stewart platforms can be classified into two main groups according to the stiffness of the legs; stiff and soft. The *stiff* design typically involves piezoelectric or magnetostrictive legs whose extension can be controlled, while in the *soft* design, each leg acts essentially as an axial spring in parallel with a voice coil actuator.

3.3 The cubic architecture

Stewart platforms are very popular parallel manipulators [6, 7, 8]. The dexterity of the mechanism and its accuracy depends very much on its nominal geometry; various optimal architectures have been developed [9]. The specific application considered here is fairly different from most applications considered in robotic manipulators, in the sense that the link elongations are very small, so that the kinematic configuration remains almost unchanged. Thus, the Jacobian remains constant and can be evaluated from the nominal configuration. The following characteristics play an important role in the design of a Stewart platform for active vibration isolation and precision pointing:

- Uniformity of control capability in all directions.
- Uniform stiffness in all directions.
- Minimum cross-coupling amongst actuators.
- Simple kinematic and dynamic analysis.
- Simple mechanical design (minimum number of different components).
- Availability of collocated actuator/sensor pairs.
- Minimum rotational stiffness of the spherical joints (ideally zero).

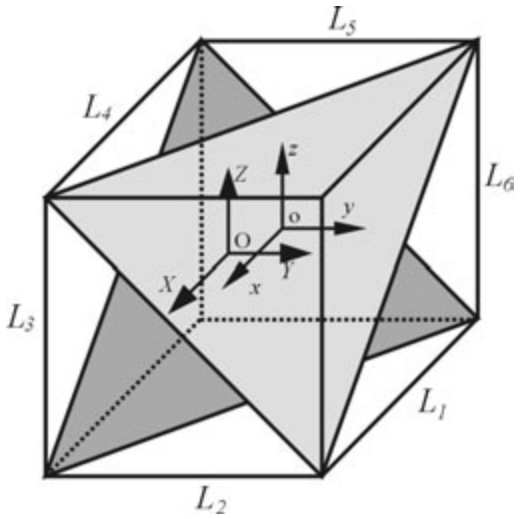

Figure 3.2: *Cubic configuration of a Stewart platform*

The "cubic configuration" was invented by Gough [3] and has been used by Intelligent Automation Inc. (IAI) [4] to fulfill most of the above properties. The nominal configuration is obtained by cutting a cube by two planes as illustrated in Fig.3.2; these planes constitute the base plates of the Stewart platform. The edges of the cube connecting the base plates constitute the six legs of the platform. The cubic configuration has other interesting features:

- The adjacent legs are orthogonal to each other resulting in a decoupled control action in the three translational directions X, Y, Z, (Fig.3.2); actuators L_1 and L_4 control the translation in the X direction, etc ... This feature also leads to a maximum uniformity of control authority in all direction.
- The Stewart platform is symmetrical in its nominal configuration and all legs are identical.

3.4 Kinematics and pointing performance of Stewart platform

3.4.1 Dimensioning of the cubic Stewart platform

Consider the schematic drawing shown in Fig.3.3 that represents the nominal configuration of a cubic Stewart platform. Figure 3.3(a) is the cross-section through the XZ-plane and Fig.3.3(b) shows the top view of the hexapod; the two triangles in dashed lines here connect the points of anchorage of the legs on the two plates. The overall length of the leg L is the basic parameter out of which all the kinematics are calculated:

$$L = l + \frac{2e}{sin\theta} \tag{3.1}$$

where l is the nominal length of the leg (active strut), e is the thickness of one of the plates and θ is the nominal inclination angle of the leg in the vertical plane including

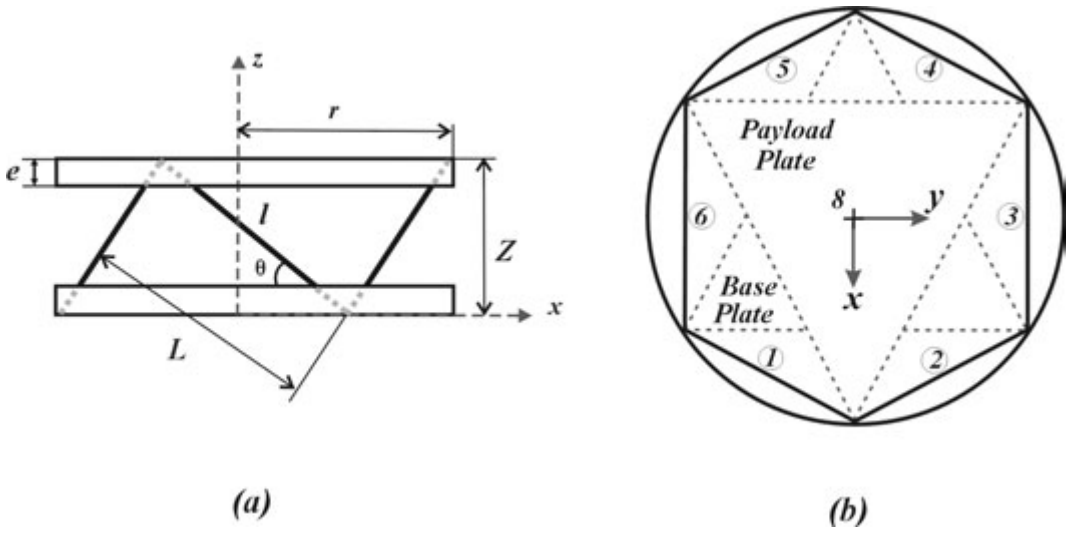

Figure 3.3: *Schematic drawing of Stewart platform; (a) side section, (b) top view*

the leg; θ is constant in the cubic configuration hexapods, regardless any change in the dimensions, and equals to 35.26 degrees. r is the radius of the circle including the points of anchorage of the legs on the plates which are the points of intersection of the adjacent legs. From the geometry:

$$r^2 = L^2 - Z^2 \tag{3.2}$$

This leads to the following values:

$$\frac{r}{L} = cos\theta = \sqrt{\frac{2}{3}}$$

$$\frac{Z}{L} = sin\theta = \sqrt{\frac{1}{3}}$$

3.4.2 Pointing performance

The Jacobian matrix J (defined in Appendix A) allows to transform the pointing control requirements (in terms of $\delta\chi$) into length requirements δq of the platform legs

$$\delta q = J\delta\chi \tag{3.3}$$

where $\chi = \{x, y, z, \theta_x, \theta_y, \theta_z\}$ is the translations and rotations of the mobile plate and $q = \{q_1, ..., q_6\}$ is the extensions of the six legs of the hexapod. This decoupling transformation produces 6 independent actuator commands for the individual legs (Fig.3.4). Most often, the pointing control involves only two pointing angles; in this case, the Stewart platform has some built-in redundancy which can be exploited to account for possible actuator failure, if some of the legs are locked with a fixed length [10, 11, 12, 13]. In these configurations, the partial Jacobian is no longer square, but the decoupling matrix D is the pseudo-inverse of the appropriate partial Jacobian matrix.

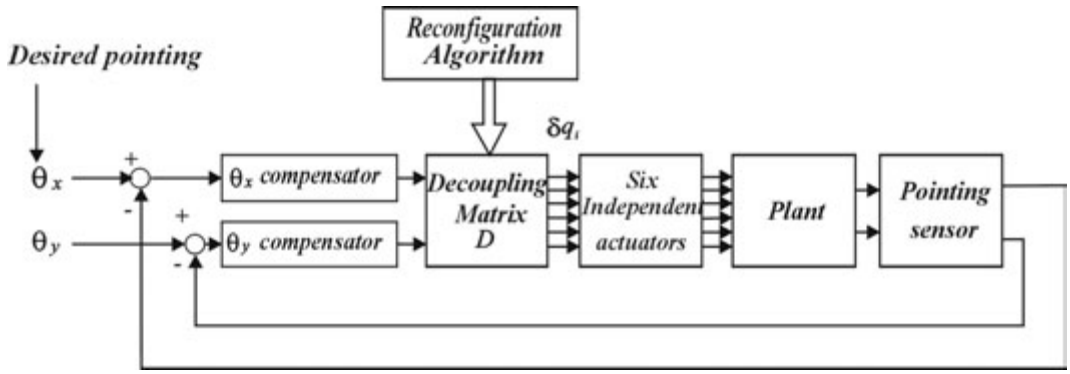

Figure 3.4: *Block diagram of pointing control problem including reconfiguration algorithm in case of actuator failure*

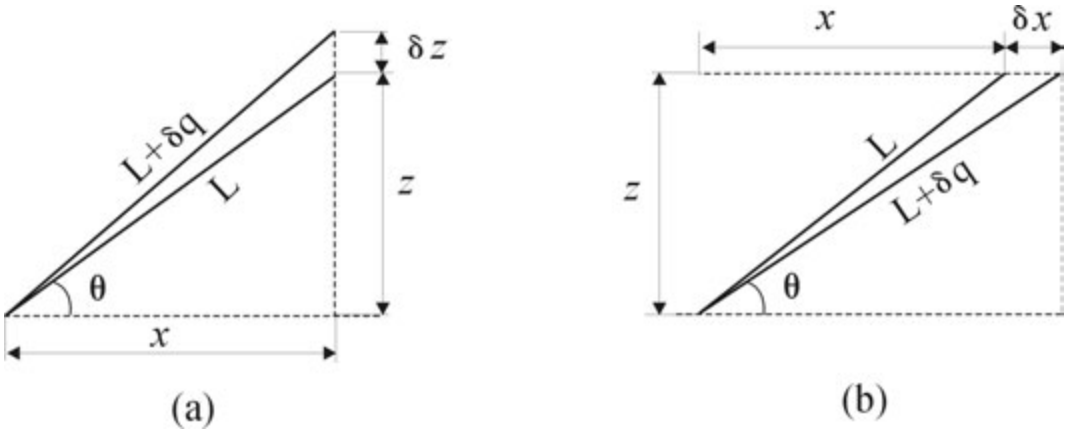

Figure 3.5: *Leg configuration for performance calculations: (a) deformation of all the legs together to give a pure vertical motion, (b) deformation of any two parallel legs to give a pure horizontal motion*

Several algorithms have been put forward to solve the kinematics of the Stewart platform for pointing purposes, some of them are discussed in [14, 15, 16, 17]. To estimate the pointing performance of Stewart platform, consider Fig.3.5(a) which shows the motion done by all the six legs together to provide a pure vertical (piston) motion (let's call it z). Figure 3.5(b) shows the motion done by two parallel legs to provide a pure horizontal (shear) motion (let's call it x). Consider moving the mobile plate in a pure piston motion; in this case, all the actuators elongate with the same length. One can calculate, analytically, the relation between the elongation of the leg δq and the piston motion δz from trigonometric analysis

$$x^2 = L^2 - z^2 = (L + \delta q)^2 - (z + \delta z)^2 \tag{3.4}$$

This leads to the relation

$$\delta z \approx \sqrt{3}\delta q \tag{3.5}$$

In the same manner, when one needs to move the platform in a pure shear motion, the

two parallel legs that are parallel to the direction of motion will elongate together to define this motion. The full-stroke of these two legs will be accompanied by a half-stroke elongation of each of the other four legs. Applying the trigonometric relations again we find

$$z^2 = L^2 - x^2 = (L + \delta q)^2 - (x + \delta x)^2 \tag{3.6}$$

This leads to the relations

$$\delta x \approx \sqrt{\frac{3}{2}}\delta q \tag{3.7}$$

and

$$\delta y \approx \sqrt{2}\delta q \tag{3.8}$$

The pure rotational motion is defined by the elongation δq normalized by the nominal length of the leg L. In the case of a pure rotation around the x-direction (if the x-axis passes through an anchorage point of two adjacent legs), the following relation defines the rotated angle $\delta\theta_x$:

$$\delta\theta_x \approx \sqrt{6}\frac{\delta q}{L} \tag{3.9}$$

and $\delta\theta_y$ is given by:

$$\delta\theta_y \approx \frac{3}{\sqrt{2}}\frac{\delta q}{L} \tag{3.10}$$

To give a pure rotation around the vertical central axis, all the legs should elongate in the way shown in Fig.3.5(b) but in alternative way (e.g. legs 1, 3 and 5 make a positive motion and legs 2, 4 and 6 make a negative motion or vice versa). The pure rotation around the vertical axis is proportional to the absolute extension/contraction of one of the legs normalized by the nominal length of the leg:

$$\delta\theta_z \approx \sqrt{3}\left|\frac{\delta q}{L}\right| \tag{3.11}$$

Table 3.1 shows the maximum pure translations and rotations in the different degrees of freedom. s is the total stroke of the actuator, δq_i is the elongation in the i^{th} leg and $\delta\chi$ is the maximum pure translations and rotations travelled by the center of the upper plate. When the motion is a combination of several directions it becomes more complicated. A simple optimization technique can be made to calculate the different configurations that give the maximum motions in the six d.o.f. of the platform. The maximum displacements and rotations with the corresponding leg configurations are shown in table 3.2. Note that the maximum motions shown in this table are not pure motions but they are coupled with other motions at the same time.

$\delta\chi$	δq_1	δq_2	δq_3	δq_4	δq_5	δq_6
$x_{pure} = \sqrt{\frac{3}{2}}s$	$s/2$	$s/2$	$-s$	$s/2$	$s/2$	$-s$
$y_{pure} = \sqrt{2}s$	s	$-s$	0	s	$-s$	0
$z_{pure} = \sqrt{3}s$	s	s	s	s	s	s
$\theta^x_{pure} = \sqrt{6}\frac{s}{L}$	0	0	s	s	$-s$	$-s$
$\theta^y_{pure} = \frac{3}{\sqrt{2}}\frac{s}{L}$	$-s$	$-s$	$s/2$	$s/2$	$s/2$	$s/2$
$\theta^z_{pure} = \sqrt{3}\frac{s}{L}$	s	$-s$	s	$-s$	s	$-s$

Table 3.1: *Maximum pure translations and rotations travelled by the mobile plate and the corresponding leg configuration (s = the actuator stroke and L = the nominal length of the leg) (see Fig.3.3 for reference axes and strut numbering)*

$\delta\chi$	δq_1	δq_2	δq_3	δq_4	δq_5	δq_6
x_{max}	$-s$	$-s$	$-s$	s	s	$-s$
y_{max}	s	$-s$	$-s$	s	$-s$	s
z_{max}	s	s	s	s	s	s
θ^x_{max}	$-s$	s	s	s	$-s$	$-s$
θ^y_{max}	$-s$	$-s$	$-s$	s	s	$-s$
θ^z_{max}	s	$-s$	s	$-s$	s	$-s$

Table 3.2: *Maximum coupled translations and rotations travelled by the mobile plate and the corresponding leg configuration (s = the actuator stroke and L = the nominal length of the leg) (see Fig.3.3 for reference axes and strut numbering)*

3.5 Current effort in soft Stewart platforms

Table 3.3 shows an overview of existing projects on soft Stewart platforms and a comparison between their main characteristics. The Jet Propulsion Laboratory (JPL) started with the Six Axis Stewart Strut Experiment (SASSIE) [18]. Other projects took place in other research centers; Hood Technology in cooperation with the University of Washington (HT-UW) developed an hexapod with a long stroke voice coil actuator and several types of feedback sensors [19, 20, 21]. Honeywell developed another type of Stewart platform with 1 Hz corner frequency to provide a wide band of vibration isolation using accelerometers as the feedback sensors [22]. Other types of hexapods have been designed and manufactured by the Naval Postgraduate School [23, 24], the University of Wyoming [10, 11, 12] and CSA Engineering Inc. The last Stewart platform in table 3.3 has been designed, manufactured and tested at ULB in the Active Structure Laboratory (ASL). The ULB soft hexapod (Fig.3.7) is based on the cubic configuration using soft voice coil actuators with a stroke of ± 1500 μm and force feedback sensors. Decentralized force feedback control strategy is used to damp actively the rigid body modes of the mobile plate. The corner frequency of the hexapod is 4.5 Hz [25, 26].

The design of the leg is the main feature to take into account in the comparison between the different designs of Stewart platforms. Figure 3.12 shows a comparison between three different leg configurations. In the design of the JPL, one can see that the bending motion of the leg is held in the flexible joints located at the two ends of the leg and the mobile plate is offloaded by using an internal spring which increases the corner frequency of the system. The coil is guided by two flexible membranes but it adds some passive damping to the axial motion of the actuator. The design of the ULB has two major differences from that of the JPL; there is no internal spring to compensate for the gravity force which allows to have a lower corner frequency and there is no passive damping (no eddy current in the coil) inside the actuator, which increases the possibility to get a higher attenuation rate at high frequency. The design of the HT-UW adds a new concept by fixing the permanent magnet to the base plate and installing the joint after the coil but the drawback here is that the air gap in the actuator should be bigger to give more clearance for the coil to move which reduces the performance of the actuator. Another contribution in the design of the HT-UW is that it adds a new spring k_2 in series with the leg because the joints are elastomers which aims at increasing the attenuation at high frequency.

Summary of current soft Stewart platforms

Hexapod	Actuator	Actu. stroke	Feedback sensor	Passive damping	Corner frequency	Gravity compensation	config-uration	Control strategy	Joints
JPL [18], Fig.3.6	**Voice Coil**	**±250 μm**	**Load cells**	**Eddy current**	**10-20 Hz**	**Internal suspension**	**Cubic**	**Decentral. Force Feedback**	**Flexible joints**
Hood Tec./Univ. of Washington [19], Fig.3.8	**Voice Coil**	**±5000 μm**	**Load cell Geophones LVDT**	**Elastomer**	**3 Hz**	**External suspension**	**Cubic**	**Decentral. feedback**	**Elastomers**
Honeywell [22], Fig.3.9	**Voice Coil**	**±1000 μm**	**Accelero-meters**	**Fluid**	**1 Hz**	**External suspension**	**Not cubic**	**Feedback**	**Bi-axial flexures**
Naval Post-graduate school [23], Fig.3.10	**Voice coil**	**±5000 μm**	**Accelero-meters**	**Eddy current, friction**	**12 Hz**	**None**	**Not cubic**	**Decentral. feedforward**	**Ball joints**
Univ. of Wyoming [10], Fig.3.11	**Voice coil**	**±630 μm**	**Load cells**	**Eddy current**	**10-20 Hz**	**Internal suspension**	**Cubic**	**Decentral. force feedback**	**Elastomers**
CSA (soft) [19]	**Electro-magnetic**	**±20 μm**	**Payload geophones**	**—**	**15 Hz**	**None**	**—**	**Feedback**	**—**
ULB (soft) [25], Fig.3.7	**Voice coil**	**±1500 μm**	**Force sensors**	**None**	**4.5 Hz**	**External suspension**	**Cubic**	**Decentral. force feedback**	**Flexible joints**

Table 3.3: *Comparison between several types of soft hexapods*

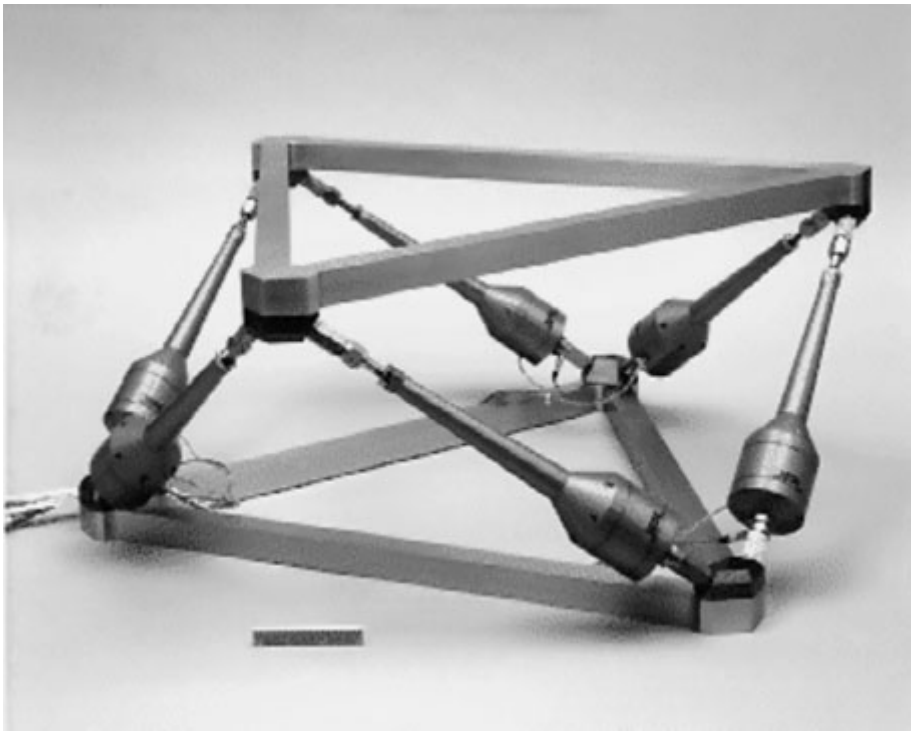

Figure 3.6: *JPL Hexapod [18]*

Figure 3.7: *ULB soft Hexapod [25]*

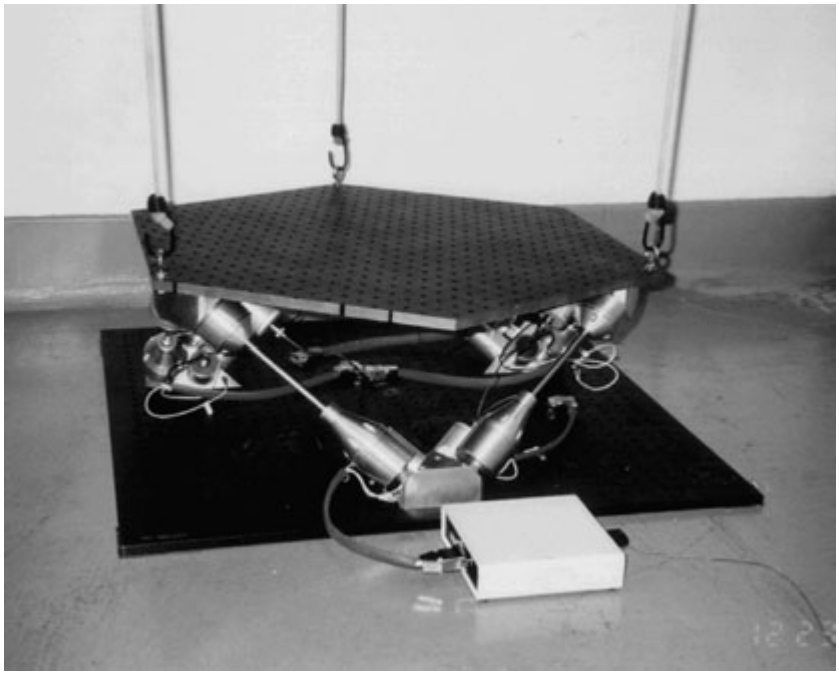

Figure 3.8: *Hood Technology and University of Washington Hexapod [19]*

Figure 3.9: *Legs of the Honeywell Hexapod [22]*

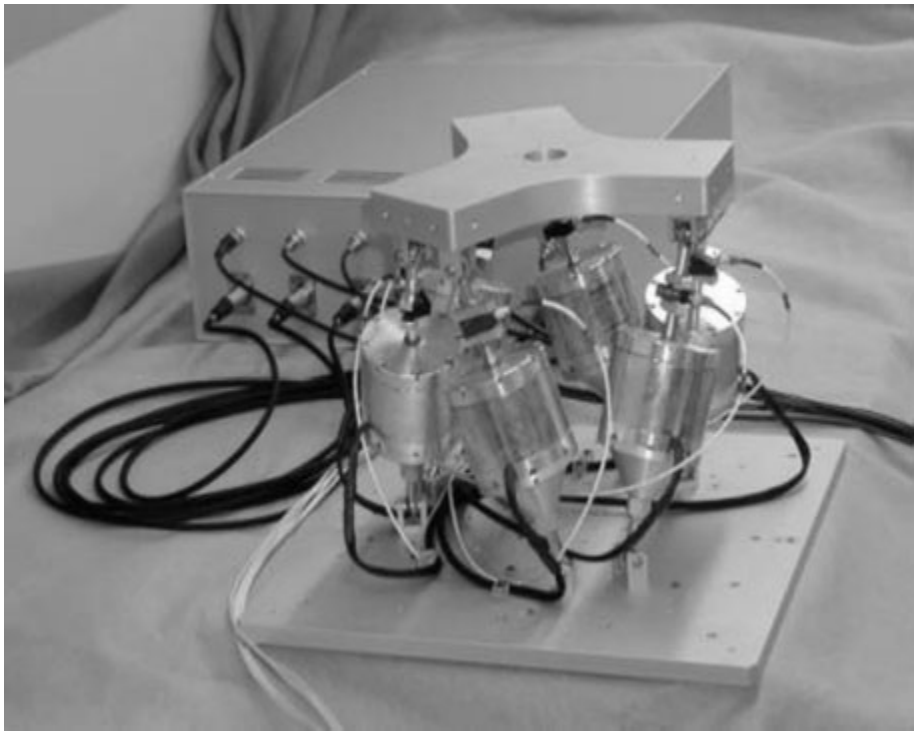

Figure 3.10: *Naval Postgraduate School Hexapod [23]*

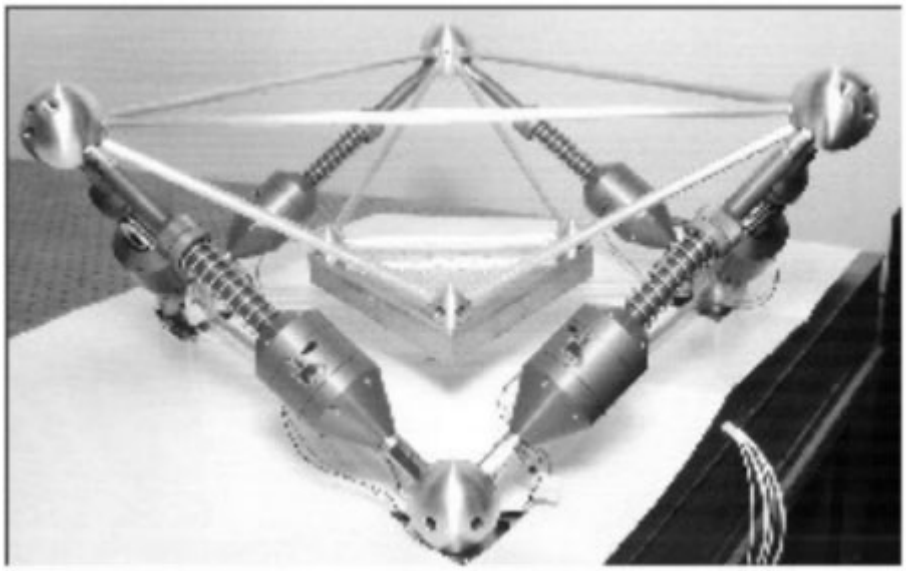

Figure 3.11: *University of Wyoming Hexapod [10]*

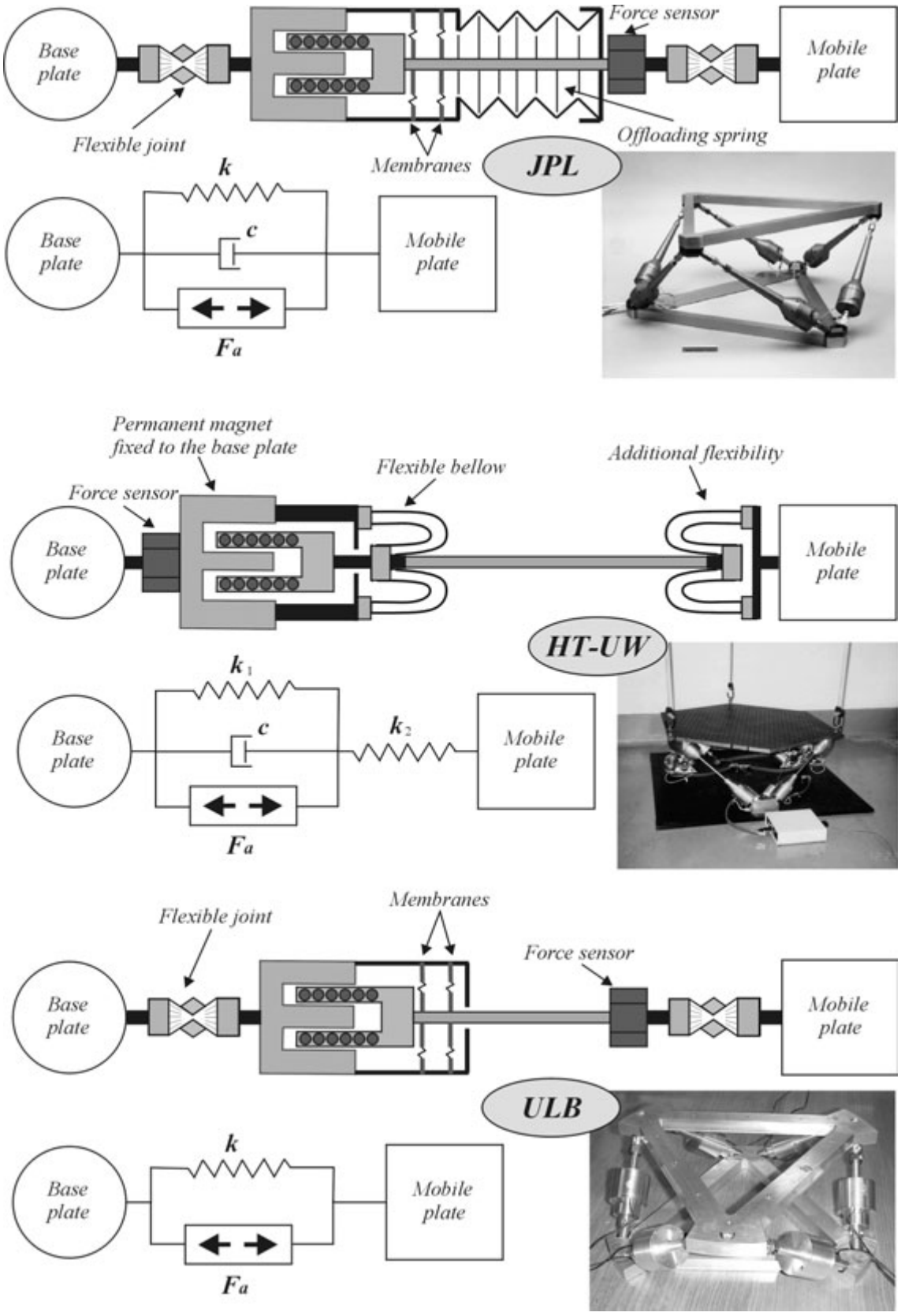

Figure 3.12: *Comparison between 3 different leg configurations; JPL, HT-UW and ULB*

3.6 ULB six-axis vibration isolator based on Stewart platform

3.6.1 Mechanical design of the ULB Stewart platform

The design of this soft Stewart platform is based on the cubic configuration discussed earlier. The two main plates here are two aluminium triangles connected to each other by means of six active struts. Each strut consists mainly of a voice coil actuator, a force sensor and two flexible joints as shown in Fig.3.13. Figure 3.14 shows the hexapod; where Fig.3.14(a) is a side view showing the inclination angles of the legs and Fig.3.14(b) is a general view showing the triangular plates and their connection to the legs [25, 26, 27, 28]. In the assembly of such a soft system, one should take into account many parameters; the design and manufacturing of the membranes, flexible joints and all the other parts should be handled carefully. Moreover, the wiring system and the cables connecting the actuators and sensors should be as soft as possible and passed carefully through the legs so as not to influence the flexibility of the leg [29, 30].

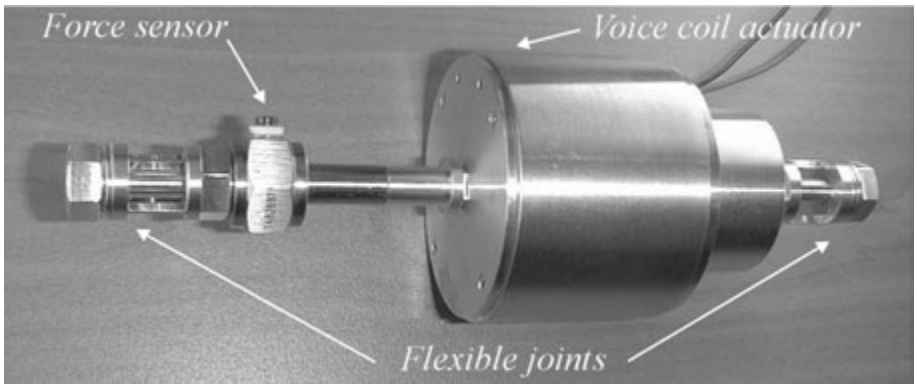

Figure 3.13: *Active strut of the soft hexapod (ULB design)*

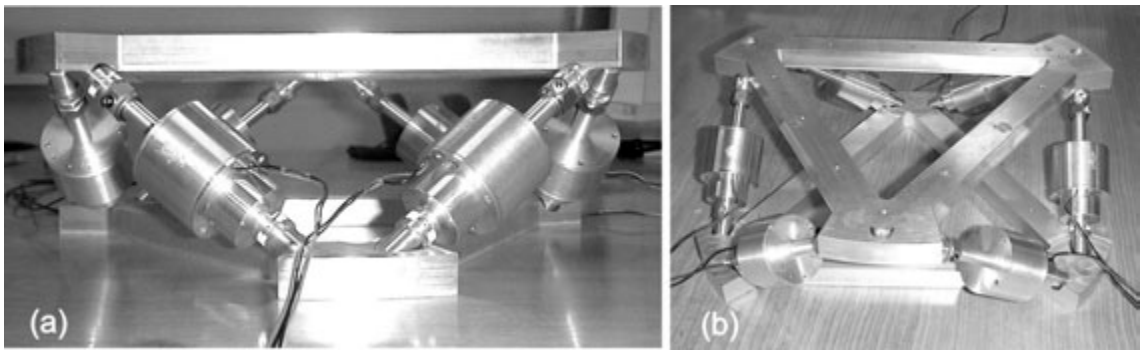

Figure 3.14: *Views of the soft hexapod (ULB design); (a): Side view, (b): General view*

3.6.2 Actuator design

Each of the voice coil actuators used here consists of a permanent magnet and a current carrying coil. The permanent magnet is a radial polarity toroid magnet with a ferromagnetic metal core manufactured by BEI KIMCO. The current carrying coil has been developed and manufactured in house, because classical metallic supports have a significant contribution to the damping through eddy-current. The eddy current adds passive damping to the system in the axial direction of the leg which leads to reduce the roll-off rate after the corner frequency. Figure 3.15 shows three different options for the design of the voice coil. When reviewing the previous designs, we found in [18, 31, 32] that the authors neglected the effect of this damping in the system in spite of its significant influence on the high frequency attenuation. The same problem of passive damping was mentioned in [23, 24] where it has been included in the representing model. On the contrary, in the Honeywell design [22] a carbon fiber composite material has been used to construct the coil holder (bobbin) in order to minimize the eddy current and reduce the passive damping. In our design, we could eliminate this problem completely by simply winding the coil and sticking the turns to each other using a special strong adhesive without having any holder from any kind. In terms of stability, this did not make any problem because the force exerted by the actuator does not exceed 15 Newtons and the adhesive proved higher strength. In order to hold the coil and the magnet up together, a set of components and connections are manufactured and installed as shown in the exploded view in Fig.3.16.

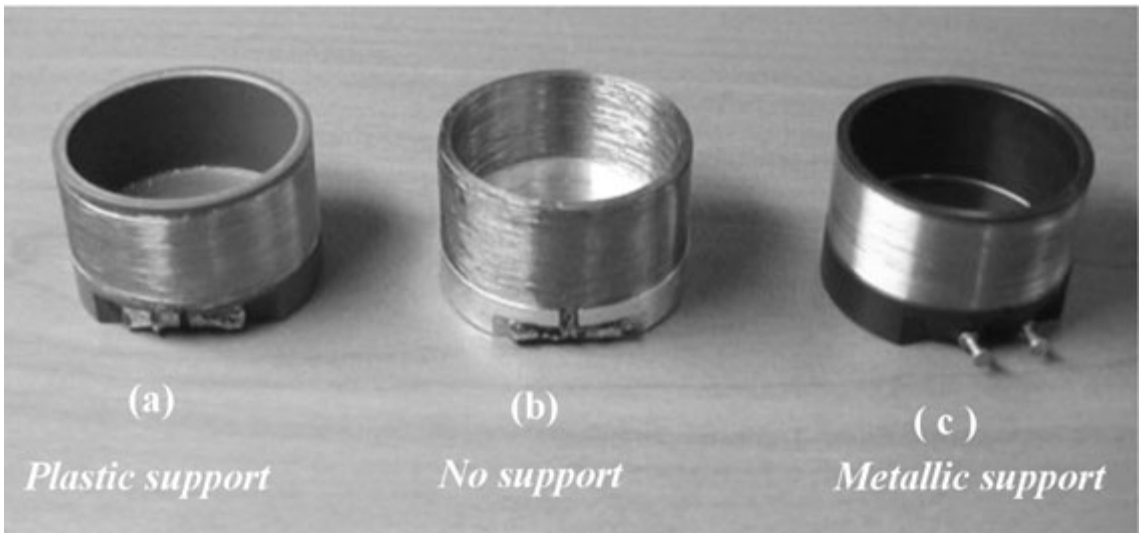

Figure 3.15: *Several design options of the voice-coils. Solution (b) is used in the ULB design*

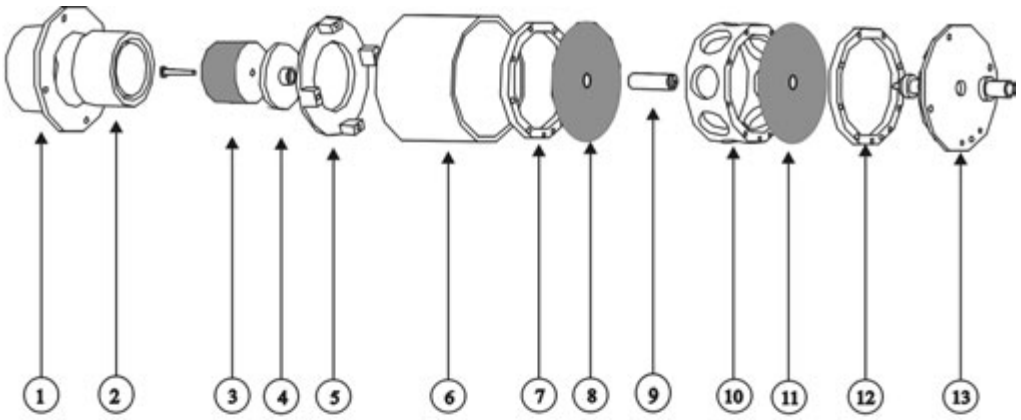

Voice coil actuator: *1- Magnet holder, 2-Magnet, 3-Coil, 4-Coil backplate, 5-Magnet-membrane spacer, 6-Envelope, 7-Spacer(1), 8-Membrane(1), 9-Central rod, 10-Membranes' spacer, 11-Membrane(2), 12-Spacer(2), 13-Cover.*

Flexible Joint

Membrane

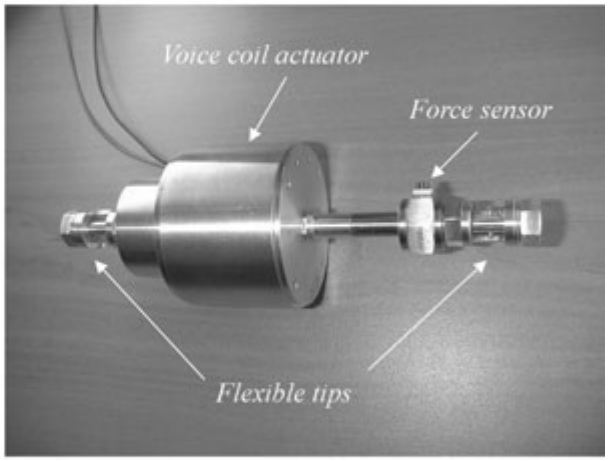

Coil and Permanent magnet

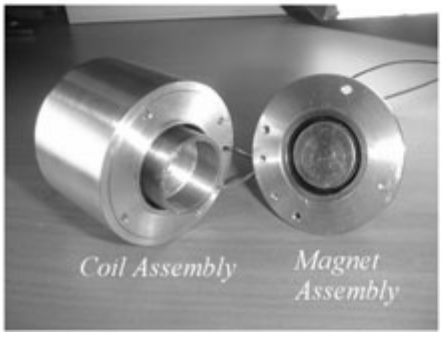

Figure 3.16: *The leg of the Stewart platform and its components; exploded view of the different parts of the actuator, a flexible tip, a membrane and the internal design of the actuator*

3.6.3 The flexible membranes

To allow the current holder bobbin to move freely through the air gap of the permanent magnet in the actuator, an alignment system is needed. The alignment system should be adapted to the requirements of the vibration isolation. It must, therefore, have the following characteristics:

- Low axial stiffness in the direction of the central axis of the actuator: the corner frequency of the whole system depends on the axial stiffness of the strut.
- High radial stiffness in the direction normal to the actuator axis: the lateral flexibility causes local modes in the leg that deteriorate the isolation authority at high frequency; this is why these modes must be pushed as high as possible.
- Minimum friction and backlash.
- High repeatability and long life time: the actuator works in a vibrating mode with different frequencies. This demands from the guiding to support this motion for millions of cycles.
- Nonmagnetic characteristics: to avoid the magnetic forces due to the attraction of the permanent magnet.

To achieve most of the previous requirements, two flexible membranes are manufactured and installed as a guiding system. Beryllium Copper is selected to be the material of these membranes because of its high yield strength and nonmagnetic behaviour, besides its ability to relieve residual stresses that act like a prestressed composite when exposed to mechanical processes. There are many shapes and designs of membranes found in the literature as shown in Fig.3.17 [33]. In Fig.3.18 we show several design shapes of the membranes that have been manufactured and tested at the ASL. Figure 3.18(c) represents a design that proved to have the best compromise between large displacement and uniform stress distribution.
Figures 3.19 and 3.20 show the result of a static finite element simulation where a constant load is applied normally to the membrane. Figure 3.19 shows a map of the displacement travelled by each element of the membrane as seen in the *F.E.M* model and Fig.3.20 shows the stress distribution on the surface of the membrane. The objective of this simulation is to optimize the different parameters of the membrane so as to have the design with the highest possible displacement as well as the most uniform stress distribution on the membrane. It is worth mentioning here that the manufacturing process has a significant effect on the characteristics of the membrane. The mechanical metal removal processes can induce high residual stresses in the membrane causing deformations that appear as "click-clack" behaviour (elastic instability) which limits the stroke and the implementation. To avoid this problem, the process used here to produce the membranes is the photochemical machining process (*Etching*).

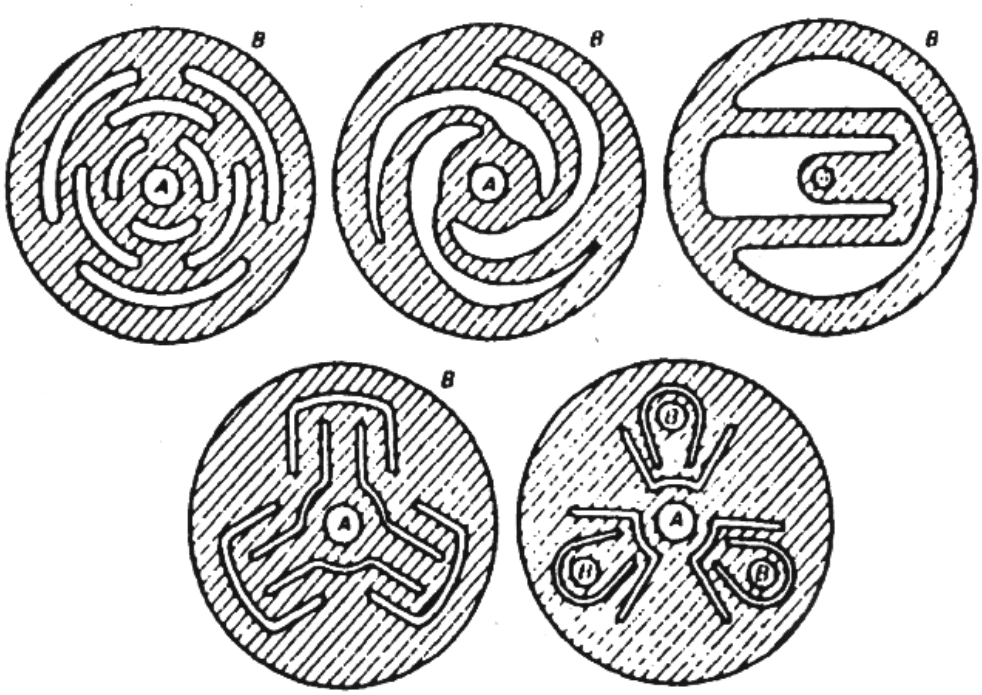

Figure 3.17: *Different shape designs of the membrane from the literature [33]*

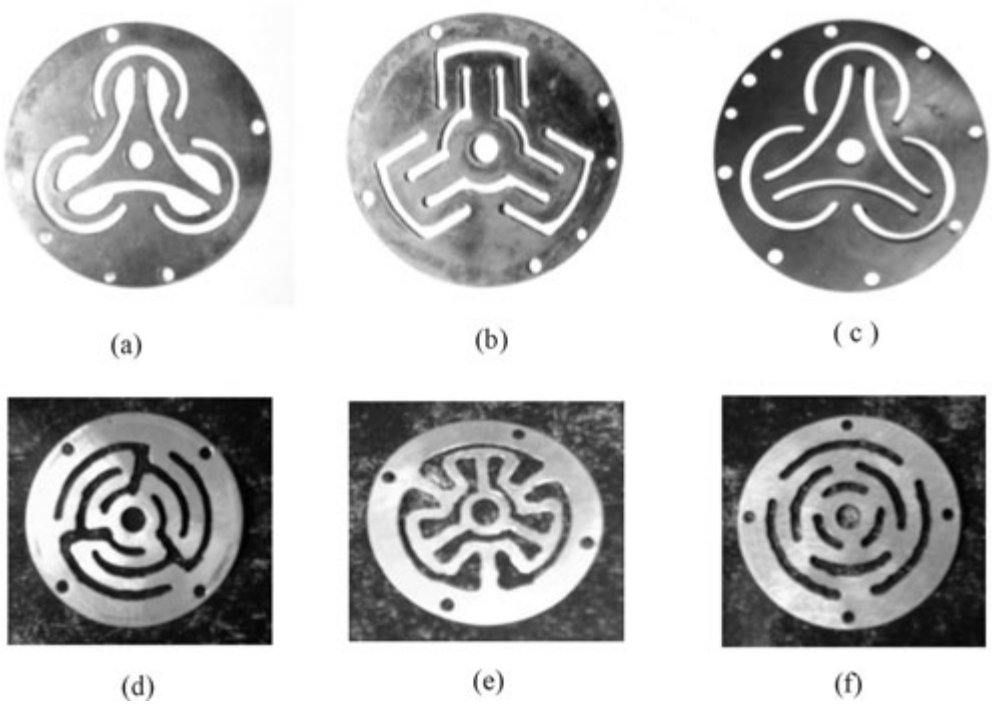

Figure 3.18: *several design shapes that have been designed and tested in the laboratory*

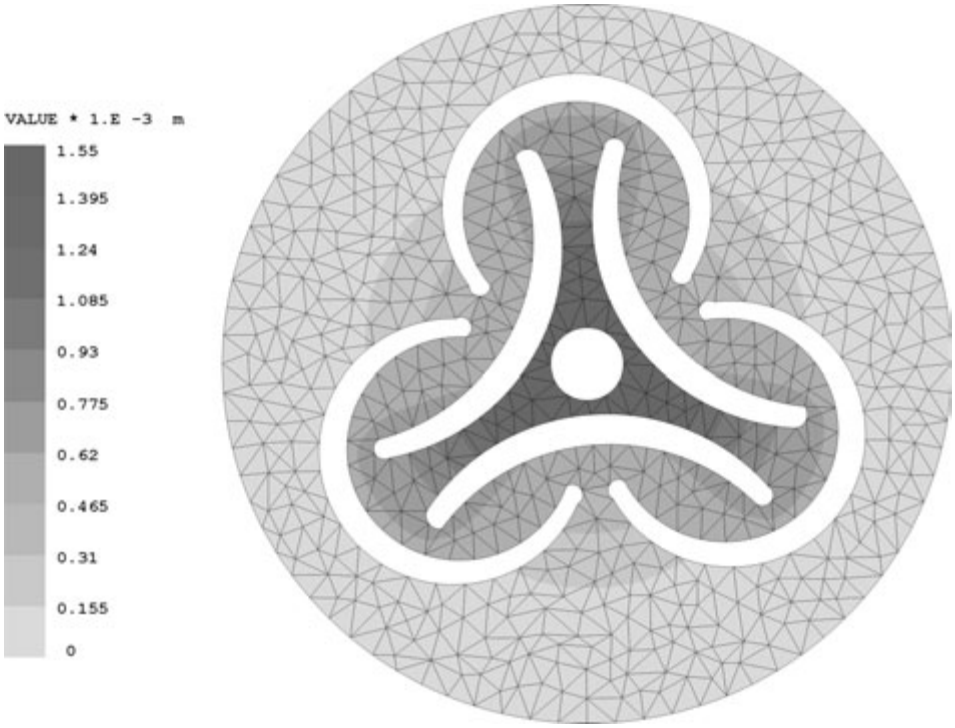

Figure 3.19: *FEM displacement distribution of the membrane*

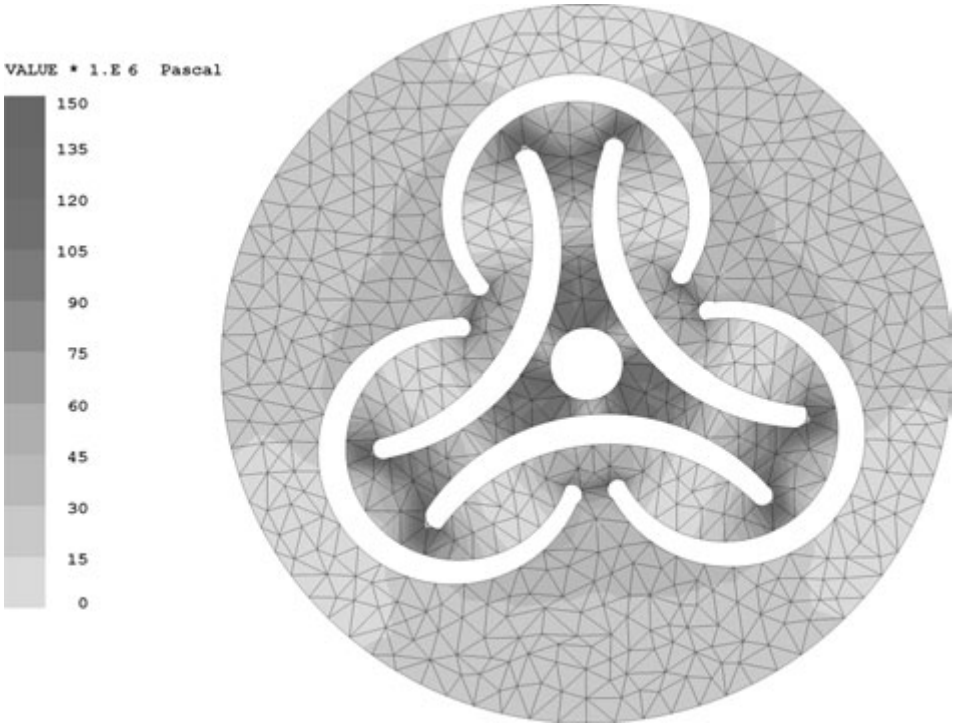

Figure 3.20: *FEM stress distribution of the membrane*

3.6.4 The flexible joints

To connect each leg to the support plates, some kind of spherical joint is needed. It is avoided to use classical joints because they have a significant amount of backlash and friction which is undesirable in precision engineering. Instead, flexible joints are used, which eliminate the backlash and friction, at the expense of some additional parasitic stiffness. The influence of the joints has been discussed by previous authors [11, 13, 19, 24]. The new ULB design of flexible joints has been based on having the following characteristics:

- High axial stiffness: to pass the control force faithfully from the actuator to the mobile plate.
- Low bending and torsion stiffness: to increase the authority of the active control as will be discussed later. It turns out that this rotary stiffness of the flexible joints will actually determine the zeros of the system.
- High shear stiffness: to push the local modes of the legs as high as possible. These modes can reduce the isolation performance at high frequency if left close to the corner frequency.
- Minimum friction and backlash.

To fulfil these requirements, several designs of flexible joints have been considered; they are shown in Fig.3.21. In Fig.3.21(a) and(c), the joint has a high stiffness in axial direction and low stiffness in the two bending degrees of freedom but the problem here is that the bending ribs are thin and long and this softens the shear and torsion degrees of freedom which is not desirable in the design. Figure 3.21(b) shows a new improved design of the joints where bending flexibility here is caused by the rotation of the torsion rods which have been made out of carbon fiber. It is based on a universal joint rather than a spherical joint. This design of the flexible joint has been selected and manufactured for the current design of the ULB Stewart platform. Figure 3.21(e) presents a commercial flexible tip with a relatively high bending stiffness [34]. Figure 3.21(f) shows a classical coupling with a low axial, bending and shear stiffness. The flexible joints shown in Fig.3.21(a),(b),(c) and (e) behave like universal joints with minimum friction and backlash.

3.7 Dynamic modelling of an ideal Stewart platform

The dynamic modelling of ideal Stewart platforms has been discussed in [5, 18, 35]. The hexapod based on the cubic architecture is interesting because it provides orthogonality and symmetry in all the directions. The stiffness and the control capability is uniform here and the coupling between the actuators is minimized. Following [18], Fig.3.22, depicts the orientation of the nodes and the struts of this architecture; the triangular base plate is formed by the connection of the nodes 1, 3 and 5; while the payload plate is formed by the nodes 2, 4 and 6. The struts are the edges of the cube formed by connecting the nodes of the base plate and the payload plate. The base plate reference frame $\{x_b, y_b, z_b\}$ has its origin at node 0 and the payload reference frame $\{x_r, y_r, z_r\}$ has its origin at the geometric

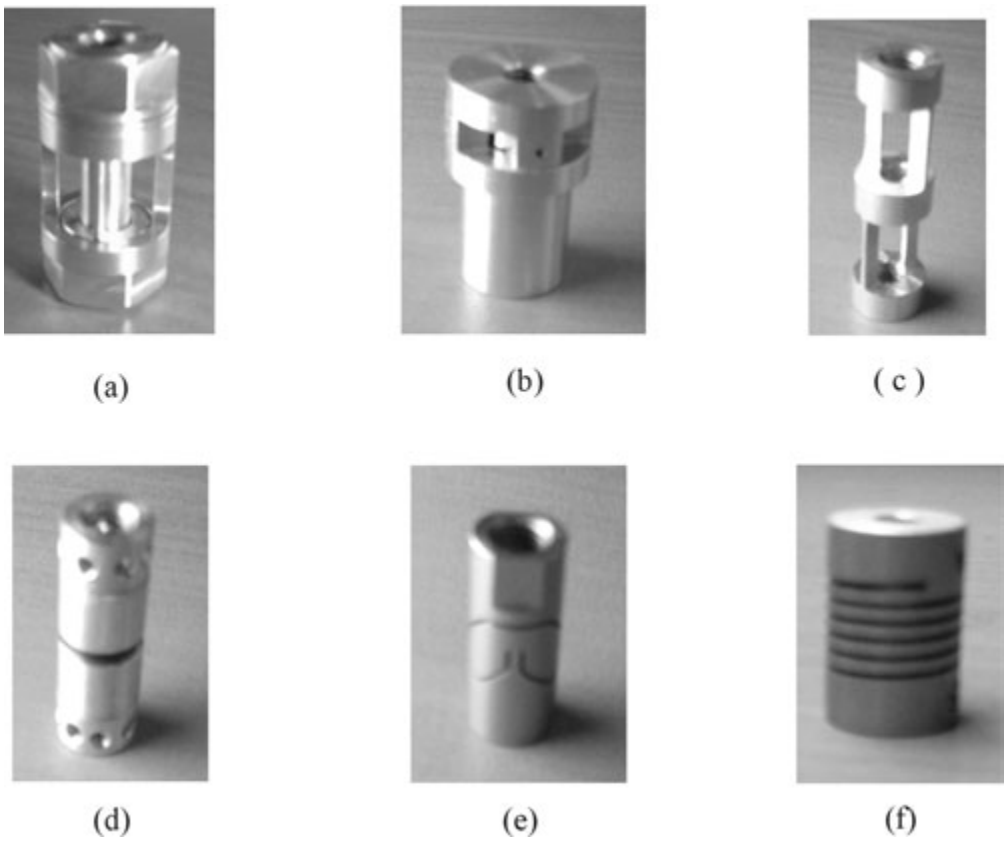

Figure 3.21: *Several designs of flexible joints*

center of the hexapod, node 8 (center of the cube). Assume that the base plate is fixed and the payload plate is a mobile axisymmetric rigid body with a mass m and a principal inertia axes aligned with $\{x_r, y_r, z_r\}$, the principal moments of inertia $I_x = I_y = mR_x^2$, $I_z = mR_z^2$, and with a center of mass located at an offset distance Z_c from the center, along the vertical axis z_r. Another assumption is that the struts are rigid and the bending stiffness of the flexible joints is neglected. The dynamic second order differential equation of motion of the isolator is:

$$M\ddot{x} + Kx = Bf \tag{3.12}$$

Where, $x = (x_r, y_r, z_r, \theta_x, \theta_y, \theta_z)^T$ is the vector describing the small displacements and rotations in the frame $\{x_r, y_r, z_r\}$, $f = (f_1, f_2, ..., f_6)^T$ is the active control force vector in strut 1 to 6 respectively, K and M are the stiffness and mass matrices of the isolator and B is the force Jacobian matrix which allows to express the active control forces in the payload reference frame (Appendix A).

To establish the equation of motion and evaluate the eigenvalues of the cubic Stewart platform [18], consider the estimation of the kinetic energy T of the mobile platform expressed in the frame $\{x_r, y_r, z_r\}$.

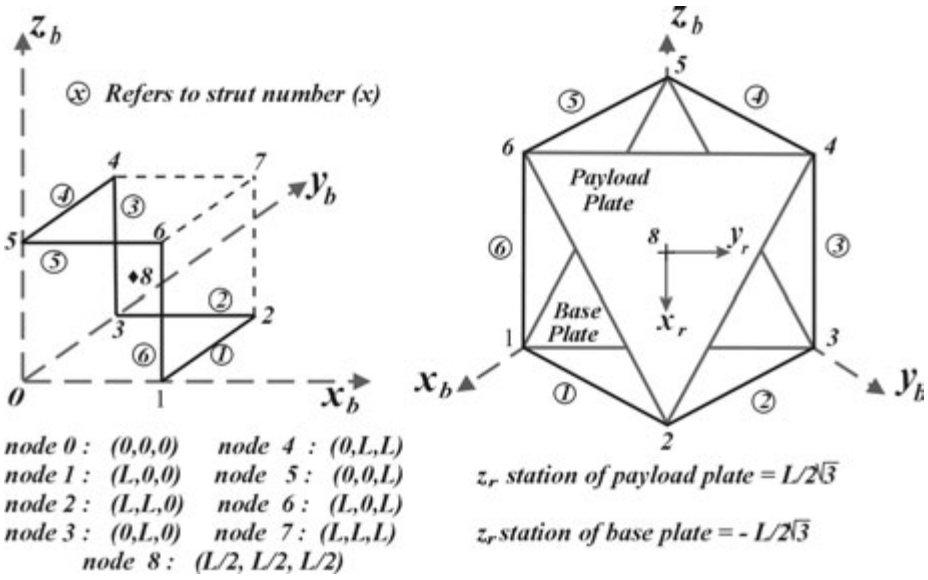

Figure 3.22: *Geometry and coordinate systems for the cubic hexapod isolator*

$$T = \frac{1}{2}mv^2 + \frac{1}{2}\omega^T I\omega \tag{3.13}$$

where m is a 3×3 diagonal mass martix, v is the translational velocity vector of the center of mass of the mobile platform, I is the moment of inertia and ω is the angular velocity of the payload. Expressing v in the reference frame $\{x_r, y_r, z_r\}$, we get

$$v = \begin{pmatrix} \dot{x}_r + \dot{\theta}_y Z_c \\ \dot{y}_r - \dot{\theta}_x Z_c \\ \dot{z}_r \end{pmatrix}$$

where $\dot{\theta}_i$ is the rotation around direction i and Z_c is the distance in the z-direction between the reference frame and the center of mass of the mobile plate. Since the principal axes of inertia are aligned with $\{x_r, y_r, z_r\}$, the rotation part becomes:

$$\omega^T I\omega = I_x(\dot{\theta}_x)^2 + I_y(\dot{\theta}_y)^2 + I_z(\dot{\theta}_z)^2 \tag{3.14}$$

where $I_x = I_y = mR_x^2$ and $I_z = mR_z^2$. Here, R_x and R_z are the radii of gyration.
In a general form, the kinetic energy can be calculated from the equation

$$T = \frac{1}{2}\dot{x}^T M\dot{x} \tag{3.15}$$

where M is the global mass/inertia matrix and $x = (x_r, y_r, z_r, \theta_x, \theta_y, \theta_z)^T$ is the global translation and rotation vector. Equating Equ.(3.13) and Equ.(3.15) leads to the general mass matrix M

$$M = m \begin{pmatrix} 1 & 0 & 0 & 0 & Z_c & 0 \\ 0 & 1 & 0 & -Z_c & 0 & 0 \\ 0 & 0 & 1 & 0 & 0 & 0 \\ 0 & -Z_c & 0 & R_x^2 + Z_c^2 & 0 & 0 \\ Z_c & 0 & 0 & 0 & R_x^2 + Z_c^2 & 0 \\ 0 & 0 & 0 & 0 & 0 & R_z^2 \end{pmatrix} \tag{3.16}$$

The stiffness matrix K, resulting from the axial stiffness of the legs, can be calculated using the stiffness formula $[kBB^T]$ as shown in Appendix A, and is given by:

$$K = kBB^T = k \begin{pmatrix} 2 & 0 & 0 & 0 & 0 & 0 \\ 0 & 2 & 0 & 0 & 0 & 0 \\ 0 & 0 & 2 & 0 & 0 & 0 \\ 0 & 0 & 0 & 0.5L^2 & 0 & 0 \\ 0 & 0 & 0 & 0 & 0.5L^2 & 0 \\ 0 & 0 & 0 & 0 & 0 & 2L^2 \end{pmatrix} \tag{3.17}$$

Where, L is the length of each leg, which are identical, k is the axial stiffness and the force Jacobian B is given by the following formula:

$$B = \frac{1}{\sqrt{6}} \begin{pmatrix} 1 & 1 & -2 & 1 & 1 & -2 \\ \sqrt{3} & -\sqrt{3} & 0 & \sqrt{3} & -\sqrt{3} & 0 \\ \sqrt{2} & \sqrt{2} & \sqrt{2} & \sqrt{2} & \sqrt{2} & \sqrt{2} \\ -L/2 & L/2 & L & L/2 & -L/2 & -L \\ -L\sqrt{3}/2 & -L\sqrt{3}/2 & 0 & L\sqrt{3}/2 & L\sqrt{3}/2 & 0 \\ L\sqrt{2} & -L\sqrt{2} & L\sqrt{2} & -L\sqrt{2} & L\sqrt{2} & -L\sqrt{2} \end{pmatrix} \tag{3.18}$$

The eigenvalues are found from Equ.(3.12), where the mass matrix M, the stiffness matrix K and the Jacobian B are given by Equ.(3.16) to (3.18). This leads to the characteristic equation

$$M\ddot{x} + Kx = 0 \tag{3.19}$$

or, in Laplace form

$$(Ms^2 + K)x = 0 \tag{3.20}$$

Solving this matrix equation for nontrivial solutions, the natural frequencies of the system are obtained; the translation in the z direction (bounce mode) and the rotation around the z direction (torsional mode) are decoupled and given by:

$$\Omega_3 = \sqrt{2}\Omega_o \qquad\qquad \Omega_6 = \frac{\sqrt{2}}{\rho_z}\Omega_o \tag{3.21}$$

Where $\Omega_o = \sqrt{k/m}$ and $\rho_z = R_z/L$ is the z-axis radius of gyration normalized to the length of the leg. For most cases of interest $\rho_z < 1$ and $\Omega_6 > \Omega_3$. The remaining four modes are lateral bending and shear. Their natural frequencies occur in two identical pairs and are given by the roots of the equation:

$$(2 - \frac{\Omega^2}{\Omega_o^2})(\frac{1}{2} - \rho_x^2 \frac{\Omega^2}{\Omega_o^2}) - 2\rho_c^2 \frac{\Omega^2}{\Omega_o^2} = 0 \tag{3.22}$$

Where $\rho_x = R_x/L$ is the x-axis radius of gyration normalized to the leg length and $\rho_c = Z_c/L$ is the mass center offset normalized by the leg length. Note that if the center of mass is at the geometric center ($\rho_c = 0$) and if $\rho_x = 1/2$ and $\rho_z = 1$, the hexapod will have 6 identical natural frequencies, all equal to Ω_3.

3.8 Closed-loop behaviour of the ideal Stewart platform

Assume that M is the inertia matrix of the Stewart platform, K is the stiffness matrix and the vector F represents the forces and moments acting on the payload platform in a coordinate system consistent with x. The governing equation of motion for this hexapod in the Laplace transform is:

$$Ms^2x + Kx = F \tag{3.23}$$

A force sensor is located in each leg of the hexapod and collocated with the actuator of that leg, then the output equation becomes:

$$y = -kq + f \tag{3.24}$$

Where $y = (y_1, ..., y_6)^T$ is the 6 force sensor outputs, q is the vector of leg extension from the equilibrium position, k is the strut stiffness and $f = (f_1, ..., f_6)^T$ is the active control forces produced by the six actuators respectively, here $F = Bf$. We know that the relationship between the leg extension and the payload frame displacement can be expressed as $q = Jx = B^Tx$ where J and B are, respectively, the velocity and force Jacobian matrices shown in Appendix A and discussed in [10], we have

$$y = -kB^Tx + f \tag{3.25}$$

Using the decentralized integral feedback with constant gain g, the control law is:

$$f = -\frac{g}{s}y \tag{3.26}$$

Including equations (3.25) and (3.26), the closed-loop equation of motion becomes:

$$Ms^2x + Kx = \frac{g}{s+g}kBB^Tx \tag{3.27}$$

But we know that $K = kBB^T$, then

$$[Ms^2 + K\frac{s}{s+g}]x = 0 \tag{3.28}$$

Transforming the former equation into modal coordinates by , $x = \Phi z$, and taking into account the orthogonality relationships $\Phi^T M\Phi = diag(\mu_i)$ and $\Phi^T K\Phi = diag(\mu_i\omega_i^2)$, the characteristic equation becomes:

$$(s^2 + \Omega_i^2 \frac{s}{s+g}) z_i = 0 \tag{3.29}$$

Therefore, in closed-loop, every mode is the solution of the characteristic equation:

$$s^2 + \Omega_i^2 \frac{s}{s+g} = 0 \tag{3.30}$$

or

$$1 + g \frac{s}{s^2 + \Omega_i^2} = 0 \tag{3.31}$$

The corresponding root locus is shown in Fig.3.23. Unless the 6 natural frequencies are identical, a given value of gain g will lead to different pole locations for the various modes and it will not be possible to achieve the same damping for all modes [18, 36]. This is why it is recommended to locate the payload in such a way that the spread of the modal frequencies is minimized.

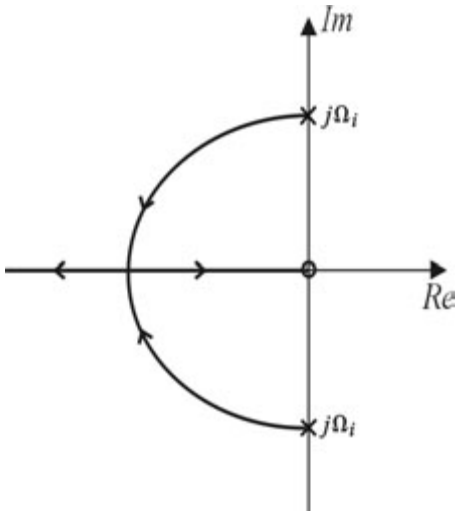

Figure 3.23: *Root locus of the modes of the six-axis isolator with integral force feedback*

3.9 Effect of the flexible joints

In the previous set of equations we assumed having no structural damping in the system. Another assumption was that all the stiffness is due to the axial stiffness of the actuators ($K = kBB^T$). However, in the real system the spherical joints are replaced by flexible joints to connect the active struts to the base plates of the Stewart platform. These flexible joints have high axial stiffness and low bending stiffness. Thus, the stiffness matrix has an additional contribution , K_e, according to the elasticity of the joints;

$$K = kBB^T + K_e \tag{3.32}$$

and the closed-loop equation becomes

$$[Ms^2 + K_e + kBB^T \frac{s}{s+g}]x = 0 \tag{3.33}$$

One can see that the asymptotic solution of Equ.(3.33) as $g \to \infty$ (transmission zeros) are no longer at the origin ($s = 0$), but they are the solution of the eigenvalue problem

$$[Ms^2 + K_e]x = 0 \tag{3.34}$$

If we denote them by ω_i, the closed-loop characteristic equation becomes

$$1 + g\frac{s^2 + \omega_i^2}{s(s^2 + \Omega_i^2)} = 0 \tag{3.35}$$

where the transmission zeros ω_i of the system are the asymptotic natural frequencies when the axial stiffness of the legs goes to zero and the only stiffness left in the leg is the bending and torsion stiffness of the joints. This important result shows that the transmission zeros are controlled by the flexible tips; The shift of the zeros away from the origin has a substantial influence on the practical performance of the Stewart platform as will be shown in the finite element model and the experimental results discussed below.

3.10 Finite element model of the actual Stewart platform

To predict the behaviour of the hexapod in a comprehensive way, a finite element model (FEM) has been built and simulated using SAMCEF finite element software. The finite element model is based on using the super element technique, retaining the most important degrees of freedom (DOF) of each component to reduce the total number of DOF of the system.

3.10.1 Structure of the finite element model

The flexible joints are modelled as zero-friction-zero-backlash joints where the motion is produced by the torsion of the carbon fiber rods (using the flexible joint shown in Fig.3.21(b)). Figure 3.24(a) shows a Computer Aided Design (CAD) view and the finite element model of the flexible joints; nodes 13 to 17 represent the main cross, the nodes 7 to 11 represent the upper yoke and the nodes 2 to 6 represent the lower yoke. The cross and the two yokes are modelled as aluminium beams. Four carbon fiber beams connect the yokes to the cross; the beams are shown in thick lines between (3-13), (6-14), (7-15) and (10-16). These carbon fiber beams are the places where the motion is tolerated in the flexible joint; the torsion of the rods (7-15) and (10-16) cause a rotation around the axis (15-16), similarly, the torsion of the two rods between (3-13) and (6-14) results in a rotational motion around the axis (13-14). The lines (2-1) and (11-12) are simple beams to connect the joint to the adjacent parts in the leg. The encircled nodes 1, 17 and 12 are the only retained degrees of freedom in this model to create the super element. The super element of the flexible joint has been created and used to construct the leg. The two super elements of the flexible joints in the model of the leg shown in Fig.3.24(c) are represented by the nodes (1,25,24) and (4,22,21).

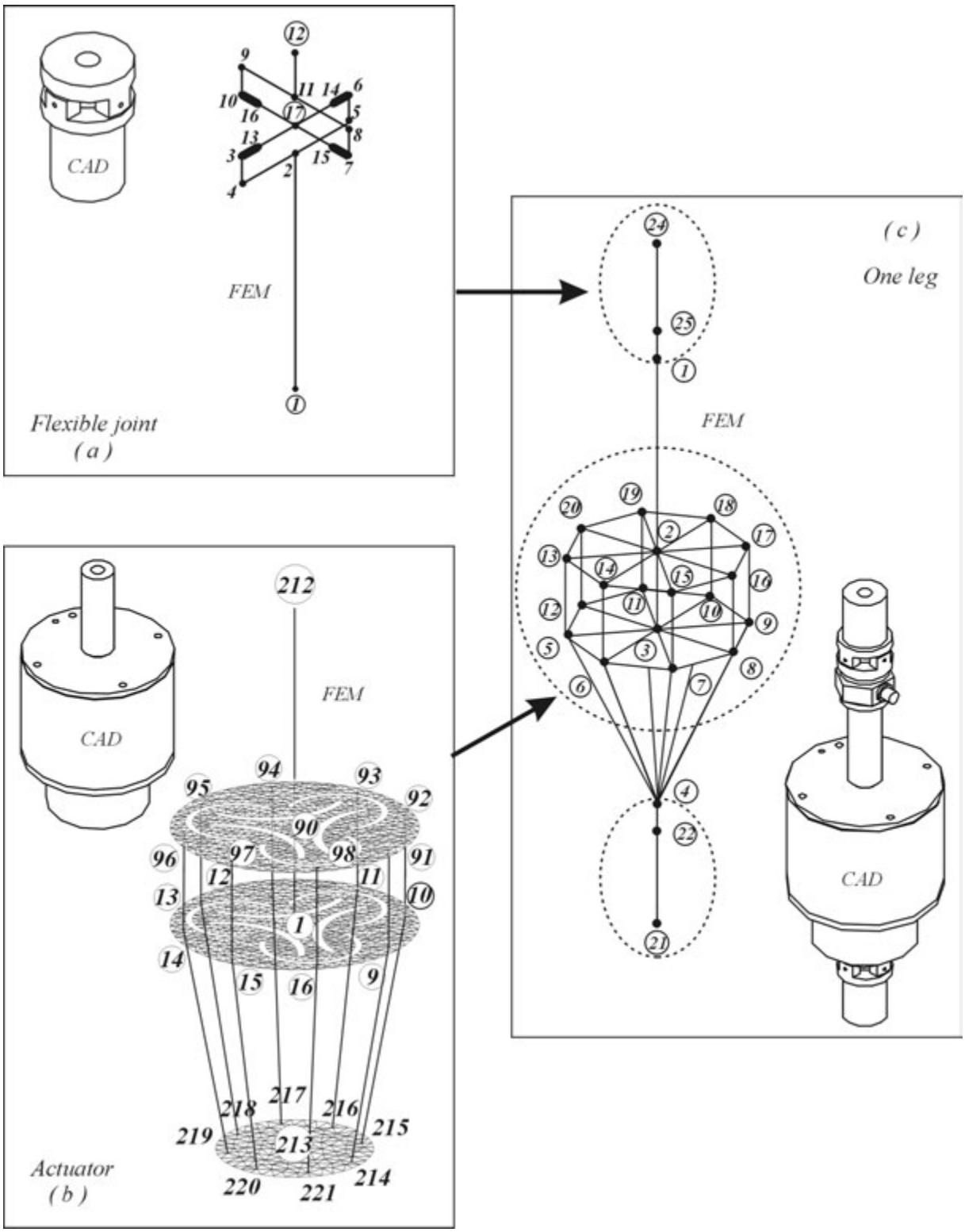

Figure 3.24: *Details of the finite element model of one leg of the hexapod showing the CAD model and the FEM model for the flexible joint, the actuator and the complete leg*

The actuator (Fig.3.24(b)) is modelled as two membranes connected to each other by 8 rigid beams at the circumference and a rigid beam in the center connecting between points 90 and 1. The upper membrane is formed by the points 91 to 98 and the lower membrane is formed by the points 9 to 16. The membrane assembly is connected to another plate in the bottom by rigid bodies. The lower plate formed by the points 214 to 221 represents the field assembly and the permanent magnet. A beam is installed between points 90 and 212 to connect the actuator to the upper flexible joint. The force sensor has not been taken into account because it was assumed as a rigid body with high stiffness. The lower flexible joint is connected to the actuator through point 213. To create a super element for the actuator, points (213,1,90,212), (9 to 16) and (91 to 98) have been retained. The created super element of the actuator is shown in Fig.3.24(c) between the nodes 1 and 4. Eventually, the model of the total leg of the Stewart platform is shown in Fig.3.24(c) between nodes 21 and 24, only the necessary nodes are retained to show the low frequency axial and lateral motions of the leg.
The joint model has been tested and saved as a super element, the same has been done for the model of the actuator, saving it as another super element. The super elements of two flexible tips and one actuator are combined producing a new super element that represents one full leg of the hexapod including all the compliance and inertia from the various components. The six legs are configured with respect to each other according to the requirements of the cubic architecture and the upper mobile plate of the hexapod is modelled and combined to the system. The lower plate is considered to be fixed to the ground, therefore, no representation of this plate appears in the model shown in Fig.3.25. The complete model of the Stewart platform with the upper plate and six legs (without using the super element technique) has 127000 DOF. This number of degrees of freedom has been reduced to 1722 DOF by using the super element technique.

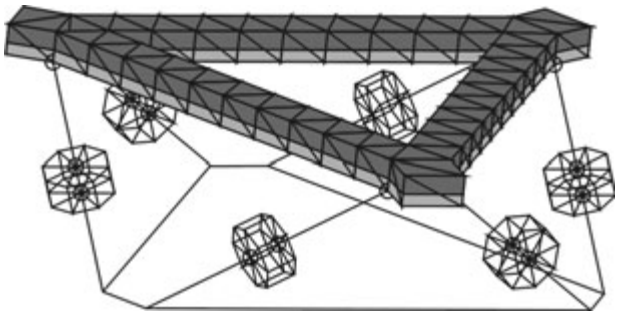

Figure 3.25: *Finite element model of the ULB hexapod*

The first six modes and mode shapes of the FEM are shown in Fig.3.26; the first piston (bounce) mode is at 2.9 Hz, the two tilt modes are at 3.2 Hz, the twist mode is at 6.5 Hz and, eventually, the two shear modes of the mobile plate are at 9.5 Hz. In addition to the six responsive modes in the frequency band 2.9-9.5 Hz, local modes of the legs appear in the frequency band 72-115 Hz. These later frequencies represent the local modes of

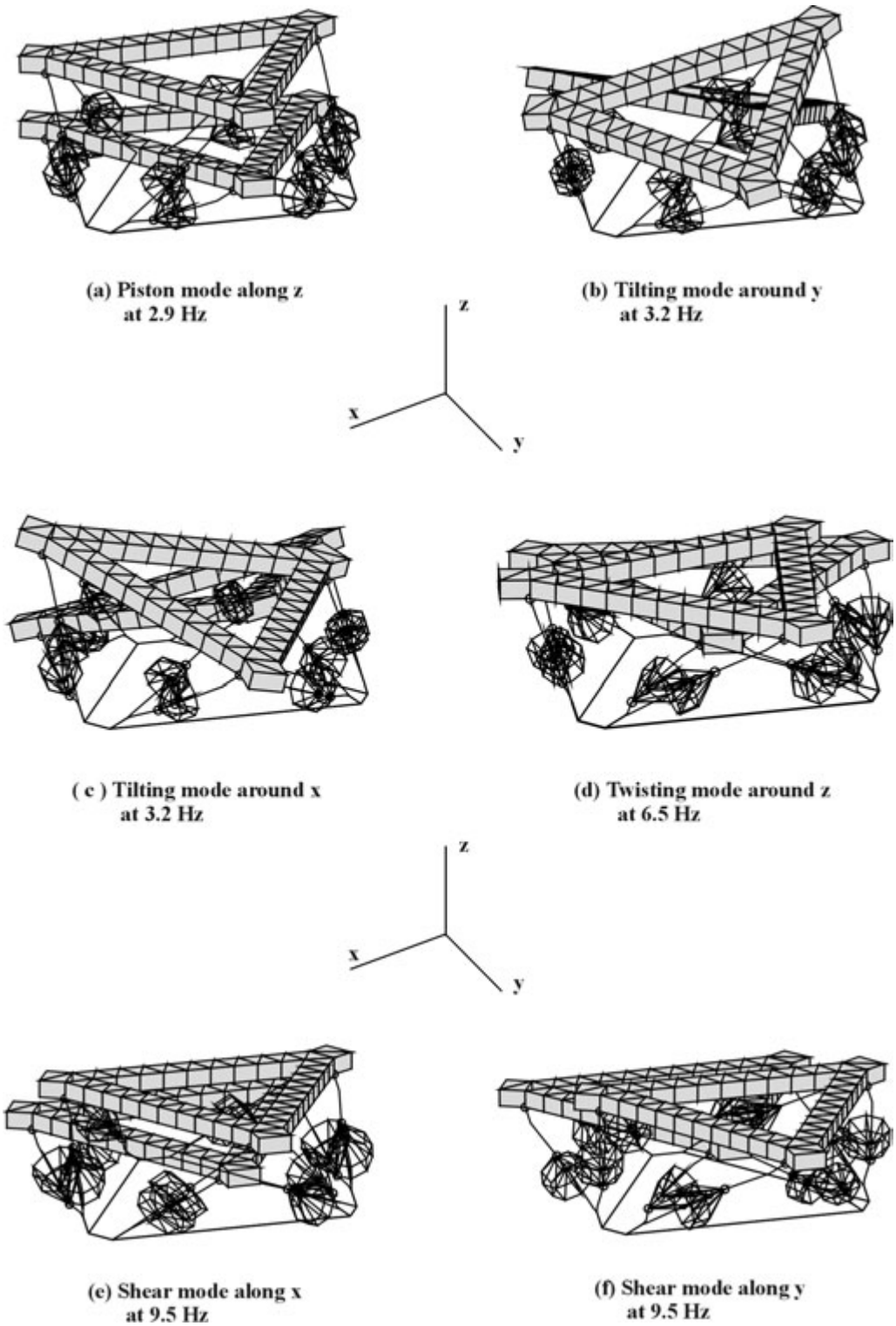

Figure 3.26: *Mode shapes of the first six modes as seen in the finite element model of the hexapod*

the legs due to the lateral flexibility of the membranes from one side and the shear and torsion flexibility of the flexible joints from the other side. The shapes of these modes vary between shear, torsion and a mixture the two shapes. Note here that using the super element model of Fig.3.24 will probably not produce a very accurate estimate of these local modes.
The local modes deteriorate the vibration isolation performance at high frequency by dominating the transmissibility of the system and reducing the roll-off after the corner frequency. The mass and stiffness distribution of the actuator play a great role in the frequency of these modes; the reduction of the mass of the actuator and/or approaching the lower hinging point of the leg (joint) to the center of mass of the actuator will increase the frequencies of these modes.

3.10.2 More on the flexible joints

This section extends the discussion of the influence of the flexible joints on the closed-loop performance of the six degrees of freedom isolator. Recall that the current design consists of a universal joint as shown in Fig.3.24(a); the cross is made of carbon fiber with circular cross-section. Using Equ.(3.35), the root locus of the closed-loop system with IFF is calculated and shown in Fig.3.27, where Ω_i are the open-loop natural frequencies and the open-loop zeros ω_i are the closed-loop natural frequencies of the system obtained by approaching the axial stiffness of the legs to zero. It is clear here that the joint stiffness results in a substantial reduction of the closed-loop performance, especially for the shear modes (modes 5 and 6).
To further illustrate the influence of the joint on the performance of the active isolator, Fig.3.28 shows the root locus corresponding to an alternative design in which the cross of the universal joint is now made of aluminium with a rectangular cross section (and $h \gg b$ so as to minimize the rotary stiffness). The results of Fig.3.28 have been obtained by finite elements; this design has not been manufactured.

3.11 Preliminary ground test

Since this hexapod is intended for space applications, it is necessary to compensate for gravity during the ground tests. This is achieved by external suspension springs attached to the ceiling. However, the additional spring stiffness produces a shift in the corner frequency of the isolator.
Figure 3.29 shows the open-loop frequency response function (FRF) of one leg between the input signal to the actuator and the conditioned signal out of the force sensor (output of the charge amplifier). As expected, the low frequency behaviour of the open-loop FRF exhibits alternating poles and zeros; the low frequency rigid body modes of the suspension are between 3.5 and 8.5 Hz. A low frequency zero appears here at 3 Hz resulting from the stiffness of the flexible joints; the existence of this zero close to the modes reduces the performance of the active control. In the previous section we discussed extensively how to reduce the frequency of this zero and, thus, increase the control authority.
Another band of modes appears at high frequency around 1000 Hz; these modes represent

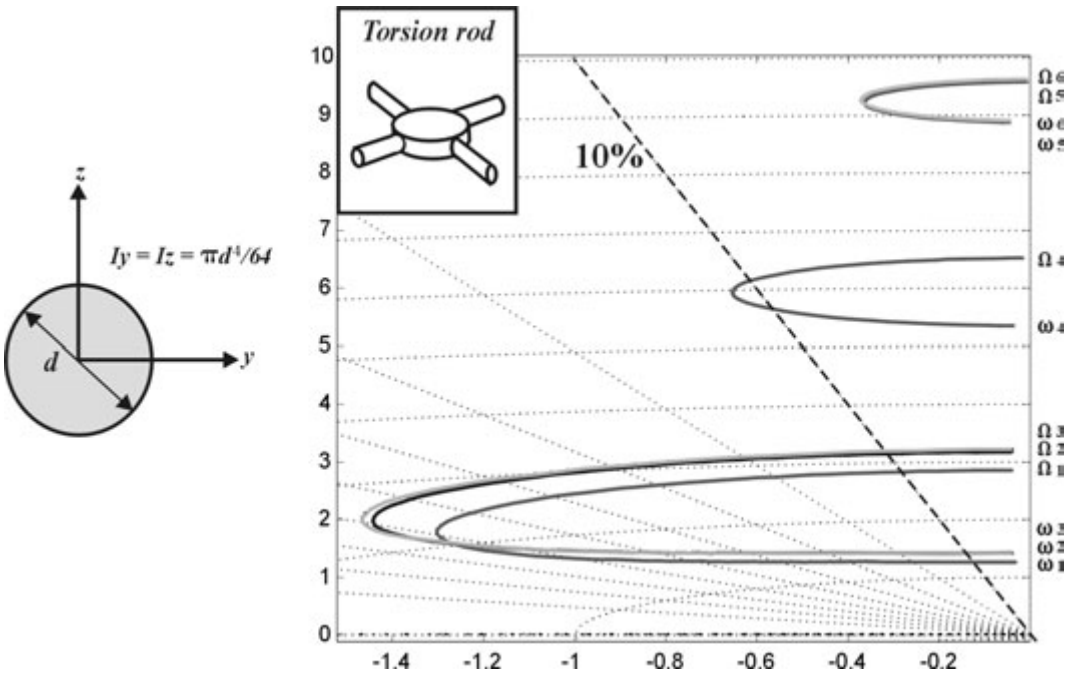

Figure 3.27: *Root locus of the first six modes with high bending stiffness of the joints (current design)*

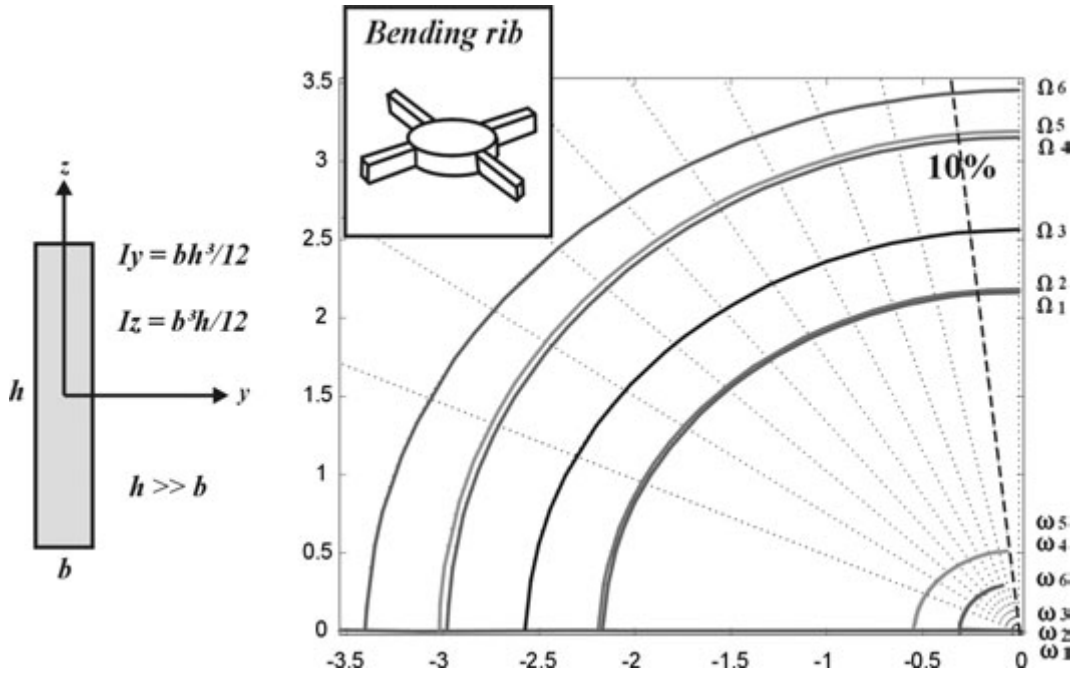

Figure 3.28: *Root locus of the first six modes with Low bending stiffness of the joints (modified design)*

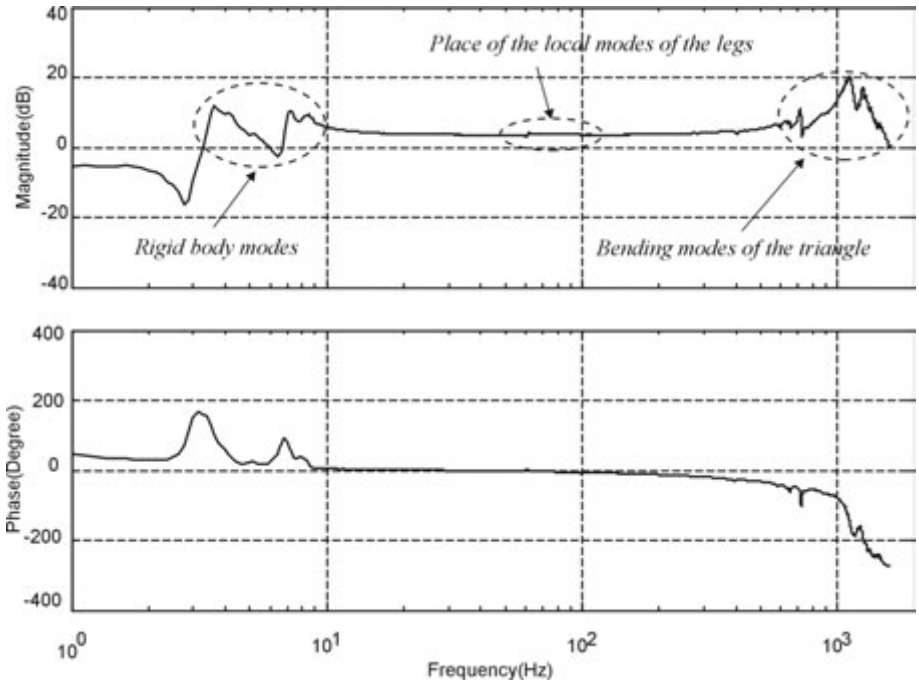

Figure 3.29: *Open-loop FRF measured in one of the legs between the signal to the actuator as an input and the signal out of the force sensor as an output*

the local modes of the mobile platform. The existence of these modes induces no effect on the system because they are located far enough from the corner frequency of the system (4.5 Hz) which results in isolating the disturbance of these modes. Besides, they are not physically relevant, because the payload should normally be attached to the payload plate. Note that the local modes of the legs (in the vicinity of 100 Hz) do not appear in the open-loop FRF of Fig.3.29, which shows that they are not observable/controllable; this is somewhat surprizing because if one leg cannot control nor observe its own local modes, it should normally control and observe those of the adjacent legs which are orthogonal. These local modes appear clearly in the transmissibility FRF of the isolator, as we discuss below.

Figure 3.31 shows the transmissibility function between the vertical acceleration (z-direction) of the lower plate and the acceleration of the upper plate in the same direction. This FRF is taken by exciting the system seismically with a random white noise signal that has a frequency range from 1 to 200 Hz. Looking at the open-loop curve of Fig.3.31, the transmission function is expected to attenuate at -40 dB/decade, ideally, because we make sure that there is no passive damping in parallel with the isolator. However, the roll-off of the FRF follows the expectations until approaching the local modes of the legs where the local dynamics become dominant. In the non-controlled (open-loop) configuration, the low frequency rigid body modes show overshoots with peaks higher than 0 dB. To reduce these overshoots while keeping the attenuation at high frequency, a decentralized force feedback active control strategy is applied. Six independent local single input single

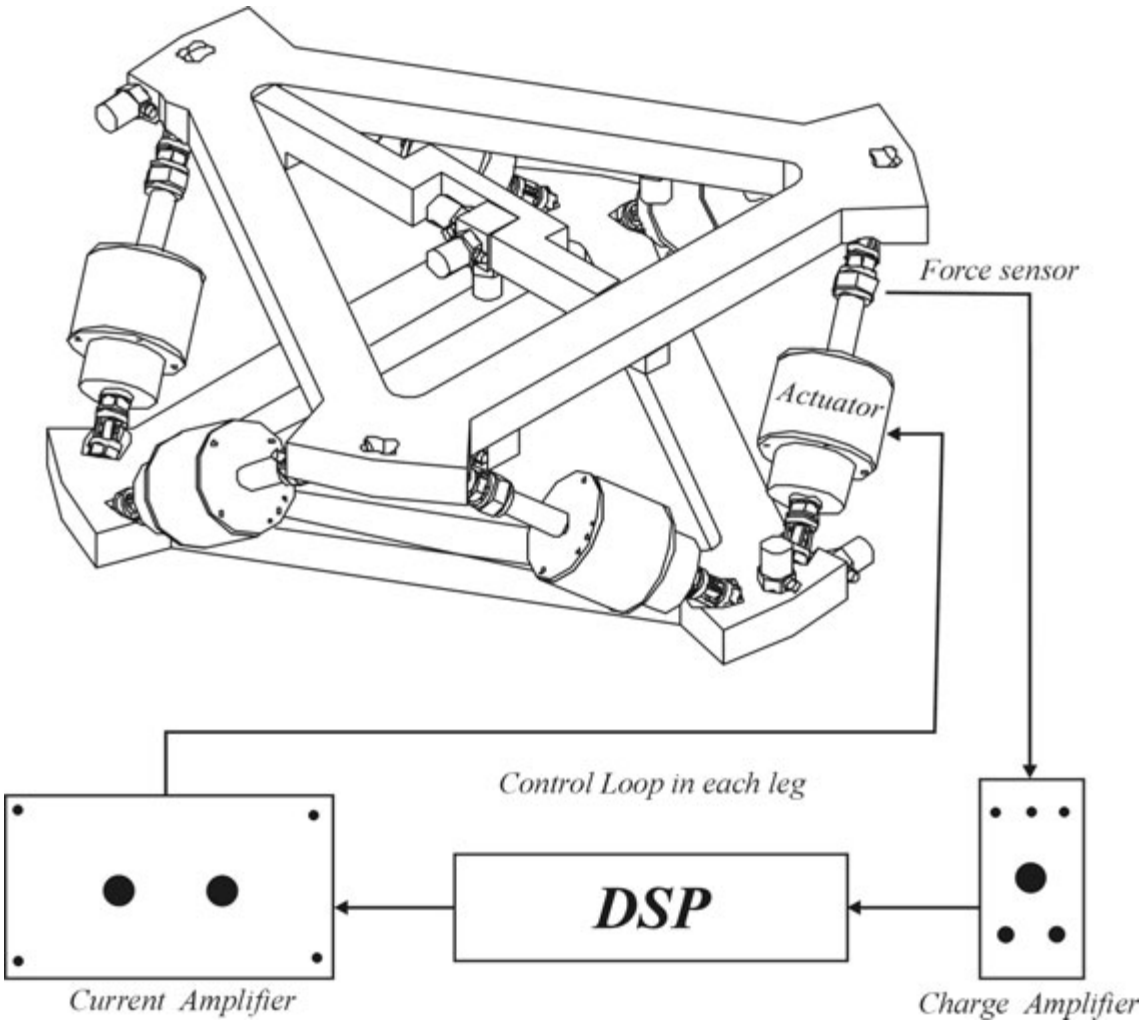

Figure 3.30: *SISO control loop in each leg of the hexapod*

output (SISO) control loops with equal gains are applied as explained in Fig.3.30. Two controllers have been tested in this ground test:

- Lag-Lead controller.
- Integral force feedback controller.

Figure 3.31 shows a typical transmissibility FRF with and without active control. One sees that the active control eliminates the overshoot of the rigid body modes while leaving the high frequency behaviour essentially unchanged. The influence of the local modes of the legs on the isolator performance near 100 Hz points out the importance of damping the transverse vibrations of the legs.

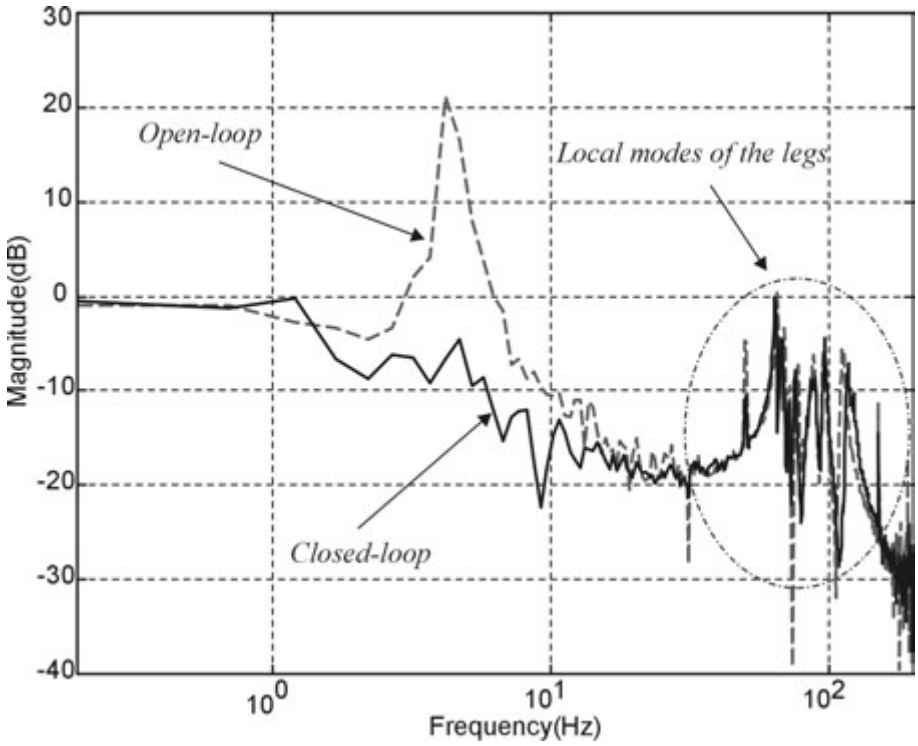

Figure 3.31: *Open and closed-loop transmissibility functions measured between the lower and upper plates (z-direction) in the ground test using Lag-Lead compensator.*

3.12 Micro-gravity parabolic flight test

3.12.1 Experiment objectives

The main difficulty faced in testing this isolation system on ground is the compensation of the static load due to gravity, any suspension system added here introduces a new stiffness that increases the corner frequency of the system, reducing the isolation performance and changing the characteristics of the system. Testing such a system in zero gravity (space station) is costly and needs exhausting work of preparations. Furthermore, because of the high competition on testing in the International Space Station (ISS), it has been decided to begin with a micro-gravity test. One way to test the system in micro gravity is the parabolic flight test. The advantages of testing in a parabolic flight is that the micro-gravity time is relatively long (22 seconds) and there is more space and possibility to stay with the experiment and to use the equipment one needs. This experiment has been carried out in the frame of:

The 33^{rd} *ESA parabolic flight campaign of A300 ZERO-G, in Bordeaux-Merignac, FRANCE.*

3.12.2 Experiment description

Stewart platform

The ULB six-axis isolator based on Stewart platform is equipped with six voice coil actuators and six force sensors in the six legs. For the purpose of performance measurement, six accelerometers are placed on the base plate and six other accelerometers on the upper mobile plate (Fig.3.37). The excitation signals propagating into the system are measured by the force sensors and fed back independently to the six actuators in the legs to suppress the vibrations near the rigid body principal modes. The performance is obtained in time and frequency domains (between the accelerometers of the lower and upper plates) using the data acquisition in the DSP card (Dspace 1103) conducted by a normal personal computer.
The Stewart platform has been installed on an excitation pad as shown in Fig.3.32. The excitation pad consists of two (50cm x 50cm) aluminium plates 5 mm thick separated by four springs. Two excitation shakers are installed on the pad; one of them is to excite the twisting and the two shear degrees of freedom and the other is to excite the piston and the two tilting degrees of freedom. The excitation shakers are driven by the DSP through two power amplifiers (Fig.3.33). A locking device is added to the system to connect the base plate and the payload plate, to avoid any damage of the system during the take-off and the landing phases of the parabolic flight.

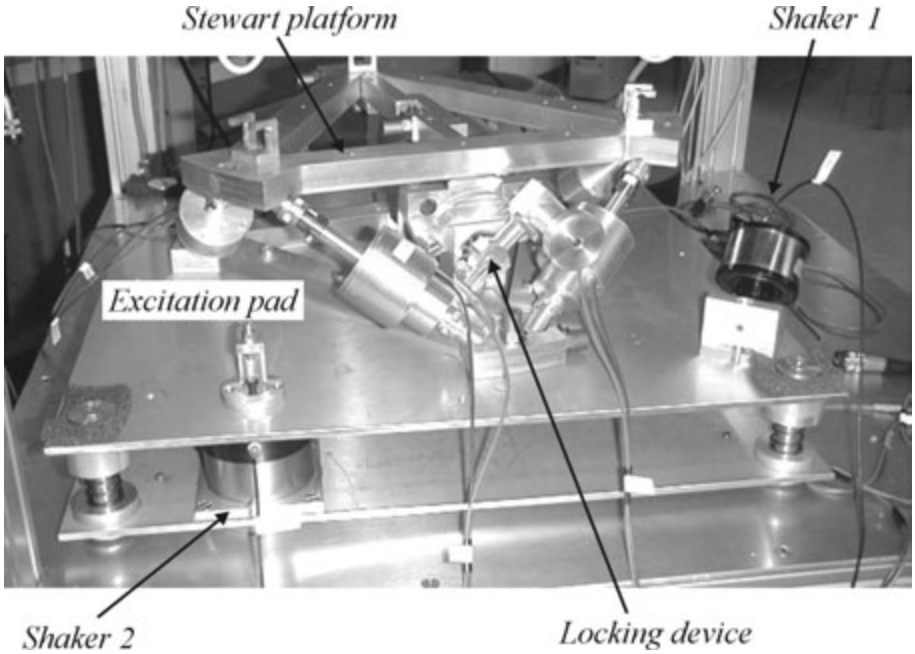

Figure 3.32: *Stewart platform mounted on top of the excitation pad*

Electronic devices

Two electronic boxes are used here: the control box and the acquisition box (Fig.3.34). All the electronics have been specially designed and built in the laboratory with the help

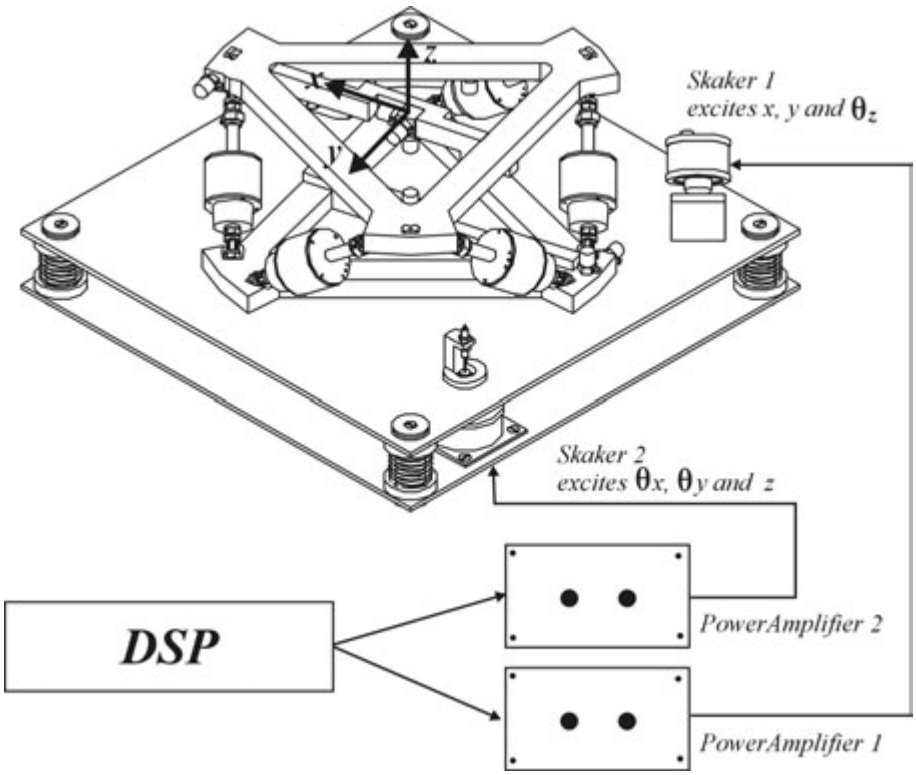

Figure 3.33: *Stewart platform mounted on top of the excitation pad and disturbance sources*

of the electronics team of Micromega Dynamics. The first electronic box (control box) contains six current amplifiers with 1.5A output to drive the voice coil actuators and two other current amplifiers with 0.75A to drive the two shakers. Seven (6 + 1 spare) charge amplifiers, to amplify the signals of the force sensors for control and acquisition purposes, are installed inside this box too. The second box (acquisition box) contains 13 (12 + 1 spare) charge amplifiers to amplify the signals of the accelerometers for performance calculation. One of the main problems we faced in these electronics was the offset; the amplification process caused an offset of 2-4 mV in the amplified signal. The influence of this offset has been found significant on the closed-loop results of the system as will be discussed later. A normal PC (200 MMX) with a Digital Signal Processing card DSP (Dspace 1103) installed on it and connected to an input/output box via cables. The hard disk of the PC has been installed in vertical position to resist the high accelerations.

The experiment rack

A mechanical frame with external dimensions (80×85×108 cm) has been built to hold the whole system (Fig.3.35(a)). The frame has been assembled out of (6×6 cm) hollow square aluminium tubes. The Stewart platform, the electronics and the computer has been installed and fixed to the frame as shown in Fig.3.35(b). The electronics and the PC computer were installed on the first level, the Stewart platform with the excitation pad on the second level and the display, keyboard and the mouse were installed on the

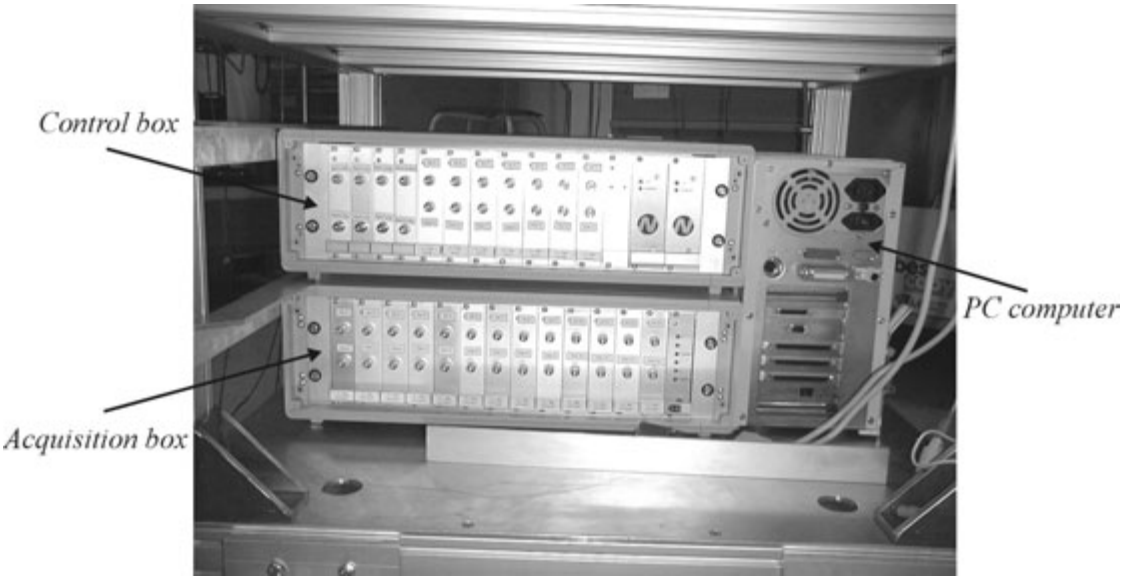

Figure 3.34: *The electronics boxes used in the flight test*

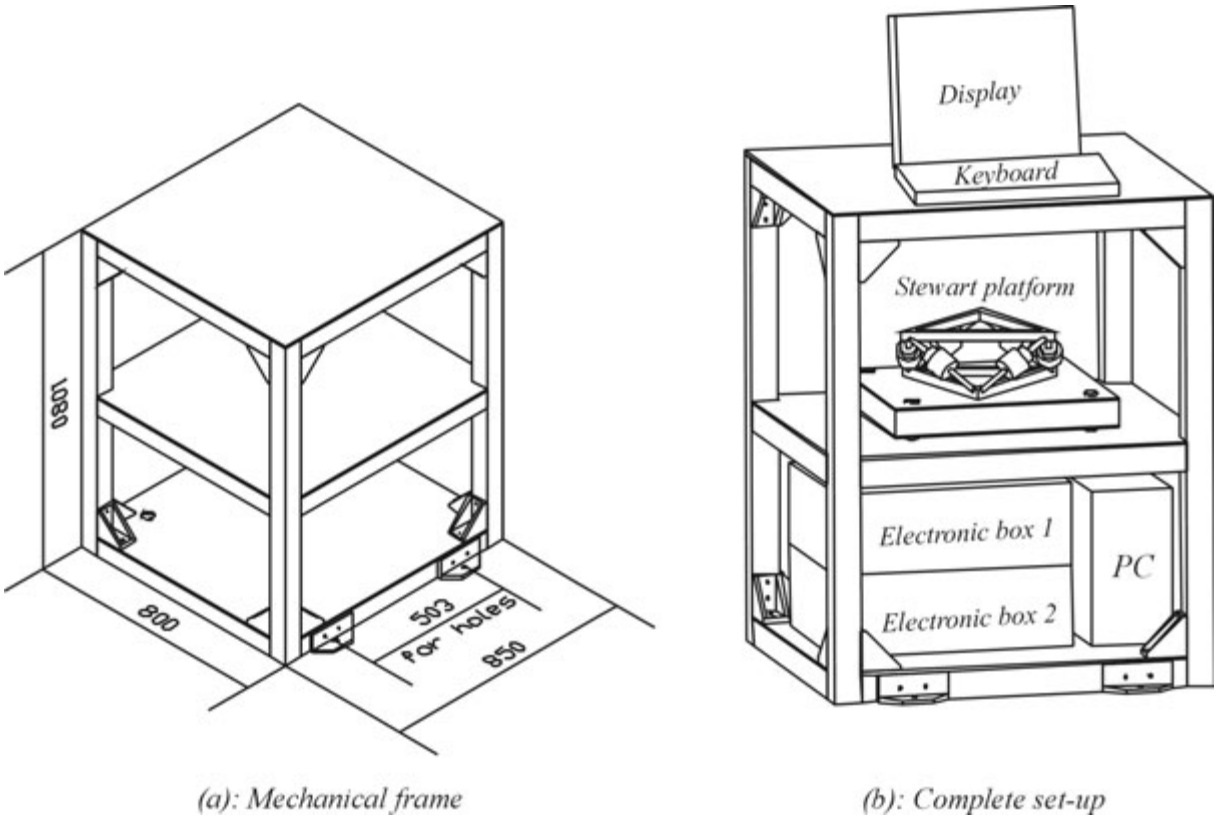

Figure 3.35: *(a): The mechanical frame, (b): The complete set-up installation of the experiment on the frame*

third level. In future tests, It is advised to install the keyboard in a lower level, because it is more comfortable for the experimenter to stay on the floor of the aircraft during the test. Figure 3.36 shows the actual picture of the experiment installed in the aircraft where all the external edges of the frame are covered by a protection foam to protect the experimenters from any shock during the micro gravity test.

Figure 3.36: *Photo of the experiment set-up installed in the aircraft*

3.12.3 In flight procedure

There was only one experimenter to fly with this experiment. Therefore, it was very important to prepare the experiment to be done easily and rapidly. The general tasks

executed by the experimenter are as follows:

1. After the take-off of the airplane and before the first parabola the computer is switched on, the accelerometers and the sensors are checked, the locking device is unlocked and the set-up is prepared for the experiment.

2. During each parabola, the control desk program is turned on, exciting the system and making the data acquisition automatically to be saved on the PC hard disk.

3. Between two parabolas the acquired data are saved and the accelerometers and force sensors are checked to be ready for the next parabola.

4. During all the parabolas, the accelerations, the forces and the input voltages to the current amplifiers are measured and registered in time domain.

5. After the last parabola, the locking device is locked again, the acquired data is collected, packed up and analysed and the test set-up is prepared for the next day.

Tasks of the first day (see Table 3.4)

1. The six voice coil actuators have been excited one at a time and the data is acquired to build the open-loop FRF in each leg between the voltage input to the current amplifiers and the force output from the collocated force sensor.

2. The two shakers are excited and the data from the twelve accelerometers is acquired to assess the open-loop transmissibility of the isolator between the lower and the upper plates.

3. Keeping the excitation on, a Lag-Lead controller has been applied and the control loops are closed in a decentralized manner. The signals of the twelve accelerometers are registered to assess the closed-loop transmissibility of the isolator between the lower and the upper plates.

Parabola	**Task**
1	Calibration of the program
2, 3, 12, 13, 22, 23	The two shakers are excited and the 12 acceleration signals are acquired in open-loop (without applying the control) to build the transmissibility FRF.
4, 5, 14, 15, 24, 25	The loop is closed with Lag-Lead compensator (gain=200) and the 12 acceleration signals are acquired in closed-loop (with applying the control) to bulid the transmissibility FRF.
6-11, 16-21, 26-31	The six actuators are excited one at a time and the force and voltage signals are acquired to build the FRFs in each leg between the actuator and the force sensor.

Table 3.4: *Program of tasks executed during the first day of the flight test*

Tasks of the second day (see table 3.5)

In the second day, the same procedure of the first day has been repeated but with changing the control strategy. A sky-hook (integral force feedback) control technique has been used here to compare the results of the two control strategies.

Parabola	Task
1	Calibration of the program
2, 3, 12, 13, 22, 23	The two shakers are excited and the 12 acceleration signals are acquired in open-loop (without applying the control) to build the transmissibility FRF.
4, 5, 14, 15, 24, 25	The loop is closed with Integral compensator (gain=60) and the 12 acceleration signals are acquired in closed-loop (with applying the control) to bulid the transmissibility FRF.
6-11, 16-21, 26-31	The six actuators are excited one at a time and the force and voltage signals are acquired to build the FRFs in each leg between the actuator and the force sensor.

Table 3.5: *Program of tasks executed during the second day of the flight test*

Tasks of the third day (see Table 3.6)

In the third day, it was foreseen to test the isolator with a payload (optical equipment) but because of the changes in the characteristics of the expected payload it was impossible to install the equipment on top of the isolator. This change led us to repeat the same experiment in the third day sharing the time between the two control techniques and varying the control gain taking three values of gain for each technique.

Parabola	Task
1	Calibration of the program
2, 3, 4, 14, 29, 30, 31	The two shakers are excited and the 12 acceleration signals are acquired in open-loop (without applying the control) to build the transmissibility FRF.
5-7 and 14-16	The loop is closed with Integral compensator (variable gain=40,50,60) and the 12 acceleration signals are acquired in closed-loop (with applying the control) to bulid the transmissibility FRF.
17-19 and 20-22	The loop is closed with Lag-Lead compensator (variable gain=100,150,200) and the 12 acceleration signals are acquired in closed-loop (with applying the control) to bulid the transmissibility FRF.
8-13 and 23-28	The six actuators are excited one at a time and the force and voltage signals are acquired to build the FRFs in each leg between the actuator and the force sensor.

Table 3.6: *Program of tasks executed during the third day of the flight test*

3.12.4 Performance assessment calculation

Six accelerometers have been installed on the lower plate of the Stewart platform and six other accelerometers on the upper plate as shown in Fig.3.37. The numbers $\{1, 2, 3, 4, 5, 6\}$ correspond to the accelerometers installed to measure the acceleration in the three translation directions x, y and z and the three rotations around these axes, respectively. The translations are measured directly while the rotations are calculated by subtracting the signals. For instance, to get the rotation around the x-axis, we subtract the signal of 3 from the signal of 4. Similarly, to calculate the rotation around the y-axis we subtract the signal of 3 from the signal of 5, and the rotation around z-axis is obtained by subtracting the signal of 2 from the signal of 6 and the values are normalized to the distance of the sensor from the reference frame $\{x, y, z\}$.

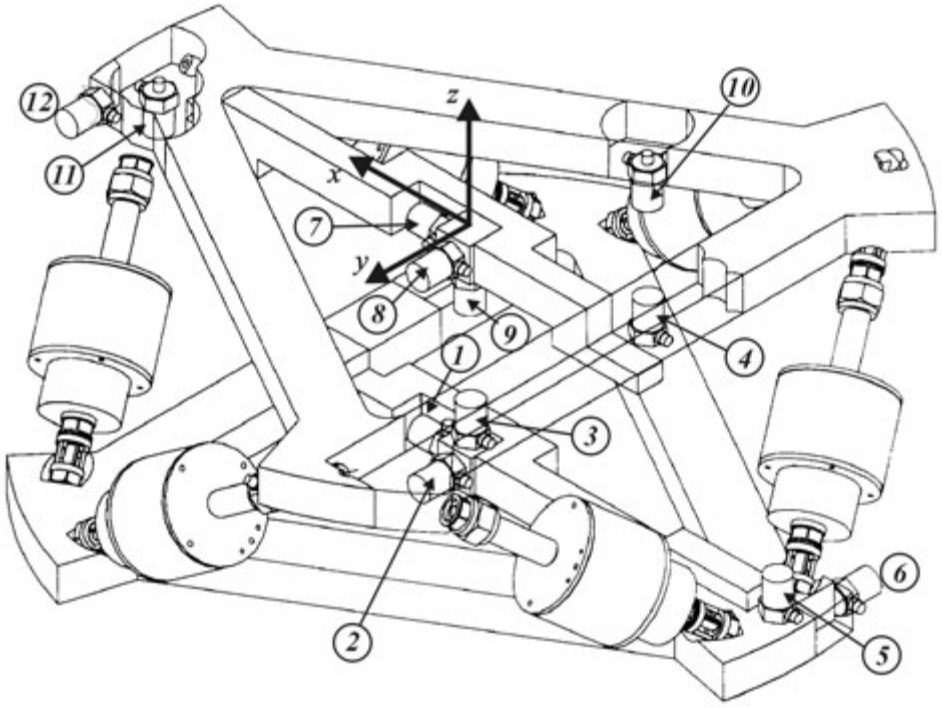

Figure 3.37: *Configuration of the twelve accelerometers fixed to the lower and upper plates*

Figure 3.38 shows the configuration of each leg with respect to the upper and the lower plates. The vector x_1 corresponds to the vector of accelerations of the lower ends of the six legs where each acceleration is in the direction parallel to the corresponding leg. The vector x_2 corresponds to the vector of accelerations of the upper ends of the six legs where each acceleration is in the direction of the corresponding leg. In order to calculate the performance of the system, one can transform the readings of the accelerometers configured as in Fig.3.37 into accelerations parallel to the legs (Fig.3.38).
Assume that y_2 is the (6×1) vector consisting of the acceleration readings measured by the six accelerometers on the upper plate $\{7, 8, 9, 10, 11, 12\}$ at a specific frequency and u_1 is the (6×1) vector consisting of the acceleration readings measured by the six

accelerometers on the lower plate $\{1, 2, 3, 4, 5, 6\}$ at the same frequency then,

$$y_2 = Pu_1 \tag{3.36}$$

where P is the (6×6) transmissibility matrix having the six lower accelerations as inputs and the six upper ones as outputs measured at the same frequency. The accelerations on the lower plate u_1 can be transformed into accelerations on the lower ends and parallel to the six legs x_1 by the equation

$$x_1 = \beta u_1 \tag{3.37}$$

where β is a (6×6) transformation matrix. β^{-1} can be estimated from the geometry and it reads

$$\beta^{-1} = \begin{pmatrix} 1/\sqrt{2} & 1/\sqrt{2} & -\sqrt{3/2} & 1/\sqrt{2} & 1/\sqrt{2} & -\sqrt{3/2} \\ 1/\sqrt{6} & -1/\sqrt{6} & 0 & 1/\sqrt{6} & -1/\sqrt{6} & 0 \\ 1/\sqrt{3} & 1/\sqrt{3} & 1/\sqrt{3} & 1/\sqrt{3} & 1/\sqrt{3} & 1/\sqrt{3} \\ 5\sqrt{3}/9 & \sqrt{3}/9 & \sqrt{3}/9 & \sqrt{3}/3 & \sqrt{3}/3 & 5\sqrt{3}/9 \\ \sqrt{3}/6 & \sqrt{3}/6 & \sqrt{3}/6 & 2\sqrt{3}/3 & 2\sqrt{3}/3 & \sqrt{3}/6 \\ 0 & 0 & \sqrt{6}/6 & -\sqrt{6}/3 & \sqrt{6}/3 & -\sqrt{6}/6 \end{pmatrix} \tag{3.38}$$

The accelerations on the upper plate y_2 can be transformed into accelerations on the upper ends and parallel to the six legs x_2 by the equation

$$y_2 = \psi x_2 \tag{3.39}$$

where ψ is a (6×6) transformation matrix. ψ can be estimated from the geometry and it reads

$$\psi = \begin{pmatrix} 1/\sqrt{2} & 1/\sqrt{2} & -\sqrt{3/2} & 1/\sqrt{2} & 1/\sqrt{2} & -\sqrt{3/2} \\ 1/\sqrt{6} & -1/\sqrt{6} & 0 & 1/\sqrt{6} & -1/\sqrt{6} & 0 \\ -1/\sqrt{3} & -1/\sqrt{3} & -1/\sqrt{3} & -1/\sqrt{3} & -1/\sqrt{3} & -1/\sqrt{3} \\ -\sqrt{3}/3 & -\sqrt{3}/3 & -\sqrt{3}/9 & -\sqrt{3}/9 & -5\sqrt{3}/9 & -5\sqrt{3}/9 \\ -2\sqrt{3}/3 & -2\sqrt{3}/3 & -\sqrt{3}/6 & -\sqrt{3}/3 & -\sqrt{3}/6 & -\sqrt{3}/6 \\ \sqrt{6}/3 & -\sqrt{6}/3 & \sqrt{6}/6 & 0 & 0 & -\sqrt{6}/6 \end{pmatrix} \tag{3.40}$$

Substituting the equations (3.37) and (3.39) into Equ.(3.36) results in the transmissibility matrix between the accelerations of the lower ends of the legs x_1 and the accelerations of the upper ends of the legs x_2

$$x_2 = Gx_1 = \psi^{-1} P \beta^{-1} x_1 \tag{3.41}$$

The transmissibility matrix G then reads

$$G = \psi^{-1} P \beta^{-1} \tag{3.42}$$

The total performance of the system is then calculated by estimating the 6-axis transmissibility transfer matrix that can be estimated over the desired frequency using the Frobenius norm [20, 21, 32]

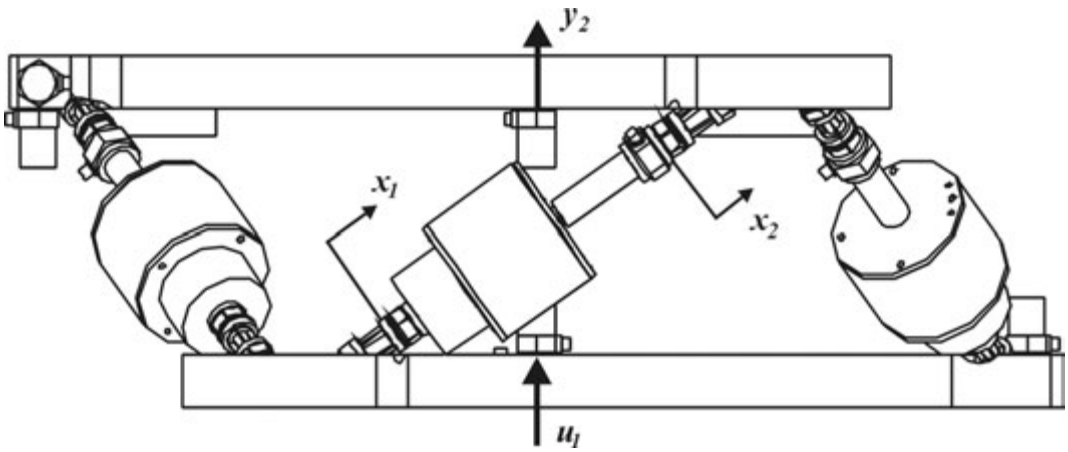

Figure 3.38: *Configuration of the displacements of one leg with respect to the upper and lower plates*

$$F(\omega) = (\sum_{k=1}^{6}\sum_{l=1}^{6} |G_{kl}(j\omega)|^2)^{1/2} \tag{3.43}$$

This results in a single frequency response that represents the norm of the transmissibility of the six-axis isolator.
Another way to assess the performance is to calculate the H_2 norm as follows [37]

$$\|G\|_2^{\,2} = \frac{1}{2\pi}\int_{-\infty}^{+\infty} \underbrace{trace[G(j\omega)G^*(j\omega)]}_{T}\, d\omega \tag{3.44}$$

The H_2 norm is interesting here because it is, in fact, the root mean square (rms) sum of the norms of the individual modes.

3.12.5 Experimental results

The open-loop FRF between the voltage input to the current amplifier, used to drive the actuator, and the signal output of the charge amplifier, used to condition the signal of the force sensor, in each leg separately has been calculated from the measured signals in time domain (using a white noise excitation). The procedure was repeated in all the six legs. Figure 3.39 shows a measured FRF between the actuator and the force sensor in one of the legs; this FRF shows two bands of modes: the first band ranges from 3.5 to 8.5 Hz and represents the rigid body modes of the mobile plate and the second band of modes appears between 600 and 1000 Hz and represents the bending modes of the triangular upper plate of the Stewart platform. The zero appearing at 3 Hz is due to the bending stiffness of the flexible joints and limits the control authority of the system. Another band of resonances exist between 60 and 110 Hz but as already observed in the preliminary ground test, it does not appear in this FRF because these latter frequencies are the local lateral modes of the hexapod legs; which are neither observable by the force sensor nor controllable by the actuator of that leg. Again, this is surprizing because it was expected from the force sensor of one leg to observe the lateral modes of the adjacent orthogonal legs. More

details about these modes will be shown in discussing the performance transmissibility results.

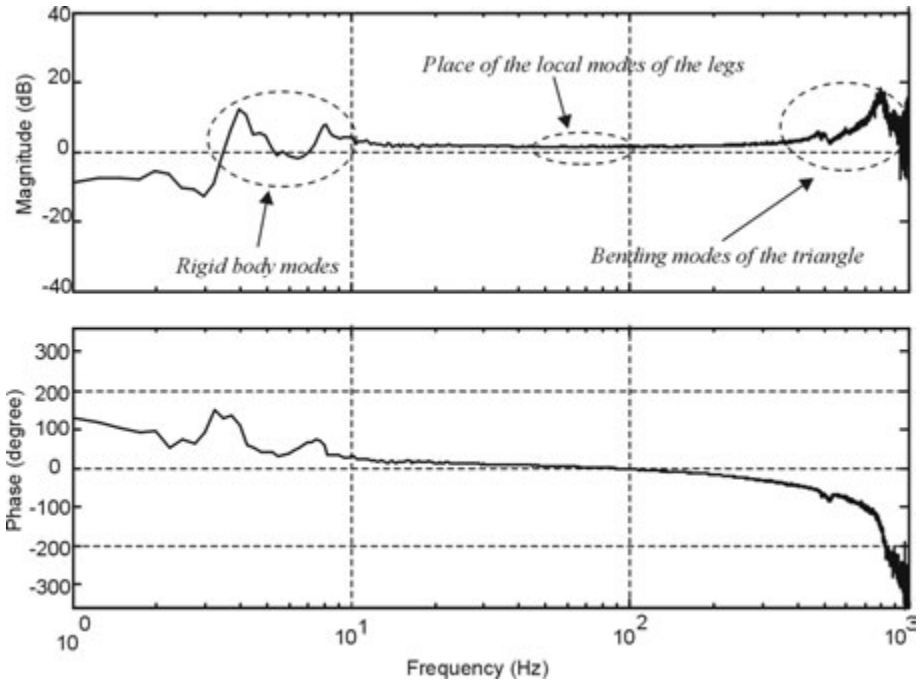

Figure 3.39: *Open-loop FRF between the actuator and the force sensor in one leg of the hexapod*

The isolator has been tested first with a Lag-Lead compensator. Figure 3.40 shows the transmissibility FRF between the signal of the accelerometer (#3) fixed in the z-direction at the lower plate and the accelerometer fixed at the upper plate in the same direction (#9). The curve indicated by (open-loop) is the z-direction transmissibility in open-loop configuration while the curve called (closed-loop) is the transmissibility with applying the Lag-Lead control technique. Figure 3.41 shows the part called T of the H_2 norm of the transmissibility with and without control calculated as explained previously in Equ.(3.44). The isolator has been experimented again by using a sky-hook control technique (Integral force feedback). This control technique is based on using a simple integration of the measured force signals and feeding the signal back to the voice coil actuator. The stability robustness property of this control strategy have been stressed in chapter 2. A high pass filter has been added at low frequency to avoid the low frequency signals from propagating into the system and to prevent the integration of the static component coming from the offset of the electronics. Figure 3.42 shows the transmissibility FRF between the accelerometer 3 fixed in the z-direction at the lower plate and accelerometer 9 fixed at the upper plate in the same direction. The curve indicated by (open-loop) is the z-direction transmissibility without control while the curve called (closed-loop) is the transmissibility with applying the sky-hook control technique. Figure 3.43 shows the part called T of the H_2 norm of the transmissibility with and without control calculated as explained in Equ.(3.44).

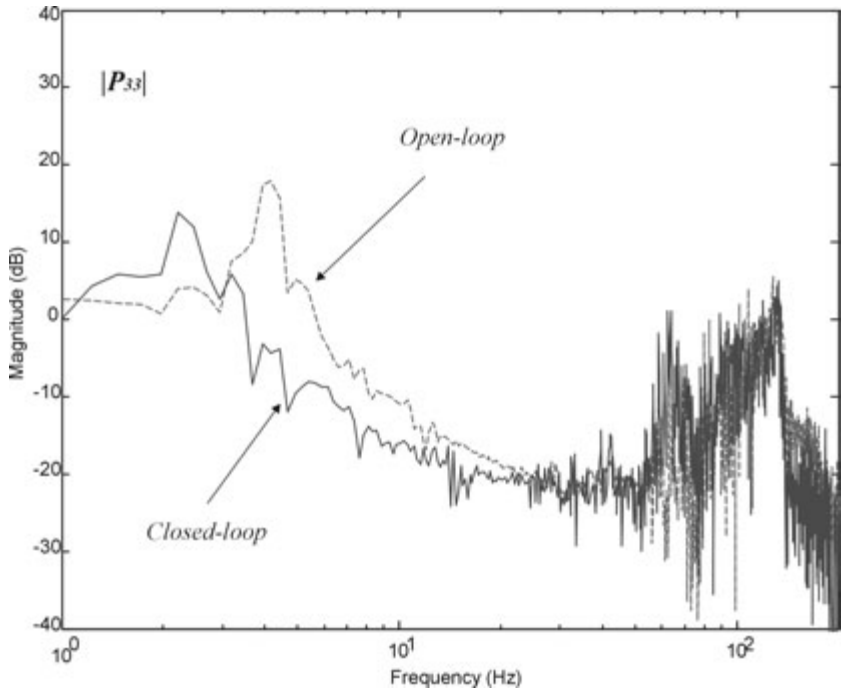

Figure 3.40: *Transmissibility FRF between the lower and the upper plates in vertical direction; without control (open-loop) and with applying Lag-Lead compensator (closed-loop)*

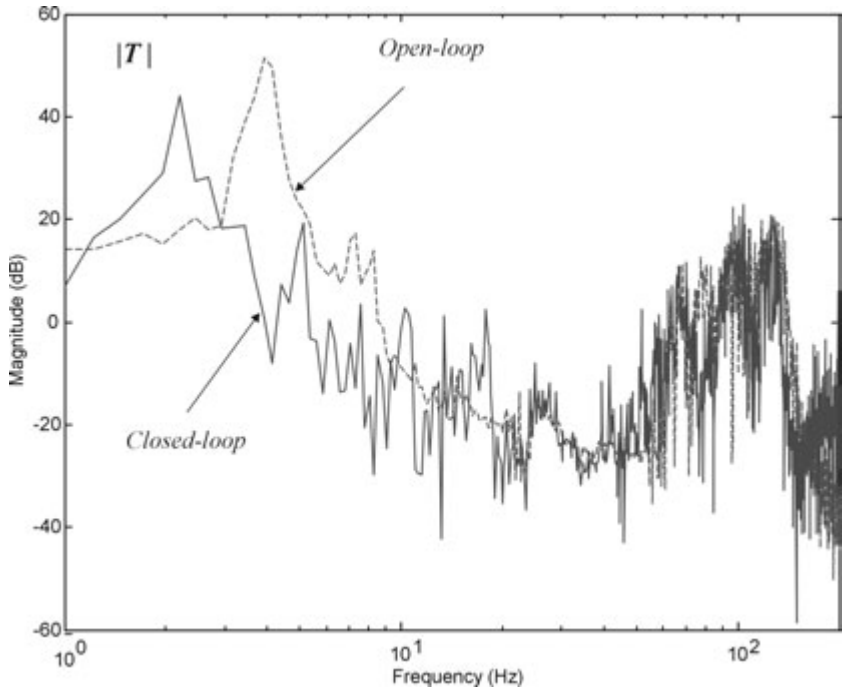

Figure 3.41: *Six-axis transmissibility FRF between the lower and the upper plates; without control (open-loop) and with applying Lag-Lead compensator (closed-loop)*

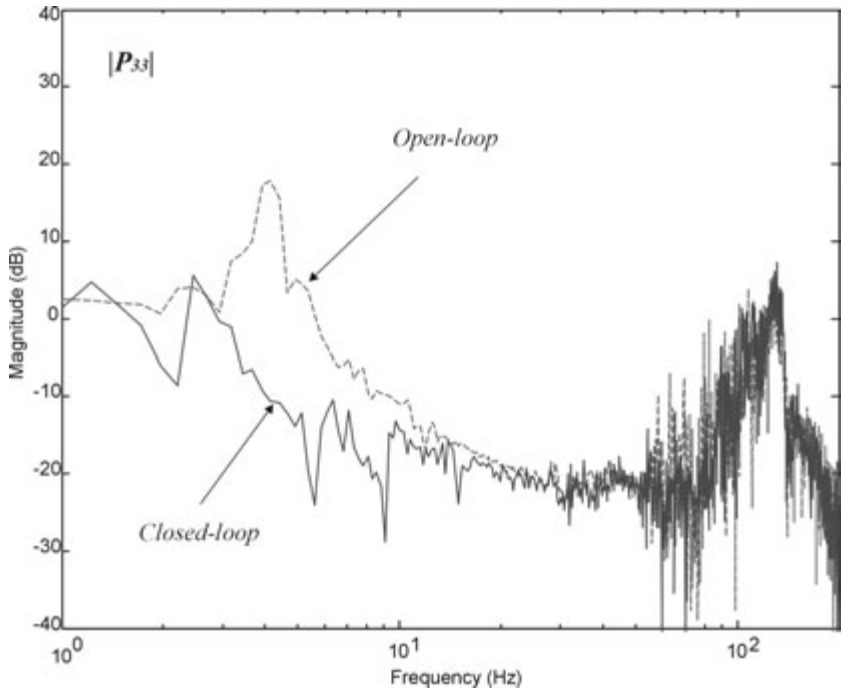

Figure 3.42: *Transmissibility FRF between the lower and the upper plates in the vertical direction; without control (open-loop) and with applying integral force feedback controller (closed-loop)*

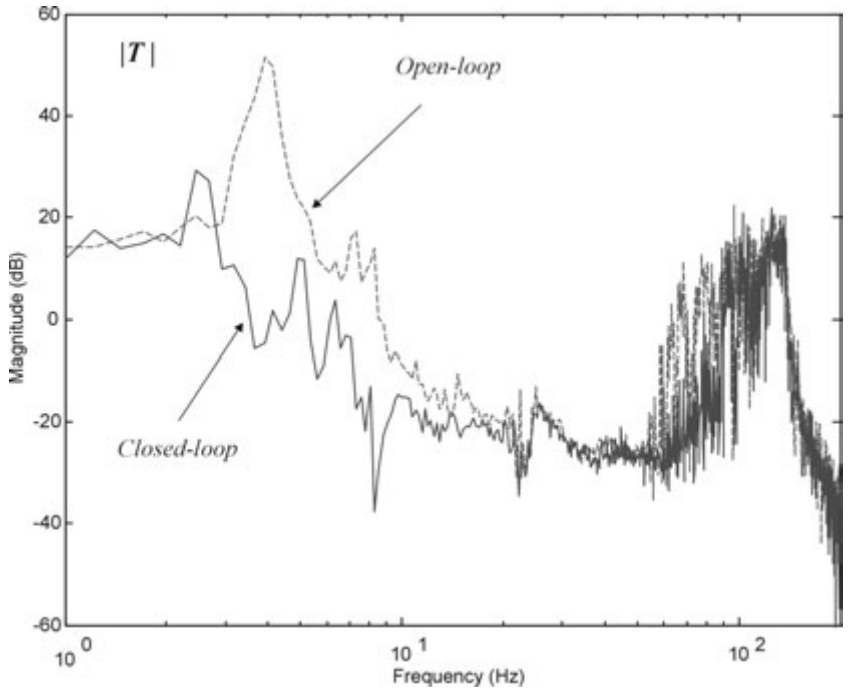

Figure 3.43: *Six-axis transmissibility FRF between the lower and the upper plates; without control (open-loop) and with applying integral force feedback controller (closed-loop)*

3.12.6 Discussion of the results

In spite of the short duration of the test (20 seconds), the results were encouraging; the quality of the bode plots was good and less noisy than we expected (see Fig.3.43). Using force feedback control strategies succeeded in removing the overshoots at low frequency while having guaranteed stability. The integral force feedback proved to be more efficient than the Lag-Lead controller especially at high frequency where it could even contribute in damping the local modes as can be seen in Fig.3.43.
Recall that the ideal transmissibility functions for all the degrees of freedom consists of a unit transmission (0 dB) at low frequency below the corner frequency of the isolator and a -40 dB/decade attenuation rate at high frequency. Unfortunately, the high frequency attenuation has been deteriorated by the local lateral modes of the legs of the hexapod. These lateral modes are a mixture of shear and bending resonances formed by the heavy masses of the voice coil actuators and the flexibility of the guiding membranes and the flexible joints in each leg. The local dynamics of the legs are orthogonal to the axial direction of the legs, which makes them neither observable by the force sensors nor controllable by the actuators. There are three suggested solutions for this problem:

- Adding visco-elastic material to add some passive damping to the lateral motion of the legs. This material can be added to the flexible joints or to the actuators or both.
- Redesigning the actuators to have lighter weight and higher lateral stiffness of the membranes.
- Moving the center of gravity of the leg towards the bending point of the flexible joints to reduce the effect of the inertia of the legs.

Looking at Fig.3.41, one can see that near the rigid body modes of the upper plate (up to 10 Hz) the transmissibility has been reduced remarkably by the effect of the active control. This controller is more or less in line with the expectations (from chapter 2); it caused a reduction of the corner frequency and produced a substantial overshoot at low frequency.
The integral force feedback technique (Fig.3.43) proved better than the Lag-Lead compensator in terms of damping of the low frequency modes, and even the high frequency lateral modes are influenced and reduced, even though, this does not change the fact that the high frequency lateral modes are still problematic.

3.12.7 Remarks

At low frequency, the acquired signals are poor and noisy and there is a lack of information which can be referred to:

1. The lack of sensitivity of the accelerometers at low frequency which reduces the coherence between the excitation at the lower plate and the response of the upper one. Figure 3.44 shows the coherence between the lower and the upper plates in the vertical direction. This figure shows that the coherence is very bad below 3 Hz.

2. The electronics have been manufactured in house and they contain a little amount of the offset (2 - 4 mV). There are two sources of the offset; the first comes from the charge amplifiers used for the force sensors and the second is from the power amplifiers used to drive the control actuators. The offset coming from the charge amplifiers has more influence than the one coming from the power amplifiers.

3. The sampling frequency in the DSP was limited to 2000 Hz by the large number of inputs, outputs and calculations done by the DSP to run the control software of the system.

4. The time available to acquire data is very short (20 seconds) which makes it difficult to have better transfer functions.

5. The aircraft produces very high noise at various frequencies that disturb the measurement.

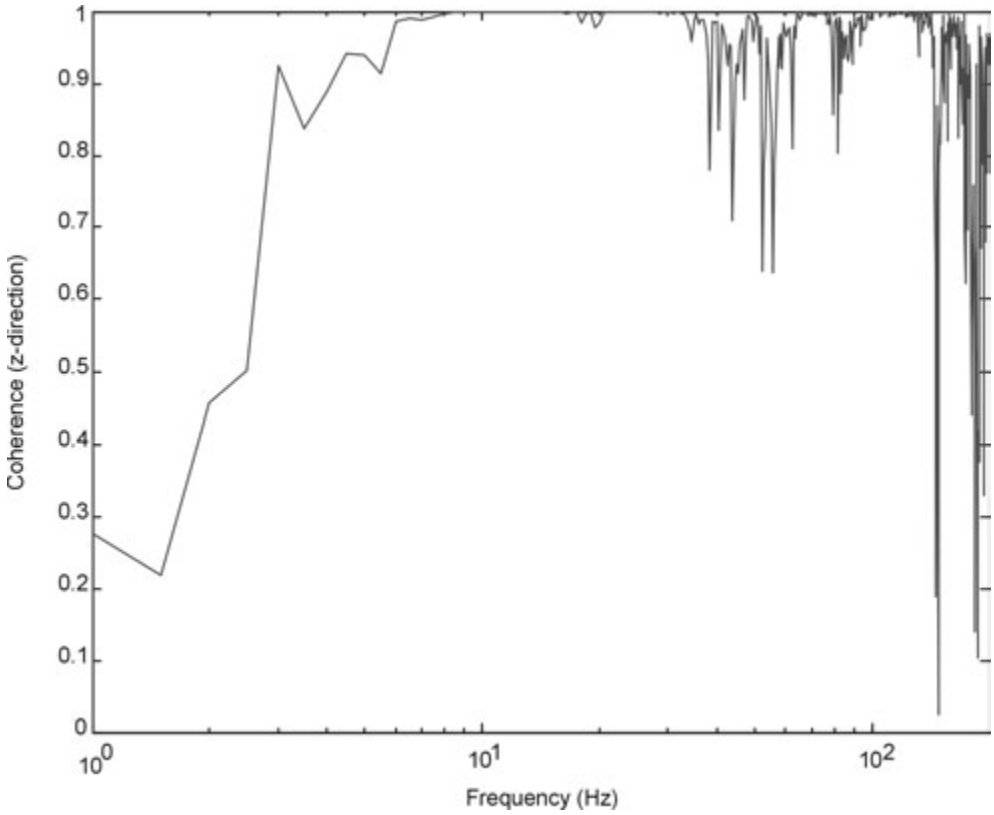

Figure 3.44: *Coherence between the lower and the upper plates in the vertical direction*

3.13 References

[1] D. Stewart. A platform with six degrees of freedom. *Proc. Instn. Mech. Engrs.*, 180(15):371–386, 1965-66.

[2] K. Cappel. Six degrees of freedom. In *Mechanical Engineering Magazine*, page 6. November 2002.

[3] V.E. Gough and S.G. Whitehall. Universal tyre testing machine. *Proc. Ninth International Technical Congress F.I.S.I.T.A.*, 117, May 1962.

[4] Z. Geng and L. Haynes. Six degrees-of-freedom active vibration control using the Stewart platforms. *IEEE Transactions on Control Systems Technology*, 2(1):45–53, March 1994.

[5] Z. Geng and L. Haynes. Six-degree-of-freedom active vibration isolation using a Stewart platform mechanism. *Journal of Robotic Systems*, 10(5):725–744, 1993.

[6] C. Reboulet and T. Berthomieu. Dynamic models of a six degree of freedom parallel manipulators. *IEEE*, pages 1153–1157, 1991.

[7] J.-P. Merlet. An algorithm for the forward kinematics of general parallel manipulators. *IEEE*, pages 1136–1140, 1991.

[8] J P Merlet. *Les Robots Paralleles*. Hermes, 2nd edition, 1997.

[9] K.H. Pittens and R.P. Podhorodeski. A family of Stewart platforms with optimal dexterity. *Journal of Robotic Systems*, 10(4):463–479, 1993.

[10] J. McInroy, J. O'Brien, and G. Neat. Precise, fault-tolerant pointing using a Stewart platform. *IEEE/ASME Transactions on mechatronics*, 4:91–95, March 1999.

[11] J. McInroy. Dynamic modeling of flexure jointed hexapods for control purposes. In *Proceedings of the 1999 IEEE International Conference on Control Applications*, pages 508–513, Kohala Coast-Island of Hawaii, USA, August 1999.

[12] J. McInroy, G. Neat, and J. O'Brien. A robotic approach to fault-tolerant, precision pointing. *IEEE Robotics and Automation Magazine*, pages 24–37, December 1999.

[13] J. McInroy and J. Hamann. Design and control of flexure jointed hexapods. *IEEE Transaction on Robotics*, 16(4):372–381, August 2000.

[14] I. Bonev and J. Ryu. A new method for solving the direct kinematics of general 6-6 Stewart platforms using three linear extra sensors. *Mechanism and Machine Theory*, 35:423–436, 2000.

[15] C. Zhang and S. Song. Forward position analysis of nearly general Stewart platforms. *Transactions of the ASME*, 116:54–58, March 1994.

[16] L. Baron and J. Angeles. The kinematic decoupling of parallel manipulators using joint-sensor data. *IEEE Transactions on Robotics and Automation*, 16(6):644–651, December 2000.

[17] C. Gosselin. Determination of the workspace of 6-DOF parallel manipulators. *Journal of Mechanical Design*, 112:331–336, September 1990.

[18] J. Spanos, Z. Rahman, and G. Blackwood. A soft 6-axis active vibration isolator. In *Proceedings of the American Control Conference*, Seattle, Washington, USA, June

1995.

[19] D. Thayer, J. Vagners, A. von Flotow, C. Hardham, and K. Scribner. Six-axis vibration isolation system using soft actuator and multiple sensors. *AAS*, 064:497–506, 1998.

[20] D. Thayer, M. Kampell, and J. Vagners. Six axis vibration isolation using modern control techniques. In *21st Annual AAS Guidance and Control Conference*, February 1998.

[21] D. Thayer, M. Kampell, J. Vagners, and A. von Flotow. Six axis vibration isolation system using soft actuators and multiple sensors. *Journal of Spacecraft and Rockets*, 39(2), March-April 2002.

[22] J. Fochage, T. Davis, J. Sullivan, T. Hoffman, and A. Das. Hybrid active/passive actuator for spacecraft vibration isolation and suppression. *SPIE*, 2865:104–122, March 1996.

[23] C. Taranti, B. Agrawal, and R. Cristi. An efficient algorithm for vibration suppression to meet pointing requirements of optical payloads. *AIAA Guidance, Navigation and Control Conference and Exhibition*, August 2001.

[24] R. Taranti, C. Cristi and B. Agrawal. State-space equations for a high-precision pointing hexapod. *IEEE Conference on Control Applications (CCA)*, 2001.

[25] A. Abu Hanieh, M. Horodinca, and A. Preumont. A soft-actuator active hexapod for the purpose of vibration isolation. In *International Conference on Noise and Vibration Engineering*, KUL, Leuven, Belgium, September 2002.

[26] A. Abu Hanieh, M. Horodinca, A. Preumont, N. Loix, and J.Ph. Verschueren. Stiff and soft Stewart platforms for active damping and active isolation of vibrations. In *Actuator 2002*, Bremen, Germany, June 2002.

[27] A. Abu Hanieh, M. Horodinca, and A. Preumont. Six-degree-of-freedom hexapods for active damping and active isolation of vibrations. *Journal de Physique*, 12(Pr11-41), December 2002.

[28] M. Horodinca, A. Abu Hanieh, and A. Preumont. A soft six degrees of freedom active vibration isolator based on Stewart platform. In *International Symposium on Active Control of Sound and Vibration (Active 2002)*, Southampton, UK, July 2002.

[29] G. Hauge and M. Campbell. Shaping the transmissibility for six-axis active vibration isolators. *AIAA*, 1287, 1999.

[30] D. Edberg and B. Wilson. Design and testing of reduced-stiffness umbilicals for space station microgravity isolation. *Journal of Spacecraft and Rockets*, 38(4):563–568, August 2001.

[31] Z. Rahman, J. Spanos, and G. Blackwood. Active narrow-band vibration isolation of large engineering structures. In *Proceedings of the First World Conference on Structural Control*, Pasadena, USA, August 1994.

[32] Z. Rahman, J. Spanos, and R. Laskin. Multi-axis vibration isolation, suppression and steering system for space observational applications. In *SPIE International Symposium on Astronomical Telescopes and Instrumentation*, Kona-Hawaii, March 1998.

[33] J. Moerschell. *Micropositioning Course.* Swiss Foundation for Research in Microtechnology, Switzerland, 1999.

[34] Physik Instruments. *Physik Instruments catalogue.*

[35] Y. Chen and J. McInroy. Identification and decoupling control of flexure jointed hexapods. In *International Conference on Robotics and Automation*, San Francisco, April 2000.

[36] A. Preumont. *Vibration Control of Active Structures.* Kluwer Academic Publishers, Netherlands, 2nd edition, 2002.

[37] W. Gawronski. *Dynamics and Control of Structures, A Modal Approach.* Springer-Verlag, New York, 1998.

Chapter 4

Systems with piezoelectric actuators

4.1 Introduction

The main requirement on the supporting trusses in many space and ground applications is stability rather than precision. This specification on the structural stability for scientific space missions, combined with the requirement for lightweight structures, has triggered extensive researches in the area of active damping of flexible structures. These have led to numerous solutions, most of them are based on the integration of SMART actuators and sensors in the structure itself. ASL is one of the pioneers in active strut control; several methods have been investigated by the ASL for the active damping of mechanical structures:

1. Replacing some bars of the truss by active struts [1, 2].
2. Using active tendons [3, 4].
3. Using six-axis damping interface based on Stewart platform (will be discussed in details in this chapter).

In this chapter, we present some systems with stiff piezoelectric actuators. The main idea is to show the use of active struts for the purpose of active damping of vibrations; an active strut consists of a piezo stack providing a displacement actuator and a collocated force sensor (Fig.1.9 shows three options of active struts). The active strut configuration can be used for damping in connection with the Integral Force Feedback (IFF) controller for various system architectures: Active truss [1], active tendon control of cable structures [5] and active support [6]. Later, we will emphasize that if we change the control law to Proportional plus Integral (PI), the system can also be used for stiffness reduction. This chapter will also discuss the design of a new six-axis active damping and precision pointing interface based on the cubic Stewart platform using piezoelectric actuators.

4.2 Active strut control

The research on active strut in the ASL began in the late 80's. The first mechanical structure used for this purpose is the active truss shown in Fig.4.1. Figure 1.8 shows a schematic of a general truss with some of its members replaced by active struts; each of them consists of a piezoelectric linear actuator colinear with a force sensor [2].

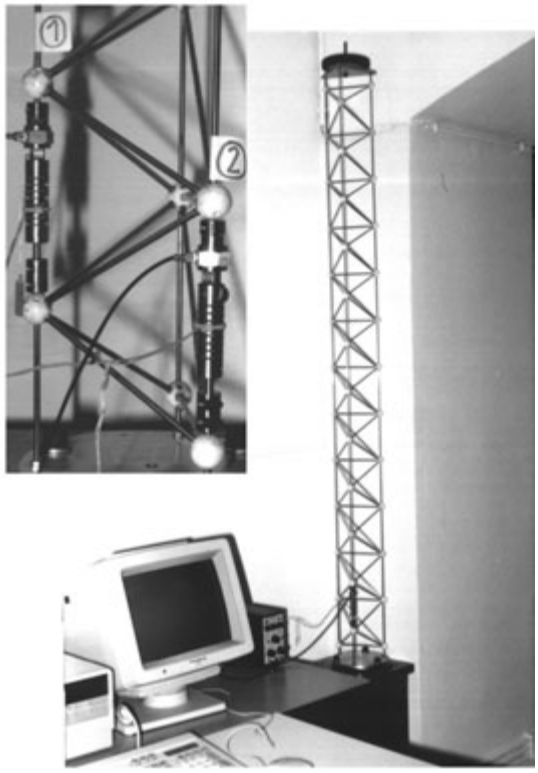

Figure 4.1: *ASL active truss*

If k is the stiffness of the active strut and δ is the extension of the piezo stack, the piezoelectric loads applied axially to both ends of the active strut are (Fig.1.8)

$$p = k\delta \tag{4.1}$$

Assuming no damping in the structure, the governing equation of motion of the truss excited by one single actuator is

$$M\ddot{x} + Kx = bk\delta \tag{4.2}$$

where M is the global mass matrix of the truss, K is the global stiffness matrix and b is the influence vector showing the location of the active strut in the global coordinates of the truss. Knowing that the total extension q is the projection of the displacement on the active strut ($q = b^T x$), the output signal of the force sensor, proportional to the elastic extension of the truss, is

$$y = k(b^T x - \delta) \tag{4.3}$$

Applying the IFF active control technique between the signal output of the force sensor and the extension of the piezo actuator, the controller equation reads

$$\delta = \frac{g}{ks} y \tag{4.4}$$

Note the positive sign in the feedback law. Neglecting the hyteresis between the voltage and the displacement of the piezo actuator, Equ.(4.4) can be considered between the signal output of the force sensor and the signal input to the piezoelectric actuator. Combining equations (4.3) and (4.4), we get

$$\delta = \frac{g}{s+g} b^T x \tag{4.5}$$

Substituting δ into Equ.(4.2) and taking the Laplace transform, we get the closed-loop characteristic equation

$$[Ms^2 + K - \frac{g}{s+g}(bkb^T)]x = 0 \tag{4.6}$$

The asymptotic solution of this characteristic equation as $g \to \infty$ results in the asymptotic values of the closed-loop poles that are equal to the zeros of the open-loop system; these are solutions of the eigenvalue problem $(Ms^2 + K - bkb^T)x = 0$, corresponding to the natural frequencies of the truss when the active strut has been removed.

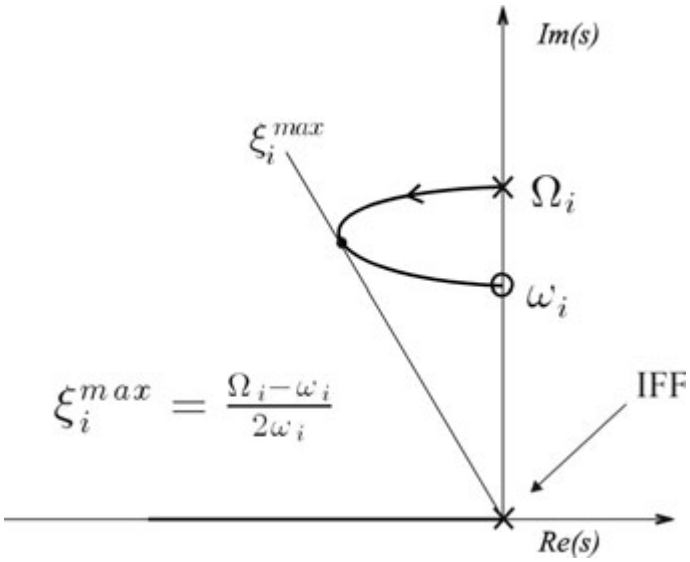

Figure 4.2: *Root locus for mode i*

Changing the variables by $x = \Phi z$, Equ.(4.6) can be transformed into modal coordinates to estimate the modal damping. Normalizing the mode shapes with $\Phi^T M \Phi = I$ and taking into account that $\Phi^T K \Phi = diag(\Omega_i^2) = \Omega^2$, we get

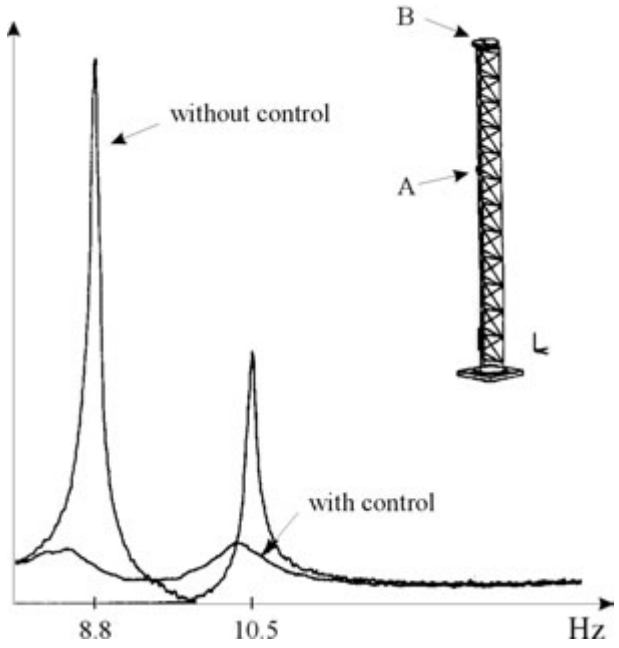

Figure 4.3: *Frequency response between A and B, with and without control*

$$[Is^2 + \Omega^2 - \frac{g}{s+g}\Phi^T(bkb^T)\Phi]z = 0 \tag{4.7}$$

Assuming that the matrix $\Phi^T(bkb^T)\Phi$ is diagonally dominant and neglecting the off-diagonal terms

$$\Phi^T(bkb^T)\Phi \approx diag(\nu_i\Omega_i^2) \tag{4.8}$$

where ν_i is the fraction of strain energy in the active strut when the truss vibrates according to the mode i (more details can be found in [2]). Substituting Equ.(4.8) into (4.7), we get

$$s^2 + \Omega_i^2 - \frac{g}{s+g}\nu_i\Omega_i^2 = 0 \tag{4.9}$$

For a small gain g, one can assume a solution of $s \approx -\xi_i\Omega_i \pm j\Omega_i$ where ξ_i is the damping ratio of mode i, this results in

$$\xi_i = \frac{g\nu_i}{2\Omega_i} \tag{4.10}$$

Denoting $\omega_i^2 = \Omega_i^2(1-\nu_i)$, the predicted root locus of the closed-loop poles reads

$$s^2 + \Omega_i^2 - \frac{g}{s+g}(\Omega_i^2 - \omega_i^2) = 0 \tag{4.11}$$

or

$$1 + g\frac{s^2 + \omega_i^2}{s(s^2 + \Omega_i^2)} = 0 \tag{4.12}$$

It is shown in Fig.4.2; with a gain $g = \Omega_i\sqrt{\Omega_i/\omega_i}$, the maximum modal damping is given by

$$\xi_i^{max} = \frac{\Omega_i - \omega_i}{2\omega_i} \tag{4.13}$$

Figure 4.3 shows some experimental results in the frequency domain for the first two modes of the truss shown in Fig.4.1. The results show the FRF between an impulse force at mid height of the truss and the acceleration at the top of the truss.
One interesting application of active struts is the active control of vibrations of high precision machines (i.e. Lithography). The University of Twente in cooperation with ASML has developed an interface for this purpose and called "Smart Disk" [6]. It is based on the principle of active struts described above and is used to support the lens of the new generation of lithography machines.

4.3 Active tendon control

The active tendon control of cable structures has been investigated at ASL for more than 5 years [3, 4, 5, 7, 8]. The control concept is explained in Fig.4.4; the tendon consists of a piezoelectric linear actuator colinear with a force sensor. The control law is also IFF. As for the active truss described above, the closed-loop performance of the control system can be predicted from the results of two modal analyses; one performed with all the cables provides the open-loop poles (Ω_i) and another one, performed after removing the active cables, provides the zeros (ω_i), and the closed-loop poles follow, once again, the root locus shown in Fig.4.5. The active tendon control has been applied to a laboratory model of space truss and to cable stayed bridges too [7, 8, 9].

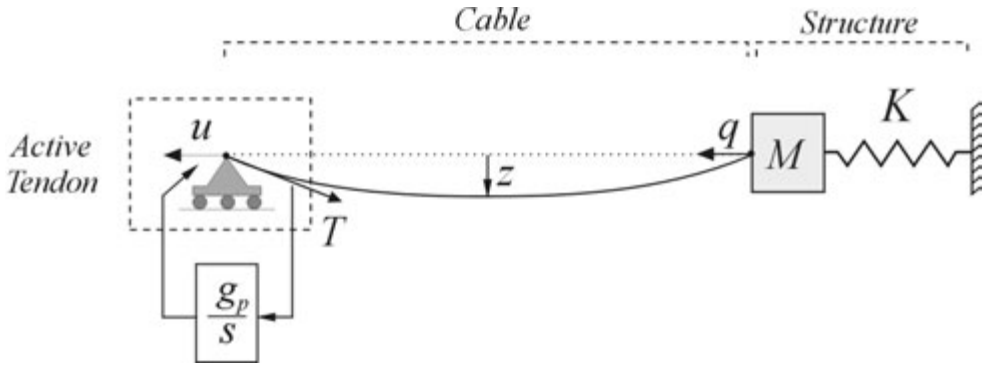

Figure 4.4: *Active damping of cable structures*

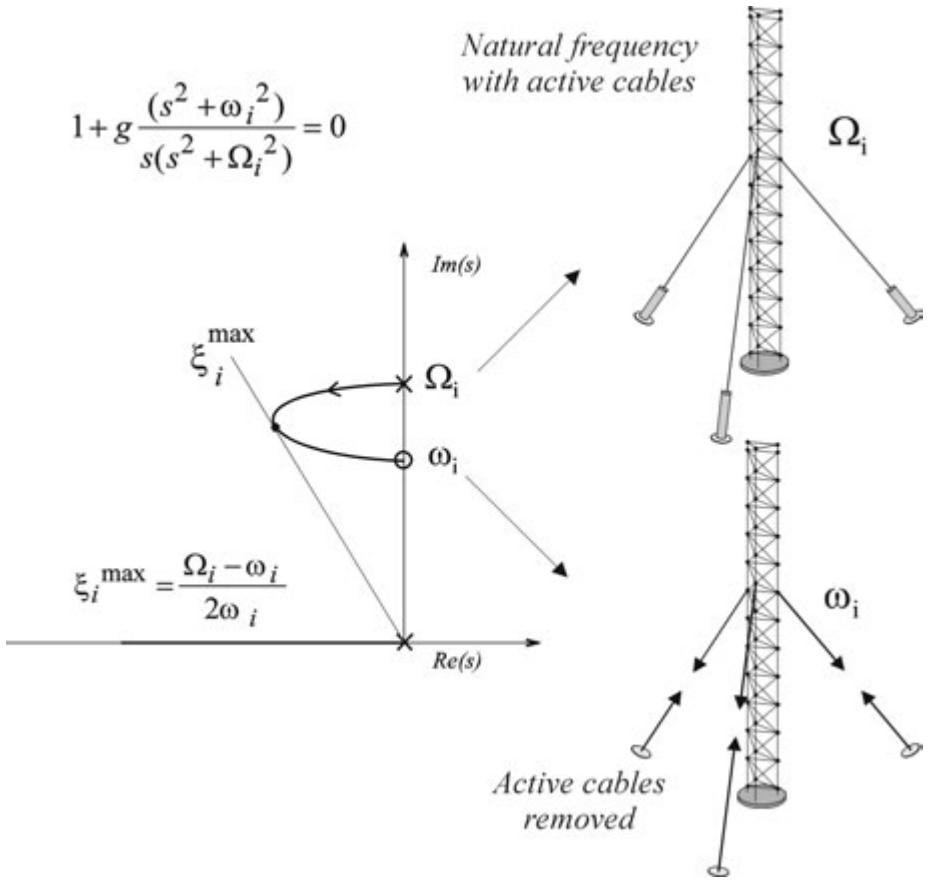

Figure 4.5: *Root locus of the closed-loop poles for active tendon control*

4.4 Frequency reduction

In the previous section, it has been shown that the active strut in connection with IFF control technique can be used for active damping of vibrations. In this section, we will show that the same concept of active strut can be used to reduce the frequency of a structure by replacing the IFF with a PI feedback control. As an application for the frequency reduction, one can imagine adaptive structures that can change their resonance frequency instantaneously to avoid being excited when the excitation frequency approaches a resonance.

Consider the single-axis system connecting two rigid bodies shown in Fig.4.6; the disturbance source m and the sensitive payload M are connected by a force sensor and a piezoelectric actuator (represented by its elongation δ and spring stiffness k). The governing equation of motion for this system in Laplace transform is:

$$Ms^2x_c = -ms^2x_d = k(x_d - x_a) = F \tag{4.14}$$

and

$$\delta = x_c - x_a \tag{4.15}$$

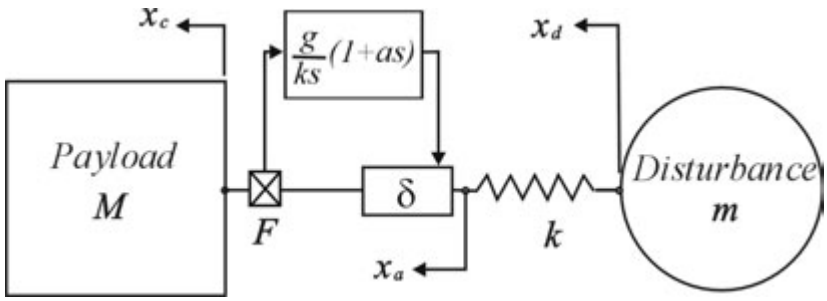

Figure 4.6: *Single-axis isolation using piezoelectric stiff actuator*

The open-loop FRF between the extension of the piezo stack in the piezoelectric actuator δ and the output of the force sensor F reads

$$\frac{F}{\delta} = k\frac{Mms^2}{Mms^2 + k(M+m)} \tag{4.16}$$

Applying a force feedback control strategy using a proportional plus integral compensator, the control law reads

$$\delta = \frac{g}{ks}(1+as)F \tag{4.17}$$

Here ga is the proportional gain and g is the integral gain. The root locus for the closed-loop poles of the this system is shown in Fig.4.7; it shows that increasing the loop gain decreases the frequency of the closed-loop poles. If the proportional term is used alone, the poles will move on the imagiary axis towards the origin but this means the risk of destabilizing the system at any instant. The use of the integral controller here pushes these poles deeper to the left half plane increasing the stability.

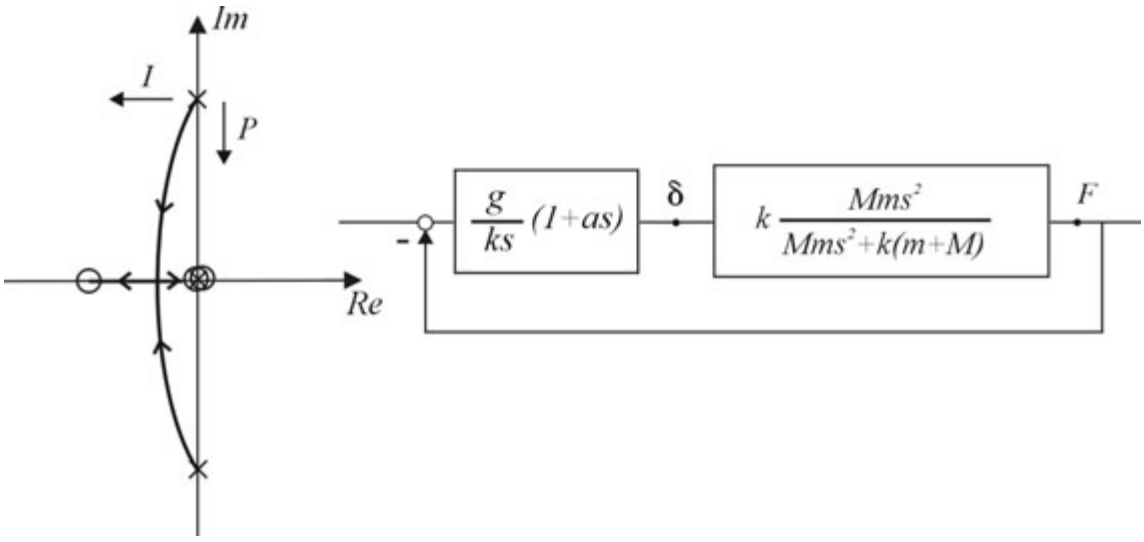

Figure 4.7: *Root locus of a single-axis system with piezoelectric actuator and PI controller*

From the analytical calculation, the intermediate displacement x_a is

$$x_a = \frac{sx_c + g(as+1)x_d}{s + g(as+1)} \tag{4.18}$$

From the foregoing equations, one can calculate the transmissibility FRF between the disturbance displacement and the payload displacement, which is equal to

$$\frac{x_c}{x_d} = \frac{1}{s^2[(1+ga)/\omega_n^2] + s[g/\omega_n^2] + 1} \tag{4.19}$$

Equ.(4.19) implies that the corner frequency ω_c of the system is determined by the proportional gain of the compensator

$$\frac{1}{\omega_c^2} = \frac{1+ga}{\omega_n^2} \tag{4.20}$$

The damping of the system is determined by the gain g of the compensator

$$\frac{g}{\omega_n^2} = \frac{2\xi}{\omega_c} \tag{4.21}$$

If ω_n is much larger than ω_c then $(\omega_n^2/\omega_c^2) \approx ga$ and

$$\frac{ga}{k} = \frac{1}{M\omega_c^2} = \frac{1}{k^*} \tag{4.22}$$

Here $(1/k^*)$ is the closed-loop flexibility of the system and is proportional to the gain. From the foregoing analysis, one can see that the closed-loop stiffness of the system is inversely proportional to the control gain; in other words, if one increases the proportional gain, the stiffness is reduced.

4.5 Experimental verification of frequency reduction

In this section, we discuss, experimentally, using the proportional plus integral (PI) controller to reduce the frequency of the structure as discussed theoreticaly in the previous section.

Consider the experimental set-up shown in Fig.4.8. It consists of two masses connected to each other by an active member; the active member consists of a piezoelectric actuator and a force sensor. Using an external shaker, the system is excited with a random signal ranging from 1 to 800 Hz and the transmissibility FRF between the displacement of the disturbance source body and that of the payload mass is measured (Fig.4.9). The resonance of the system is found at 500 Hz.

A feedback system with a PI control law is applied to the system and the same FRF measured again. Figure 4.9 shows the two measured FRFs: the open-loop (before stiffness reduction) and the closed-loop (after stiffness reduction). The natural frequency of the system has been reduced 50%; from 500 Hz to 250 Hz. The maximum reduction has been obtained by increasing the gain of the proportional part of the compensator, but this leads to the risk of walking along the imaginary axis which can lead to instability if the

surrounding conditions change slightly. Thus, there is a need to increase the integral gain too at the same time to increase the stability margin of the system.
In the same context, another expriment has been done. The same control technique has been applied to the truss structure shown in Fig.4.1. The signals of the two force sensors, in the two active struts of the truss, have been filtered using the (PI) compensator in a Digital Signal Processor (DSP) and fed back to the piezoelectric actuators. The two control loops have been closed independently, forming a decentralized controller. Again, by increasing the proportional gain, the frequency of the active struts in the structure has been reduced significantly. Figure 4.10 shows the first two modes of the FRF between

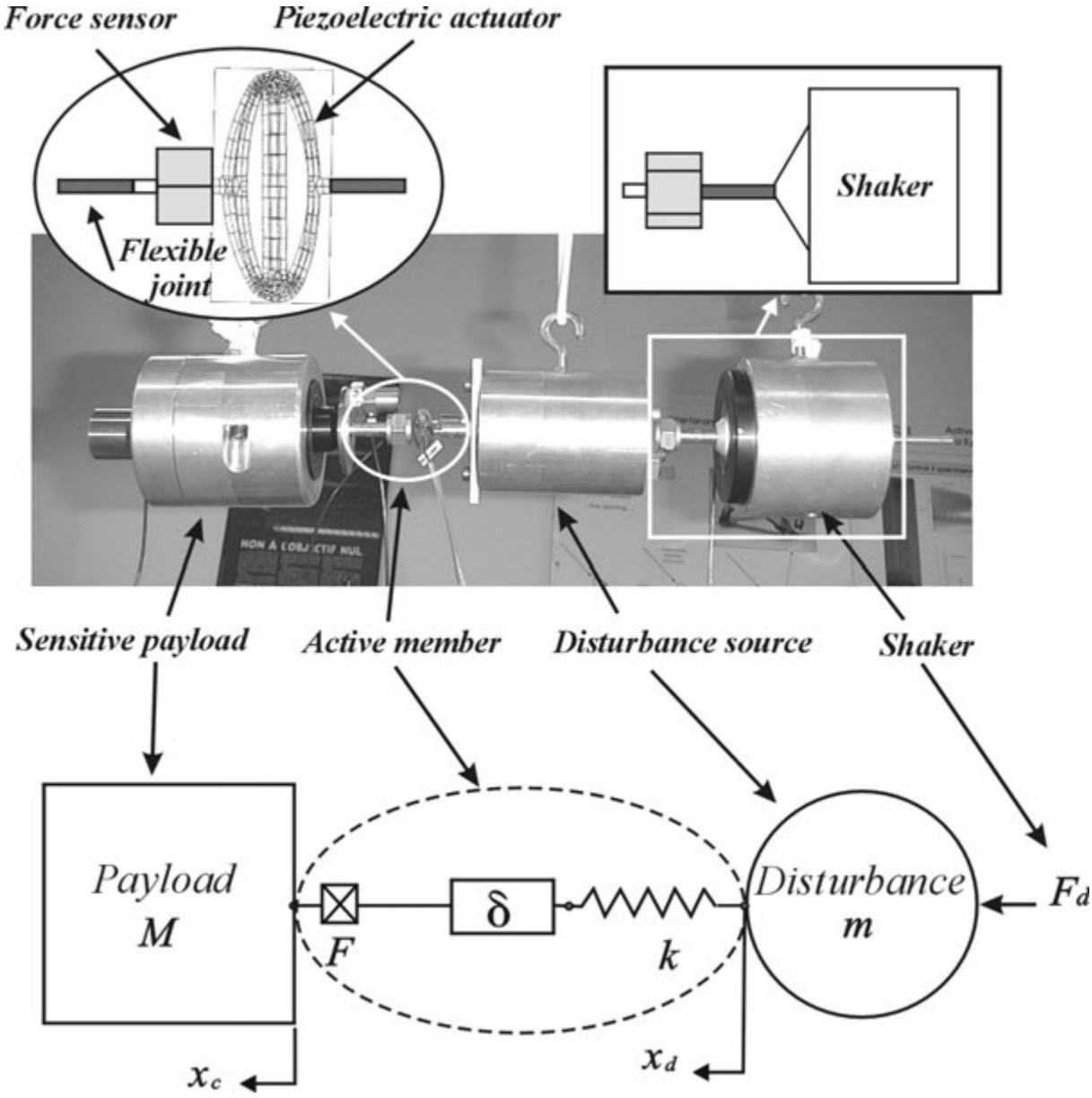

Figure 4.8: *Experimental SDOF set-up with a piezoelectric actuator*

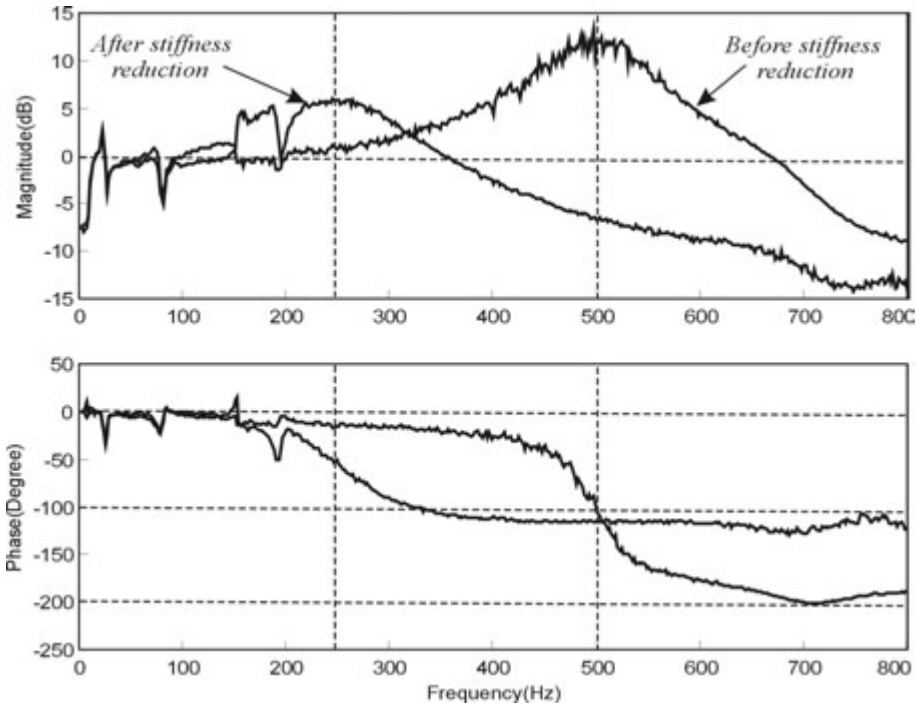

Figure 4.9: *(x_c/x_d) Transmissibility of the SDOF system before and after frequency reduction*

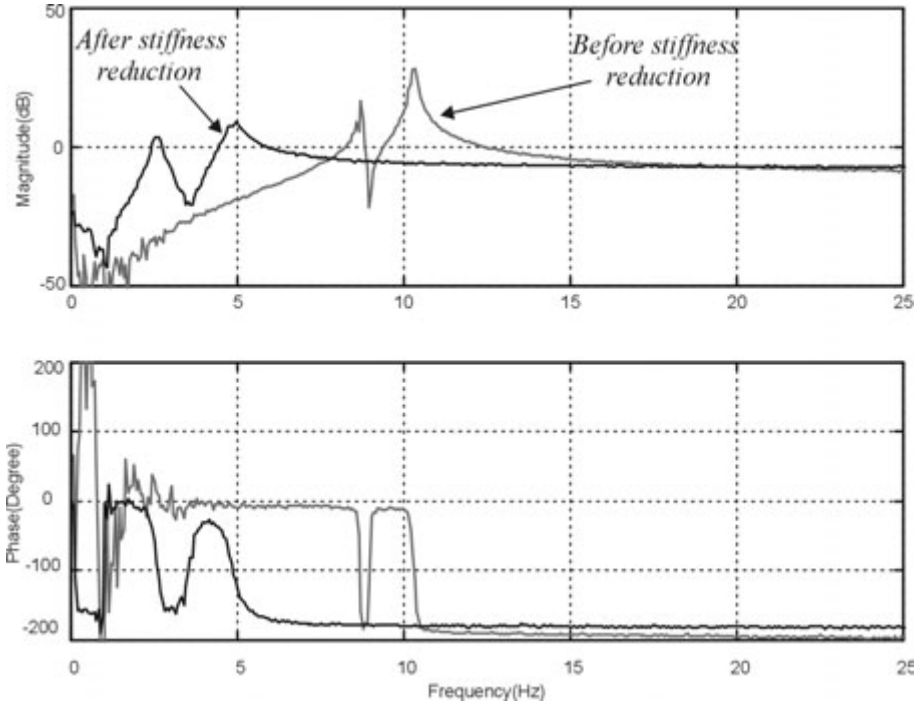

Figure 4.10: *(F/δ) FRF shows the stiffness reduction in the struts of the active truss structure fo Fig.4.1*

the voltage input to one of the actuators and the force output from the collocated force sensor. The open-loop FRF (before stiffness reduction) shows that the two modes are located at 8.8 and 10.5 Hz. Using this control technique, they have been moved to 2.6 and 5 Hz, respectively.
A potential application of this is the adaption of structural resonances to a narrow band disturbance of variable frequency.

4.6 A piezoelectric Stewart platform

Referring to the discussion in the begining of chapter 3, Fig.3.1 expresses the different configrations and applications of Stewart platforms. Besides the ability of using it as an isolation mount, Stewart platform can be used as an active damping mount and as a structural active element. To fulfil these applications, the IAI has designed a Stewart platform with magnetostrictive (Terfenol-D) actuators and cubic configuration in the early 90's [10] (see Fig.4.11).
The potential applications for the piezoelectric Stewart platform are the following:

1. Precision pointing device.
2. Vibration isolation if combined with feedforward control.
3. Active damping interface and a possible combination with pointing.

In this latter case, from previous discussion, the idea is to use the same strategy as in section 4.2 and to have strain energy concentration in the hexapod legs which would guarantee controllability on the modes as discussed in Equ.(4.10) and Fig.4.2.
A brief review of the current designs of stiff Stewart platforms is discussed in the next section showing a comparison between the different designs. The design, manufacturing and applications of the ULB piezoelectric Stewart platform [11, 12, 13, 14, 15] is then discussed in details.
Table 4.1 shows a comparison between some of the current stiff hexapods. One can notice here that there is a wide range of actuators used to operate these Stewart platforms, depending mainly on the stroke requested by the application. Piezoelectric actuators can give good accuracy in pointing but their stroke is limited, to get long stroke for the hexapod, rotary or DC motors can be used (i.e. CSA and PI) but the drawback is that the resolution that can be achieved by the pointing system is reduced. Stiff Stewart platforms are not preferred in vibration isolation unless combined with feedforward control, but they are considered as appropriate generic active damping interfaces that can damp structures very effectively if located in the appropriate manner. The hexapod produced at ULB-ASL has become a commercial product [16]. It has been tested as a damping interface for a truss structure and gave good results in terms of active suppression of vibrations.

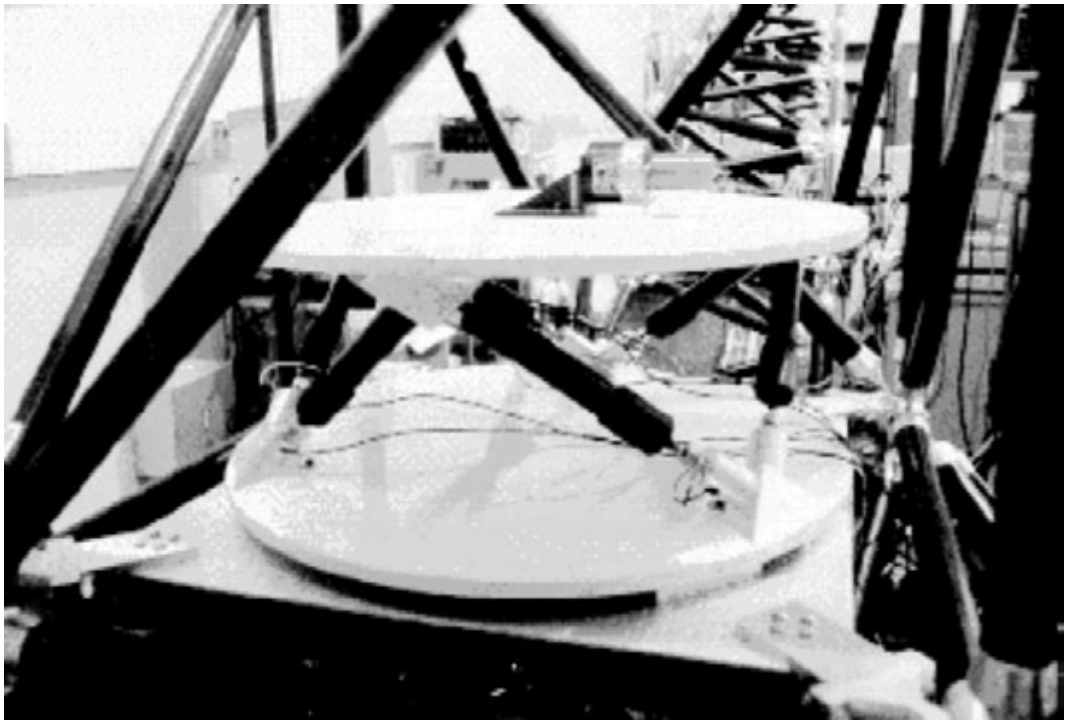

Figure 4.11: Intelligent Automation Inc. Hexapod [10]

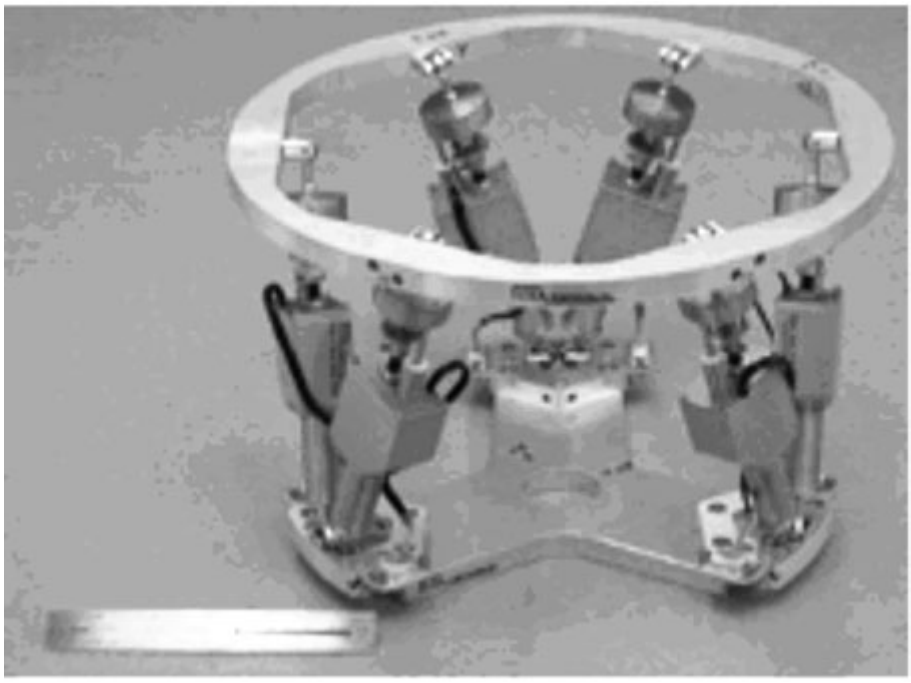

Figure 4.12: CSA Engineering stiff Hexapod [17]

Summary of current stiff Stewart platforms

Hexapod	Actuator	Actuation stroke	Feedback sensor	Configuration	Control strategy	Joints	Resolution
CSA (stiff) [17], Fig.4.12	rotary motor	±6350 μm	Payload geophones	Not cubic	—	Ball joints	2 μm
ONERA/ MATRA [18], Fig.4.13	Piezo-electric	—	Force sensors	Not cubic	Decentral. Feedforward	Universal joints	—
IAI [10], Fig.4.11	Magneto-stictive	± 127 μm	Load cells, accelerometers	Cubic	Decentral. feedforward	Flexible joints	—
MATRA/ CSEM [19], Fig.4.14	Piezo-electric	±12 μm	Force sensors	Cubic	Decentral. force feedback	Flexible pivots	0.1 μm
Physik Instruments [20], Fig.4.15	DC motors, screws	±25000 μm	Encoders	Not cubic	Static PID	Spherical, universal joints	1 μm 10 μrad
ULB (stiff) [11], Fig.4.16	Piezo-electric	±27.5 μm	Force sensors	Cubic	Decentral. force feedback	Flexible joints	0.005 μm 0.05 μrad

Table 4.1: *Comparison between several types of stiff hexapods*

Figure 4.13: ONERA/MATRA (SEPTRA) Hexapod [18]

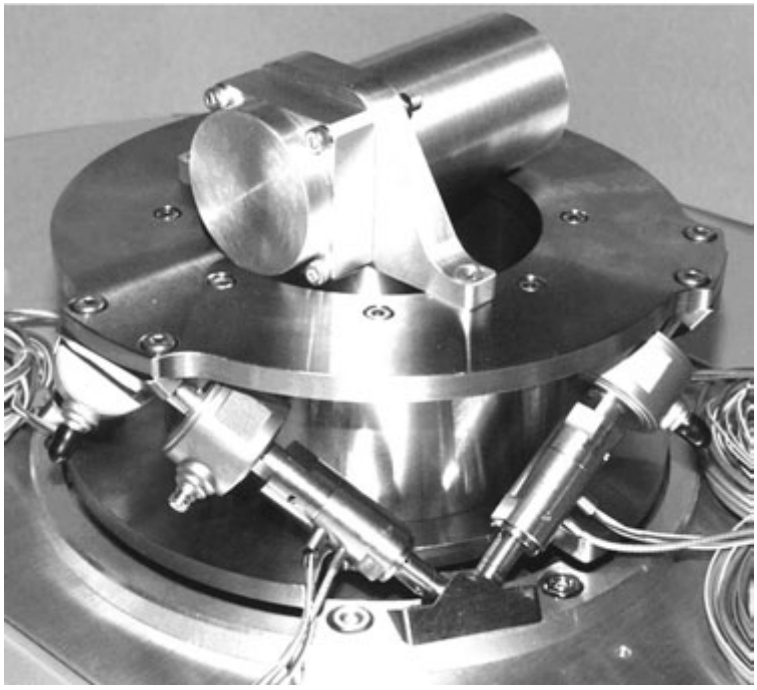

Figure 4.14: MATRA/CSEM (MAIS) Hexapod [19]

Figure 4.15: Physik Instruments Hexapod [20]

4.7 ULB piezoelectric Stewart platform

Figure 4.16 shows a picture of the ULB piezoelectric Stewart platform; Fig.4.16(a) shows the complete Stewart platform where the connectors are the inputs to the actuators and the wires are the outputs of the sensors; Fig.4.16(b) shows the hexapod with the upper plate removed to show the details and configuration of the legs.

The hexapod consists of two parallel plates connected to each other by six active legs. The legs are mounted in such a way to achieve the geometry of cubic configuration. Each active leg consists of a force sensor (B&K 8200), an amplified piezoelectric actuator (Cedrat Recherche APA50s) and two flexible joints as shown in Fig.4.17. In the ideal situation, the hexapod needs to be hinged using spherical joints, but to avoid the problem of friction and backlash, flexible tips are used instead of spherical joints. These flexible tips have the following properties: zero friction, zero backlash, high axial stiffness and relatively low bending stiffness. It will be shown in the next section that the bending stiffness of these joints makes a limitation for the active control authority, because it shifts the transmission zeros which decreases the closed-loop performance (a similar behaviour was observed with the vibration isolator in the previous chapter).

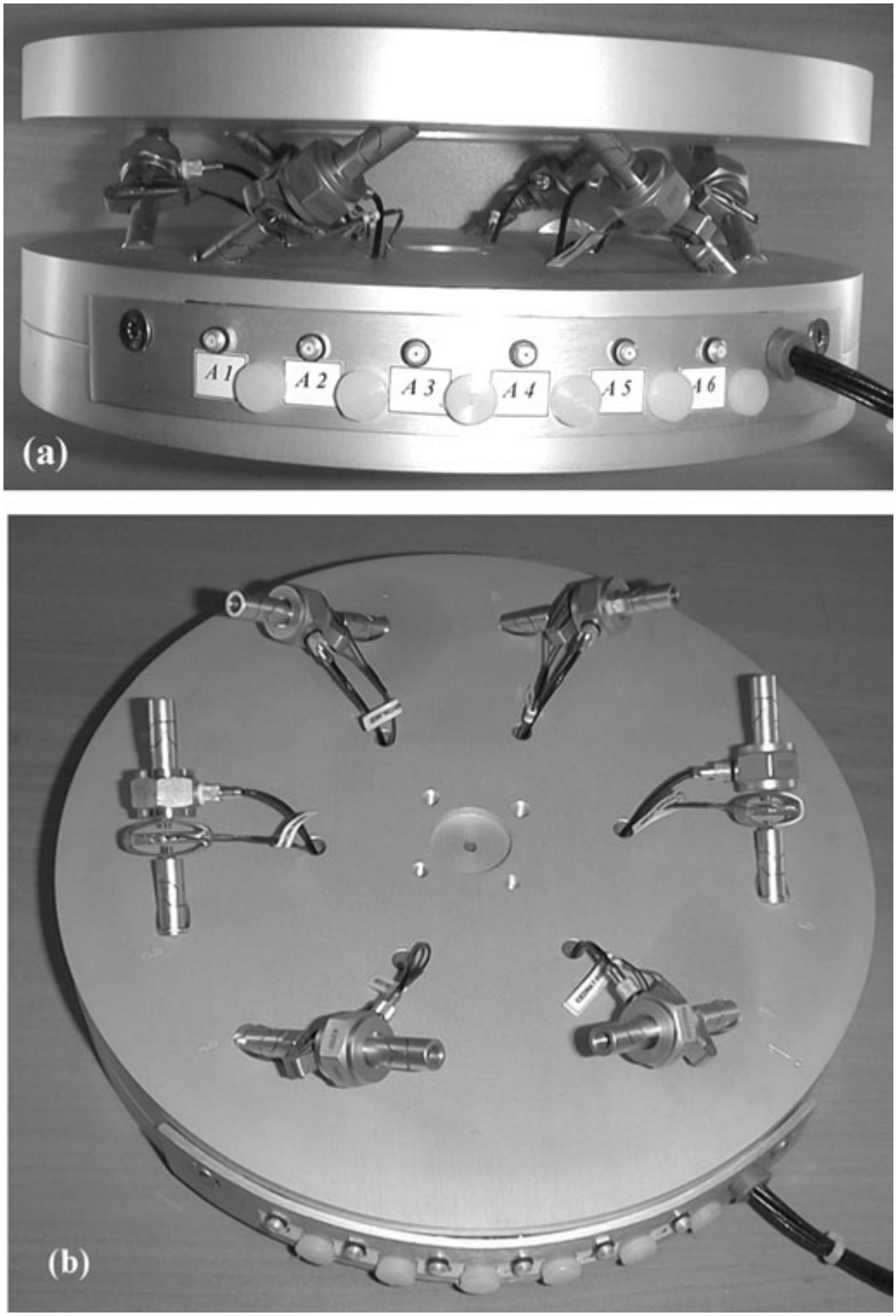

Figure 4.16: *The stiff Stewart platform (ULB design); (a) complete hexapod, (b) the hexapod with the upper plate removed*

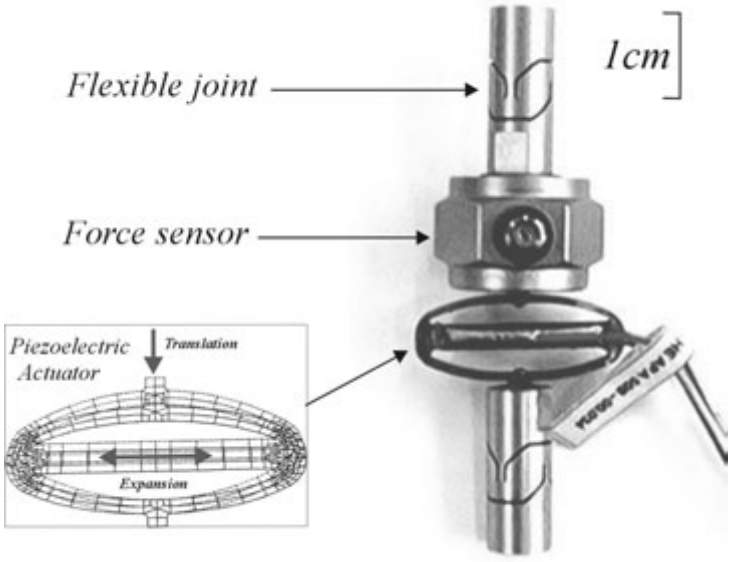

Figure 4.17: *The active leg of the stiff Stewart platform (ULB design)*

4.8 Governing equations

Consider the piezoelectric hexapod integrated in a structure and let M and K be the mass and stiffness matrices of the global passive system (structure + hexapod). Including the equivalent piezoelectric forces, the dynamic equation governing the system reads

$$Ms^2x + Kx = Bk\delta \tag{4.23}$$

where B is the force Jacobian matrix, k is the axial stiffness of the leg and $\delta = (\delta_1, ..., \delta_6)^T$ is the vector of the 6 unconstraint displacements of the piezoelectric actuators; $k\delta$ represents the equivalent piezoelectric force in the leg as expressed in Equ.(4.1). As explained before, there is a force sensor located in each leg of the hexapod and collocated with the actuator. The corresponding output equation reads

$$y = k(q - \delta) \tag{4.24}$$

where $y = (y_1, ..., y_6)^T$ is the 6 force sensor outputs and $q = (q_1, ..., q_6)^T$ is the vector of leg extensions from the equilibrium position. Taking into account the relationship between the leg extensions and the payload frame displacements; $q = B^Tx$, the output equation become:

$$y = k(B^Tx - \delta) \tag{4.25}$$

Using the decentralized IFF with constant gain g, the control law is:

$$\delta = \frac{g}{ks} y \tag{4.26}$$

(note here that this is a positive feedback). This leads to the closed-loop equation of motion:

$$[Ms^2 + K - \frac{g}{g+s} BkB^T]x = 0 \tag{4.27}$$

The contribution of the hexapod to the general stiffness matrix of the system, K, includes the axial stiffness k of the legs and also some bending stiffness due to the flexible tips connecting the legs to the base plates. Without this parasitic stiffness, the transmission zeros of the system, ω_i (the asymptotic solution of the closed-loop equation, Equ.(4.27), as $g \to \infty$) would be located at the origin (removing one leg would produce a mechanism). With the bending stiffness due to the flexible tips, these transmission zeros will be moved away from the origin; there will be no more rigid body modes to appear when the axial stiffness of the legs is removed. The zeros are the solution of the eigenvalue problem $[Ms^2 + K - BkB^T]x = 0$ corresponding to the axial stiffness of the leg being removed from K.
To transform Equ.(4.27) into modal coordinates, one substitutes $x = \Phi z$ and, assuming that the mode shapes are normalized according to $\Phi^T M \Phi = I$ and that $\Phi^T K \Phi = \Omega^2$, Equ.(4.27) becomes:

$$[s^2 + \Omega^2 - \frac{g}{g+s} \Phi^T BkB^T \Phi]z = 0 \tag{4.28}$$

From the analysis explained more deeply in [2] we have:

$$\Phi^T (BkB^T)\Phi \approx diag(\nu_i \Omega_i^2) \tag{4.29}$$

where ν_i is the fraction of modal strain energy in the active legs when the structure vibrates according to mode i. As in section 4.2, the frequencies of the transmission zeros can be denoted as:

$$\omega_i^2 = \Omega_i^2 (1 - \nu_i) \tag{4.30}$$

and the characteristic equation can be written similarly as:

$$s^2 + \Omega_i^2 - \frac{g}{g+s}(\Omega_i^2 - \omega_i^2) = 0 \tag{4.31}$$

or

$$1 + g \frac{(s^2 + \omega_i^2)}{s(s^2 + \Omega_i^2)} = 0 \tag{4.32}$$

4.9 Applications of the piezoelectric Stewart platform

4.9.1 High precision pointing device

An interesting application for the piezoelectric Stewart platform is positioning with high resolution; such a device can be used for the purpose of fine pointing of optics, telescopes and other precision devices [21, 22]. The kinematics of the hexapod has been discussed in details in chapter 3 and appendix A.
The maximum stroke of the piezoelectric actuator used in our design is $55\mu m$; for symmetric operation, an offset voltage is applied so that the actual stroke is $\pm 27.5\mu m$. Following the discussion of section 3.4.2, table 4.2 shows the maximum pure translations and rotations in the different degrees of freedom. δq_i is the elongation in the i^{th} leg given in μm and $\delta\chi$ are the maximum pure translations (in μm) and rotations (in μrad) travelled by the center of the upper plate (see Fig.3.3 for reference axes and strut numbering).

$\delta\chi$	δq_1	δq_2	δq_3	δq_4	δq_5	δq_6
$x_{pure} = 33.7$	13.75	13.75	-27.5	13.75	13.75	-27.5
$y_{pure} = 38.9$	27.5	-27.5	0	27.5	-27.5	0
$z_{pure} = 47.5$	27.5	27.5	27.5	27.5	27.5	27.5
$\theta^x_{pure} = 498$	0	0	27.5	27.5	-27.5	-27.5
$\theta^y_{pure} = 431$	-27.5	-27.5	13.75	13.75	13.75	13.75
$\theta^z_{pure} = 350$	27.5	-27.5	27.5	-27.5	27.5	-27.5

Table 4.2: *Maximum pure translations (in μm) and rotations (in μrad) travelled by the mobile plate and the corresponding leg configuration (see Fig.3.3 for reference axes and strut numbering)*

When the motion is a combination of several directions, a numerical technique is used to calculate the different configurations that give the maximum motions in the six d.o.f. of the platform. The maximum translations (in μm) and rotations (in μrad) and the corresponding leg configurations are shown in table 4.3. Note that the maximum motions shown in this table are not pure motions but they are coupled with other motions at the same time.

$\delta\chi$	δq_1	δq_2	δq_3	δq_4	δq_5	δq_6
$x_{max} = 45$	-27.5	-27.5	-27.5	27.5	27.5	-27.5
$y_{max} = 51.5$	27.5	-27.5	-27.5	27.5	-27.5	27.5
$z_{max} = 47.5$	27.5	27.5	27.5	27.5	27.5	27.5
$\theta^x_{max} = 650$	-27.5	27.5	27.5	27.5	-27.5	-27.5
$\theta^y_{max} = 575$	-27.5	-27.5	-27.5	27.5	27.5	-27.5
$\theta^z_{max} = 350$	27.5	-27.5	27.5	-27.5	27.5	-27.5

Table 4.3: *Maximum coupled translations (in μm) and rotations (in μrad) travelled by the mobile plate and the corresponding leg configuration (see Fig.3.3 for reference axes and strut numbering)*

The signal to noise ratio of commercial power electronics for piezo actuators is about 80

dB [23]. As the position noise is linearly proportional to the electrical noise, the resolution of piezoelectric actuator is about 0.01% of its stroke. In present case, the piezo noise for a $55\mu m$ stroke actuator should be $5.5nm_{rms}$. As the pointing commands in the hexapod are transferred into motion of the upper plate, the noise is transferred too. To find the RMS values of the noise on the platform, we can use

$$\delta x_i = \sqrt{\sum_j (J_{ij}^{-1})^2 \delta q_j^2} \tag{4.33}$$

where δx_i is the transferred noise in the i^{th} direction of motion of the platform, δq_j is the noise produced by the actuator in the j^{th} leg and J_{ij} is the Jacobian value relating them ($\delta q_j = J_{ij}\delta x_i$). Table 4.4 gives the resolution of the platform in the six degrees of freedom.

δx_i	Resolution
x_{noise}	4.5 nm_{rms}
y_{noise}	5.2 nm_{rms}
z_{noise}	3.9 nm_{rms}
θ^x_{noise}	66.4 $nrad_{rms}$
θ^y_{noise}	57.5 $nrad_{rms}$
θ^z_{noise}	28.7 $nrad_{rms}$

Table 4.4: *Resolution of the six degrees of freedom of the platform*

4.9.2 Active damping interface

The test set-up consists of mounting the truss of Fig.4.1 on the upper plate of the hexapod (Fig.4.18). The active struts of the truss are not used in this experiment; the aim is to introduce active damping to the flexible modes of the structure using only the elongation of the legs of the Stewart platform. The mode shapes of the global system are shown in Fig.4.19; the modal fraction of strain energy (computed from finite element results) is given in table 4.5. ν_i is the sum of modal fractions of strain energy in the six legs of the hexapod when the structure vibrates according to the i^{th} mode. Except for mode 3, all these values are fairly large, which should result in high control authority of the active damping.

A decentralized IFF control has been implemented on a DSP board with identical gains for all loops. Figure 4.20 shows experimental results in time history; it shows the signal of one of the force sensors located in the legs, in the following sequence of events: (i) an impulse load is applied to the passive structure, we then observe the free response in the open-loop, (ii) the control is switched on and we observe the free response in closed-loop.

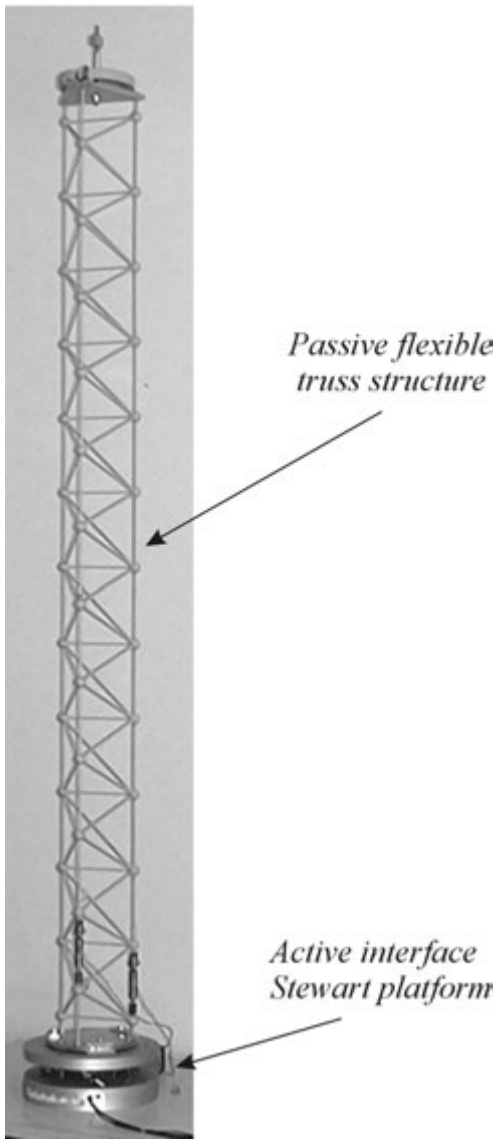

Figure 4.18: *Passive truss mounted on the active damping interface*

mode	Frequency	ν_i
1	3.82 Hz	65.2 %
2	4.21 Hz	56.7 %
3	45.35 Hz	2.7 %
4	65.62 Hz	14.9 %
5	78.97 Hz	14 %
6	87.44 Hz	68 %

Table 4.5: *Modal fraction of strain energy in the hexapod legs corresponding to the first six modes of the structure*

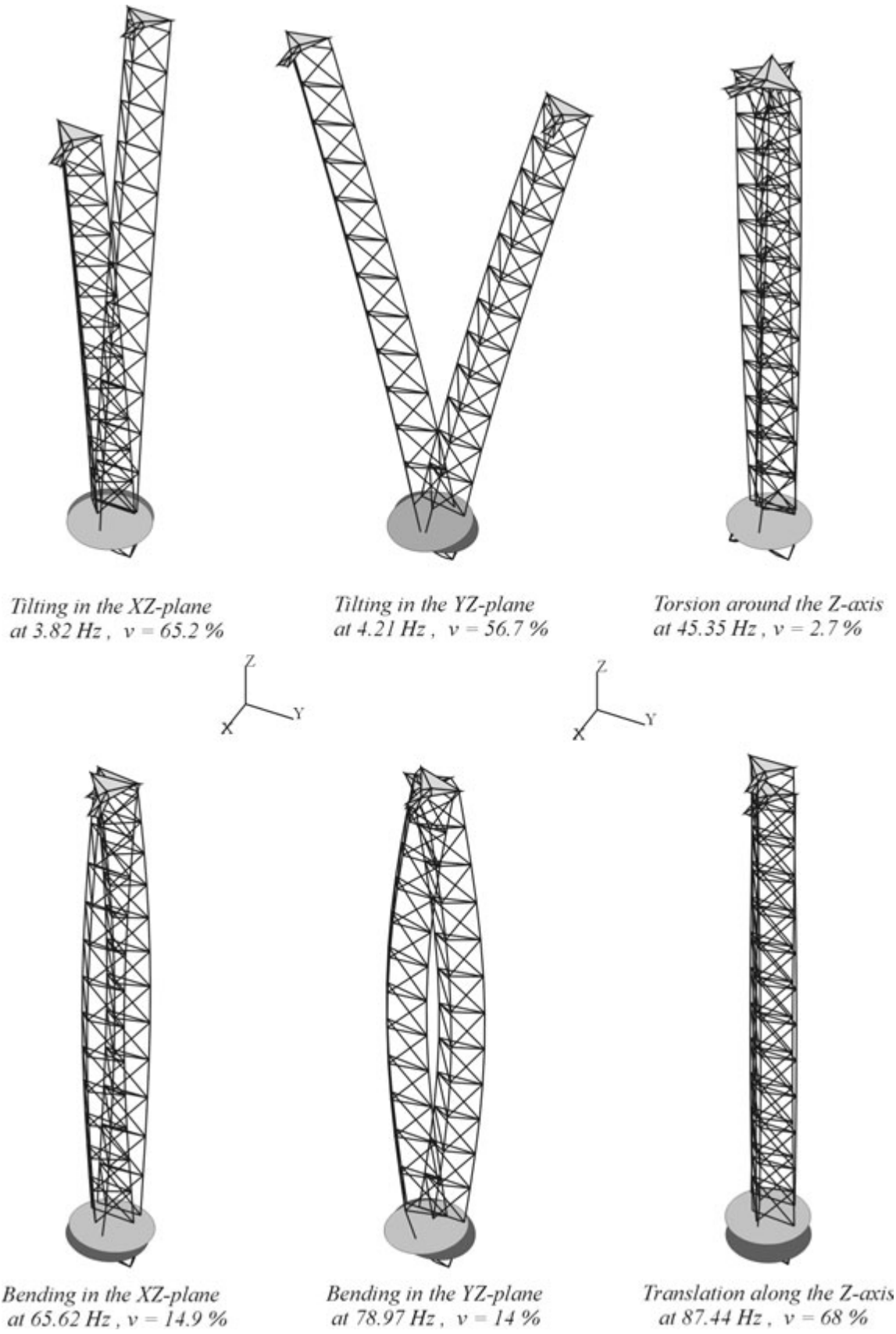

Figure 4.19: *Mode shapes of the test structure (finite element calculations)*

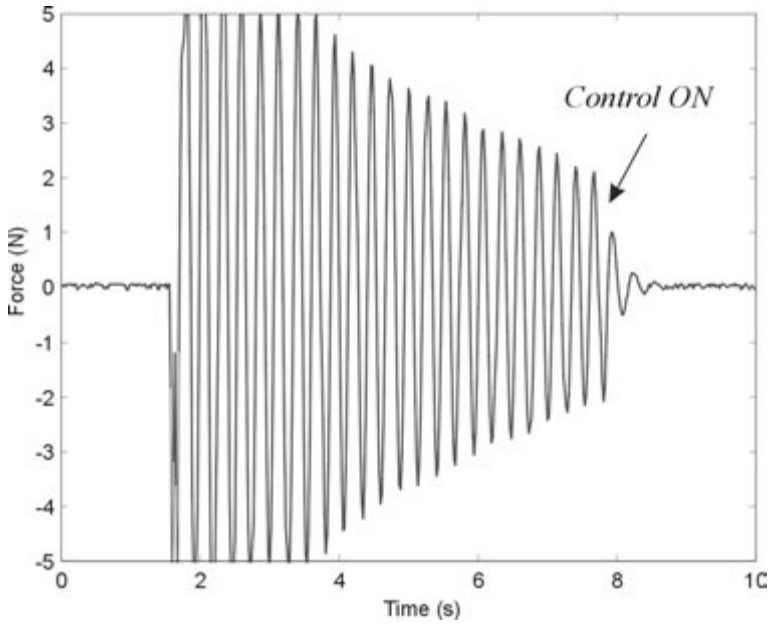

Figure 4.20: *Time response with and without control for impulse excitation*

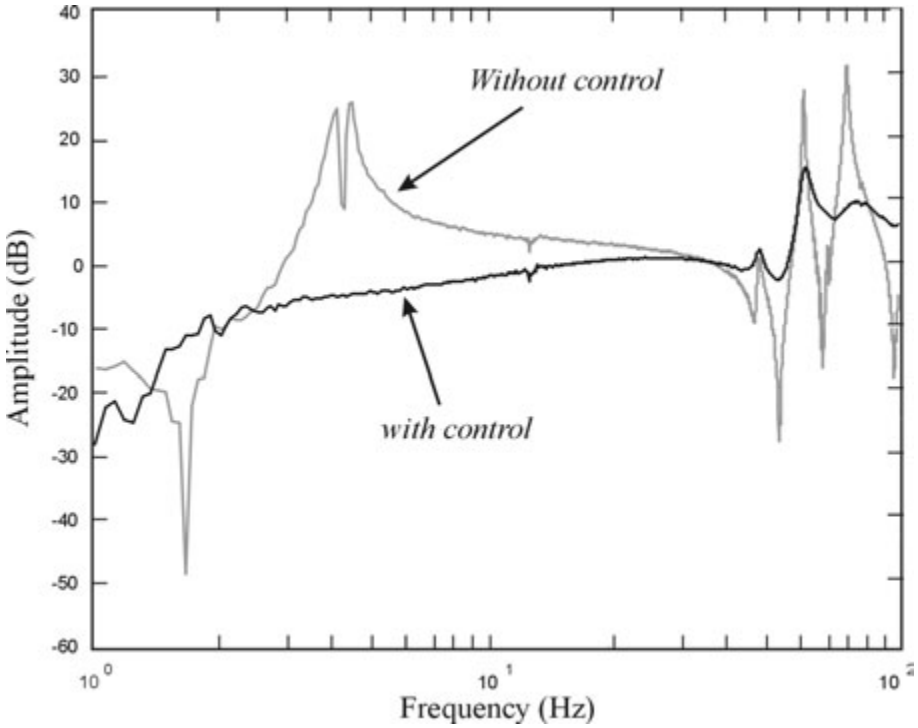

Figure 4.21: *FRF between the voltage input to the actuator and the signal output of the force sensor in one of the legs*

The FRFs, with and without control, shown in Fig.4.21 are obtained between the perturbation signal applied to the piezo actuator of one leg and the signal of its collocated force sensor. One can see that fairly high damping ratios can be achieved for the low frequency modes (4-5 Hz) but also a significant damping is obtained for the high frequency modes (40-90 Hz). As expected from table 4.5, the control influence on the torsion mode is limited. An additional contribution to the lack of damping is the bending stiffness of the flexible tips. The experimental root locus for the first two modes is shown in Fig.4.22 and is compared to the estimated theoretical root locus from Equ.(4.32); Ω_i and ω_i are the resonance and transmission zeros of the experimental FRF, respectively. ω_i have been found, experimentally, as the asymptotic values of the closed-loop poles when the gain $g \to \infty$.

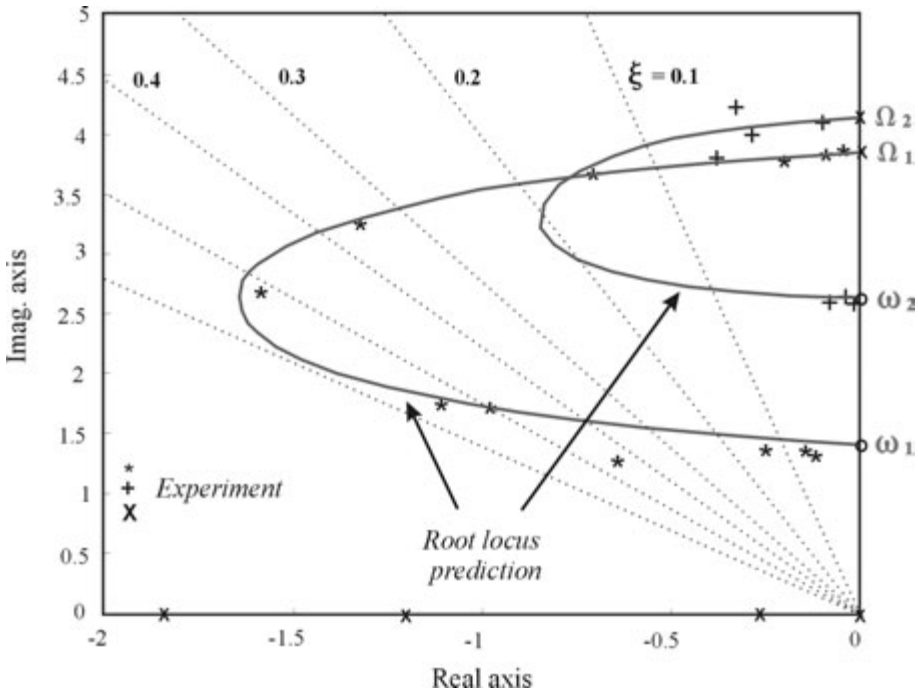

Figure 4.22: *Experimental root locus compared to the theoretical estimation*

4.10 References

[1] A. Preumont, J.-P. Dufour, and C. Malekian. Active damping by a local force feedback with piezoelectric actuators. *AIAA, J. Guidance, Control and Dynamics*, 15(2):390–395, March-April 1992.

[2] A. Preumont. *Vibration Control of Active Structures*. Kluwer Academic Publishers, Netherlands, 2nd edition, 2002.

[3] A. Preumont and Y. Achkire. Active damping of structures with guy cables. *AIAA Journal of Guidance, Control and Dynamics*, 20(2):320–326, March-April 1997.

[4] A. Preumont, Y. Achkire, and F. Bossens. Active tendon control of large trusses. *AIAA Journal*, 38(3), March 2000.

[5] A. Preumont and F. Bossens. Active tendon control of vibration of truss structure. *Journal of Intelligent Materials Systems and Structures*, 2(11):91–99, February 2000.

[6] J. Holterman. *Vibration Control of High-Precision Machines with Active Structural Element*. PhD thesis, Twente University, The Netherlands, 2002.

[7] Y. Achkire. *Active Tendon Control of Cable-Stayed Bridges*. PhD thesis, Université Libre de Beuxelles, Brussels, Belgium, 1996-1997.

[8] F. Bossens. *Amortissement actif des structures cablées: de la théorie à l'implémentation*. PhD thesis, Université Libre de Bruxelles, Brussels, Belgium, October 2001.

[9] F. Bossens and A. Preumont. Active tendon control of cable-stayed bridges. *Earthquake Engineering and Structural Dynamics*, 30:961–979, 2001.

[10] Z. Geng and L. Haynes. Six degrees-of-freedom active vibration control using the Stewart platforms. *IEEE Transactions on Control Systems Technology*, 2(1):45–53, March 1994.

[11] A. Abu Hanieh, A. Preumont, and N. Loix. Piezoelectric Stewart platform for general purpose active damping and precision control. In *9th European Space Mechanism and Tribology Symposium*, Liege, Belgium, September 2001.

[12] A. Abu Hanieh, M. Horodinca, A. Preumont, N. Loix, and J.Ph. Verschueren. Stiff and soft Stewart platforms for active damping and active isolation of vibrations. In *Actuator 2002*, Bremen, Germany, June 2002.

[13] A. Abu Hanieh, A. Preumont, and N. Loix. Six-axis active damping and precision pointing interface based on a Stewart platform. *Computing and Control Engineering Journal of the IEE*, accepted in October 2002.

[14] N. Loix, A. Abu Hanieh, and A. Preumont. Piezoelectric Stewart platform for general purpose active damping interface and precision control. In *3rd International Conference of the European Society for Precision Engineering and Nanotechnology*, Euspen, Eindhoven, The Netherlands, May 2002.

[15] A. Abu Hanieh, M. Horodinca, and A. Preumont. Six-degrees-of-freedom parallel robots for active damping and active isolation of vibrations. In *1st Conference: Model Experiment Interactions in Solid Mechanics*, Besançon, France, July 2002. Published in *Journal de Physique* .

[16] Micromega Dynamics. http://www.micromega-dynamics.com.

[17] CSA Engineering. Internet. Http://www.csaengineering.com, January 2001.

[18] B. Petitjean and D. Lebihan. Robust control of a satellite truss structure. In *ICAST '99*, volume 117, Paris, October 1999.

[19] A. Defendini, L. Vaillon, F. Trouve, Th. Rouze, B. Sanctorum, G. Griseri, and M. Von Alerti. Technology predevelopment for active control of vibration and very high accuracy pointing system.

[20] Physik Instruments. *Physik Instruments catalogue*.

[21] R. Gloess. Hexapod parallel kinematics with sub-micrometer accuracy. In *International Conference on New Actuators*, volume 15, Bremen, Germany, June 2000.

[22] B. Wada, Z. Rahman, and R. Kedikian. Vibration isolation, suppression, steering, and pointing (VISSP). In *Proc. Conference on Spacecraft Structures, Materials and Mechanical Testing*, volume 15, Noordwijk, The Netherlands, March 1996.

[23] Cedrat Recherche. Cedrat, electrical engineering catalogue, 2000.

Chapter 5

Conclusions and future work

5.1 Summary and conclusions

Chapter 1 introduces the motivation of this research and the applications on ground as well as in space. Vibration isolation objectives are discussed, in general, and some isolation architectures are shown. Active damping of structures is introduced here showing the possibility to use the piezoelectric Stewart platform as an active damping interface between truss structures.

Chapter 2 discusses single-axis systems using soft actuators. After a brief review of the passive isolation, various active control techniques are discussed, showing the robustness of the integral force feedback over the sky-hook damper when the isolated body is flexible relative to the isolation mount. The stability of the IFF controller for an isolator connecting arbitrary flexible structures has been established. Two other techniques of vibration isolation have been discussed: using seismometers and using intermediate passive mount.

Chapter 3 addresses the general problem of six degrees of freedom vibration isolation. The architecture and characteristics of the Stewart platform are discussed and the advantages of the cubic architecture are stressed. After a review of on-going projects in foreign teams, the detailed design of ULB Stewart platform is described and the contribution of the various components to the performance of the global system is discussed. The flexible joints connecting the legs to the base plates are pointed out as particularly important, because they control the open-loop zeros of the system. Also, the eddy currents in the voice coil holder should be minimized in order to maximize the high frequency decay rate of the isolator. A finite element model of the Stewart platform has been developed, using the technique of super elements; this leads to a small size model which can be integrated in a global model.

Chapter 3 also reports on the microgravity tests performed in parabolic flight; two controllers have been used: Lag-Lead and IFF, the latter has guaranteed stability, it also performs better. The test campaign was sucessful, although, it clearly points out the need to improve the lateral dynamics of the legs in order to improve the isolation performance.

Chapter 4 is devoted to stiff systems with pizeoelectric legs. The damping properties of the active strut is first reviewed; it consists of a piezoelectric actuator collocated with a force sensor and controlled according to positive IFF; several applications are discussed. Next, various on-going projects using stiff Stewart platform are reviewed and the ULB design is described in details. The use of the platform as active damping interface is demonstrated sucessfully.

In this research, two Stewart platforms have been designed, manufactured and tested by the author; a *soft* Stewart platform (chapter 3) with voice coil actuators for the purpose of active isolation of vibrations and a *stiff* Stewart platform (chapter 4) with piezoelectric actuators for the purposes of active damping and precision pointing.

The major conclusions regarding *soft* Stewart platforms are:

- They can be used efficiently for vibration isolation purposes.
- The corner frequency of the soft hexapod should be as low as possible and the modal spread should be minimized.
- The design of the flexible joints has a great effect on the control authority and the isolation performance.
- The lateral dynamics of the legs deteriorate the high frequency isolation performance of the isolator.

As far as *stiff* Stewart platforms are concerned, the main conclusions are as follows:

- They can be used for vibration damping and precision pointing purposes.
- The damping performance is very good and can be predicted by a simple root locus technique.
- Using an hexapod with piezoelectric actuators, combined damping and positioning is feasible.
- The concept can be easily scaled up and down, and a family of active damping interfaces can be developed, that can be used to assemble elementary passive trusses into highly damped large space structures.

5.2 Future work

This study points out the following avenues to improve the performance of the six d.o.f. isolator:

1. A redesign of the flexible joints between the legs and the support plates, in order to reduce their parasitic stiffness and keep the open-loop zeros close to the origin while keeping the axial stiffness and the overall strength needed during the launch of the spacecraft. The use of superelastic material in the joint seems to be an attractive option.

2. Improving the lateral dynamics of the legs: the resonance peaks of the lateral modes can be moved to higher frequency by reducing and redistributing the inertia along the leg. Also, the membranes play a key role in the leg behaviour and their shape and distance should be optimized to combine low axial stiffness with high frequency lateral modes. On the other hand, the damping of the lateral modes should be improved without adding damping to the axial motion of the leg. Fitting a tuned-mass damper on the lateral modes of the legs should be examined.

As far as the system with piezoelectric actuators is concerned, the control strategy is simple robust, very effective and the closed-loop performances are easily predictible. It seems that this technology is ready to be used in precision engineering. For space applications, more studies are needed at system level, to investigate how modular structures can be assembled with standard joints imbedding this technology. Achieving integrated modular electronics is also an issue.

Appendix A

Jacobian of the Stewart platform

In this appendix, we will use different notations from those used in the text of chapter 3 for clarity reasons and to follow those used in the robotics community [1]. To estimate the Jacobian matrix that relates the elongation of the legs of the Stewart platform to the motion of the platform, let us consider the vectorial representation of the hexapod shown in Fig.A.1.

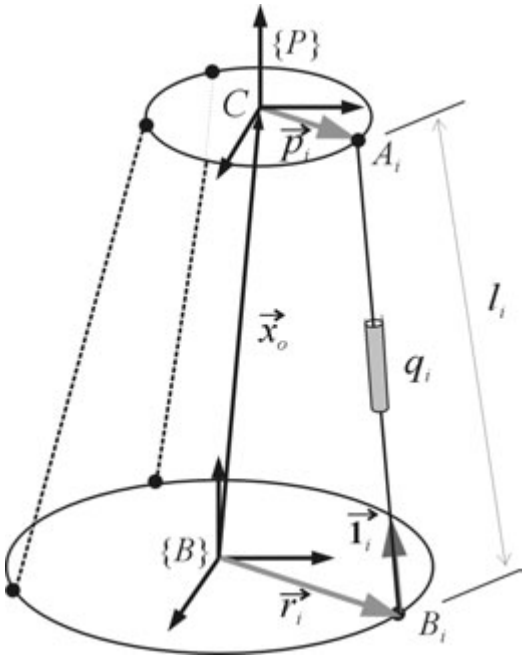

Figure A.1: *Vectorial representation of the Stewart platform*

$\{B\} \equiv$ inertial reference frame of the lower platform (assumed fixed).
$\{P\} \equiv$ reference frame at the center of mass C of the upper platform.
$\vec{\mathbf{r}}_i \equiv$ position of the extremity of leg i in the lower platform.
$\vec{\mathbf{p}}_i \equiv$ position of the extremity of leg i in the upper platform.
$\vec{\mathbf{x}}_o \equiv$ The vector connecting the origin of $\{B\}$ to that of $\{P\}$

$\vec{\mathbf{1}}_i \equiv$ Unit vector along leg i.
R is the rotation matrix relating $\{P\}$ to $\{B\}$, defined for example in terms of *roll/pitch/yaw* angles: $\boldsymbol{\theta}= (\gamma, \beta, \alpha)^T$.
The relationship between $\{B\}$ and $\{P\}$ is completely defined by $\mathbf{x}_o$ and $\boldsymbol{\theta}$; the Jacobian J relates the elongation velocities of the legs, $\dot{q}_i$, to the velocity vector $\dot{\boldsymbol{\chi}} = (\mathbf{v}^T, \boldsymbol{\omega}^T)^T$, where $\mathbf{v} = \dot{\mathbf{x}}_o$ and $\boldsymbol{\omega} = \dot{\boldsymbol{\theta}}$.

$$\dot{\mathbf{q}} = J\dot{\boldsymbol{\chi}} \tag{A.1}$$

The analytical expression can be obtained by expressing the absolute velocity $\vec{\mathbf{v}}_i$ of the extremity A_i (the extremity B_i is fixed in the inertial reference frame $\{B\}$), and projecting it along $\vec{\mathbf{1}}_i$, we get

$$\vec{\mathbf{v}}_i = \vec{\mathbf{v}} + \vec{\boldsymbol{\omega}} \times \vec{\mathbf{p}}_i$$

where $\vec{\mathbf{v}}$ is the absolute velocity of C and $\vec{\boldsymbol{\omega}}$ is the angular velocity of the upper plate.

$$\dot{q}_i = \vec{\mathbf{1}}_i \cdot (\vec{\mathbf{v}} + \vec{\boldsymbol{\omega}} \times \vec{\mathbf{p}}_i)$$

$$\dot{q}_i = \vec{\mathbf{1}}_i \cdot \vec{\mathbf{v}} - \vec{\mathbf{1}}_i \cdot \vec{\mathbf{p}}_i \times \vec{\boldsymbol{\omega}}$$

and, upon projecting in the appropriate reference frame,

$$\dot{q}_i = \mathbf{1}_i^T \mathbf{v} - \mathbf{1}_i^T \tilde{\mathbf{p}}_i \boldsymbol{\omega}$$

where we have used the antisymmetric matrix $\tilde{\mathbf{p}}_i$ to express the cross product :
$\mathbf{p}_i \times \boldsymbol{\omega} = \tilde{\mathbf{p}}_i \, \boldsymbol{\omega}$.
The above equation constitute the i^{th} line of the Jacobian:

$$\dot{\mathbf{q}} = J\dot{\boldsymbol{\chi}} = \begin{pmatrix} \cdots & \cdots \\ \mathbf{1}_i^T & -\mathbf{1}_i^T \tilde{\mathbf{p}}_i \\ \cdots & \cdots \end{pmatrix} \begin{pmatrix} \mathbf{v} \\ \boldsymbol{\omega} \end{pmatrix} \tag{A.2}$$

The right side of the equation can be expressed either in the inertial reference frame $\{B\}$ or in the reference frame of the upper platform $\{P\}$. If $\mathbf{v}$ and $\boldsymbol{\omega}$ are expressed in the moving frame $\{P\}$,

$$\mathbf{1}_i = \frac{1}{l_i}[R^T(\mathbf{x}_o - \mathbf{r}_i) + \mathbf{p}_i]$$

where it has been assumed that $\mathbf{x}_o$ and $\mathbf{r}_i$ are expressed in $\{B\}$. It follows that

$$-\mathbf{1}_i^T \tilde{\mathbf{p}}_i = -\frac{1}{l_i}(\mathbf{x}_o - \mathbf{r}_i)^T R \tilde{\mathbf{p}}_i$$

The velocity Jacobian matrix becomes

$$J = \begin{pmatrix} \cdots & \cdots \\ \frac{1}{l_i}[(\mathbf{x}_o - \mathbf{r}_i)^T R + \mathbf{p}_i^T] & -\frac{1}{l_i}(\mathbf{x}_o - \mathbf{r}_i)^T R \tilde{\mathbf{p}}_i \\ \cdots & \cdots \end{pmatrix} \tag{A.3}$$

The force Jacobian can be obtained from the virtual work theorem,

$$\mathbf{f}^T \delta\mathbf{q} = \mathbf{f}^T J \delta\boldsymbol{\chi} = (\mathbf{F}^T, \mathbf{T}^T)\delta\boldsymbol{\chi}$$

where $\mathbf{f}$ stands for the forces along the legs of the platform and $\mathbf{F}$ and $\mathbf{T}$ are respectively the resultant force and the resultant torque applied to the upper platform. It follows that $\mathbf{F}$ and $\mathbf{T}$, expressed in the same reference frame as $\mathbf{v}$ and $\boldsymbol{\omega}$, are related to the forces acting in the leg $\mathbf{f}$ by:

$$\begin{pmatrix} \mathbf{F} \\ \mathbf{T} \end{pmatrix} = B\mathbf{f} \tag{A.4}$$

where $B = J^T$ is the force Jacobian and equals to:

$$B = \begin{pmatrix} \cdots & \mathbf{1}_i & \cdots \\ \cdots & \tilde{\mathbf{p}}_i \mathbf{1}_i & \cdots \end{pmatrix} \tag{A.5}$$

or in more details

$$B = \begin{pmatrix} \cdots & \frac{1}{l_i}[R^T(\mathbf{x}_o - \mathbf{r}_i) + \mathbf{p}_i] & \cdots \\ \cdots & \frac{1}{l_i}\tilde{\mathbf{p}}_i R^T(\mathbf{x}_o - \mathbf{r}_i) & \cdots \end{pmatrix} \tag{A.6}$$

To calculate the general stiffness matrix of the platform, assuming that the only stiffness exists here is the axial stiffness k of the leg. Equ.(A.4) gives

$$\begin{pmatrix} \mathbf{F} \\ \mathbf{T} \end{pmatrix} = B\mathbf{f} = Bk\delta\mathbf{q} \tag{A.7}$$

where $\delta\mathbf{q}$ is the elongation of the legs. From Equ.(A.1) we know that $\delta\mathbf{q} = J\delta\boldsymbol{\chi} = B^T\delta\boldsymbol{\chi}$, then

$$\begin{pmatrix} \mathbf{F} \\ \mathbf{T} \end{pmatrix} = [BkB^T]\delta\boldsymbol{\chi} \tag{A.8}$$

This leads to conclude that the general stiffness matrix of the Stewart platform can be found from the expression: $[BkB^T]$. This expression assumes that the joints at the end of the leg behave perfectly, i.e have a zero bending stiffness. Further readings about the kinematics of the hexapods can be found in [2, 3, 4, 5].

A.1 References

[1] J. Craig. *Introduction to Robotics.* Addison-Wisley, 1986.

[2] J P Merlet. *Les Robots Paralleles.* Hermes, 2nd edition, 1997.

[3] J. McInroy, J. O'Brien, and G. Neat. Precise, fault-tolerant pointing using a Stewart platform. *IEEE/ASME Transactions on mechatronics*, 4:91–95, March 1999.

[4] J. McInroy, G. Neat, and J. O'Brien. A robotic approach to fault-tolerant, precision pointing. *IEEE Robotics and Automation Magazine*, pages 24–37, December 1999.

[5] C. Reboulet and T. Berthomieu. Dynamic models of a six degree of freedom parallel manipulators. *IEEE*, pages 1153–1157, 1991.

Appendix B

Geophones

B.1 Design of the geophone

The basic principle of the geophone depends mainly on the production of a voltage in a coil when a magnet is passed though it. One configuration of the conventional geophones consists of a cylindrical magnet coaxial with a cylindrical coil as shown in Fig.B.1. In this configuration, the coil is wound around a nonconductive cylinder to avoid the effect of the eddy current that can be caused by the current induced in the coil. The wire forming the coil is made up of a good conducting material like copper. The diameter of this wire and the dimensions of the holding cylinder are designed according to the application. The internal core is a permanent magnet selected to give the highest possible magnetic field density B to maximize the induced voltage in the coil. The coil is attached to the casing of the geophone by means of leaf springs (membranes); these springs are designed so as to maintain alignment in the motion of the coil relative to the magnet keeping the lowest stiffness possible in order to have a low resonant frequency for the geophone. For commercial products of geophones, there are many providers [1, 2]
The reverse configuration is also possible (Fig.B.2); using a coil fixed to the casing while the moving mass is the permanent magnet. Since the mass of the magnet is heavier than that of the coil; this configuration leads to a lower natural frequency, but the moving part is larger and heavier.

B.2 Modelling of the geophone

Geophone can be considered as a velocity sensor. No matter whether the proof-mass is the coil or the magnet, one can model the instrument as shown in Fig.B.3.

Assume modelling a moving coil inertial sensor, the coil and the cylindrical holder are represented by the proof-mass m which is mounted to the casing by means of a spring and a damper. The governing equation of motion in Laplace transform for this system is:

$$ms^2x + Cs(x - y) + K(x - y) = 0 \tag{B.1}$$

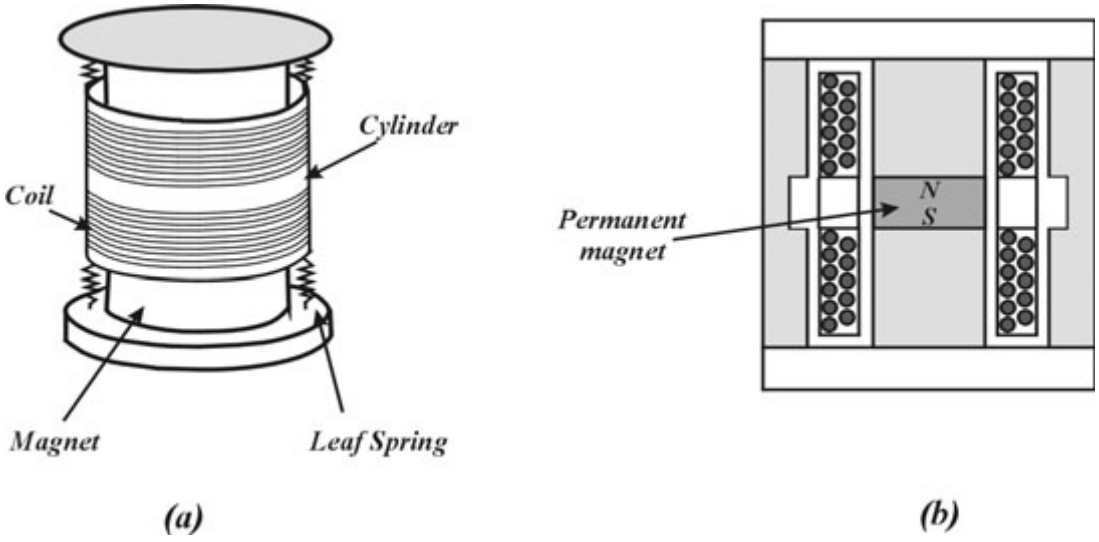

Figure B.1: *Schematic view of a geophone [3], (a) The installation of the coil and springs. (b): A cross-section of the geophone*

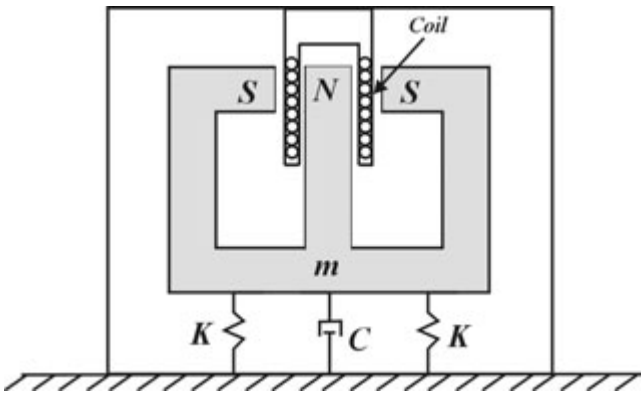

Figure B.2: *A moving magnet seismometer*

Where x and y are the absolute displacements of the proof-mass and the casing, respectively. Using the relative displacement of the proof-mass with respect to the casing $z = (x - y)$, the equation of motion becomes:

$$ms^2z + Csz + Kz = -ms^2y \tag{B.2}$$

From the electromagnetic theory [4, 5], we know that the induced voltage V is related linearly to the relative velocity $\dot{z}$ by the relation:

$$V = Gsz \tag{B.3}$$

Substituting the voltage instead of the relative velocity in Equ.(B.2) gives:

$$ms^2V + CsV + KV = -Gms^3y \tag{B.4}$$

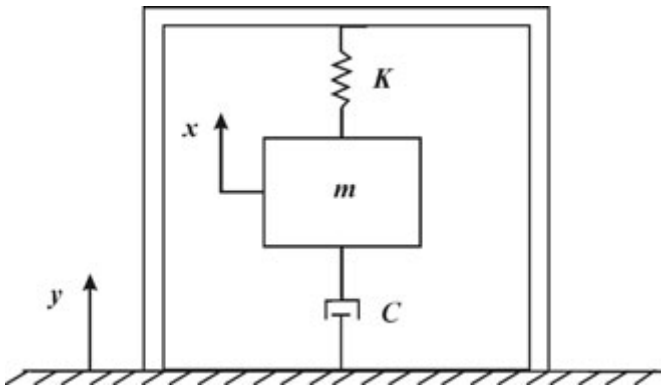

Figure B.3: *A simplified model for the seismometer*

Knowing that the casing of the geophone is fixed to the vibrating body, the relation between the absolute velocity of the casing $\dot{y}$ and the induced voltage in the coil V is given by:

$$G(s) = \frac{V}{\dot{y}} = -G\frac{s^2}{s^2 + 2\xi_g\omega_g s + \omega_g^2} \tag{B.5}$$

Equ.(B.5) expresses the open-loop transfer function of the geophone which senses the absolute velocity of the vibrating body $\dot{y}$ and induces a voltage V in the coil. Here $\omega_g = \sqrt{K/m}$ is the natural frequency of the seismometer, $\xi_g = C/2m\omega_g$ is the damping ratio including the effect of the eddy current and $G = Bl$ is the transduction constant, where B is the magnetic field density generated by the permanent magnet and l is the length of the coil. The transfer function in Equ.(B.5) is plotted in the frequency domain in Fig.B.4. This bode plot shows that the amplitude ratio at low frequency is very small and it becomes unity above the resonance frequency (behaviour of high-pass filter).

B.3 Sensitivity of the geophones

Equ.(B.5) gives the ratio between the output voltage and the velocity of the vibrating body. This relation yields the ratio between the relative velocity $\dot{z}$ and the absolute velocity of the casing $\dot{y}$. Dividing Equ.(B.5) by ω_g^2 and substituting $V = G\dot{z}$, we get:

$$\frac{\dot{z}}{\dot{y}} = \frac{z}{y} = \frac{(s/\omega_g)^2}{(s/\omega_g)^2 + 2\xi_g(s/\omega_g) + 1} \tag{B.6}$$

At high frequencies (above the natural frequency), since $z = -y$, the relative motion of the seismic mass must be the same as that of the vibration to be measured. When the natural frequency ω_g of this instrument is low in comparison to the vibration frequency s, the ratio s/ω_g approaches to a large number and the relative displacement z approaches to y regardless of the value of the damping ratio ξ_g, the mass m then remains stationary while the supporting case moves with the vibrating body. The relative motion is converted

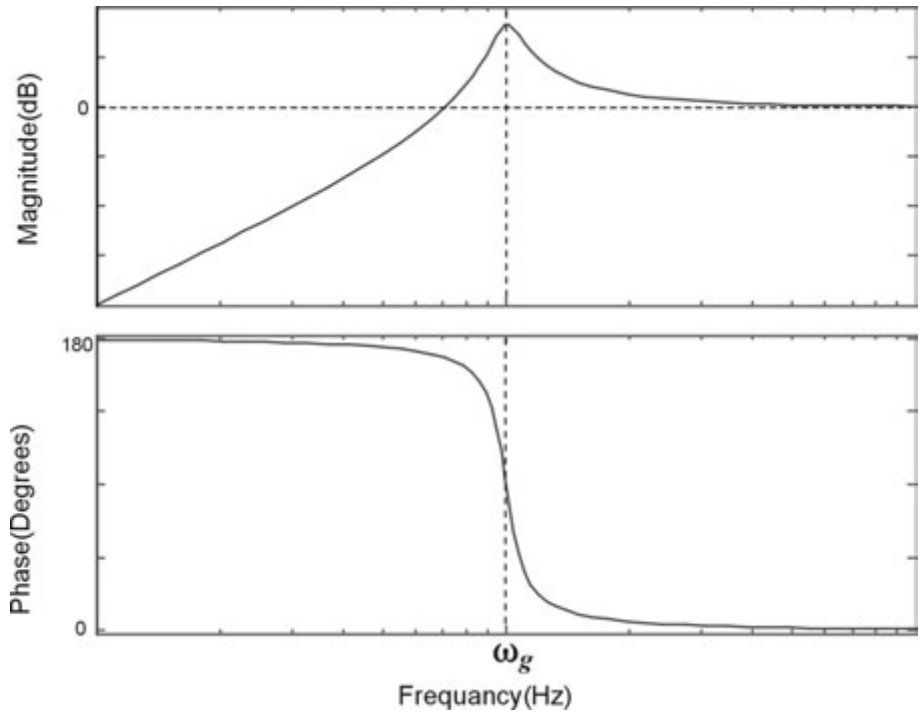

Figure B.4: *The open-loop bode plot for the geophone*

to an electric voltage either by making the seismic mass as a magnet moving relative to the coil or vice versa. Since the generated voltage is proportional to the rate of crossing of the magnetic field, the output of the instrument will be proportional to the velocity of the vibrating body. A typical instrument of this kind may have a natural frequency between 1 Hz to 5 Hz. The sensitivity of such instrument may be in the range of 2 V/ms^{-1} to 3.5 V/ms^{-1} with the maximum displacement limited to about 5 mm peak to peak [6]. When a geophone is used to measure vibrations with a frequency below its natural frequency, the proof-mass tends to follow the motion of the vibrating body rather than staying stationary. This motion of the proof-mass following the casing reduces the relative motion which in turn reduces the induced voltage. Here the sensitivity of the sensor (ratio between the voltage and the casing velocity) becomes very small which restricts the performance of the sensor and limits the range of usage of the instrument to frequencies above its corner frequency. It is important to mention that both displacement and acceleration can be obtained from the velocity sensor (seismometer) by means of the integrator provided in most of the signal conditioner units.

B.4 References

[1] Geospace. Geospace geophones. http://www.geospacelp.com, 2000.

[2] Mark Products. Mark geophones. http://psn.quake.net/geophone/, 2000.

[3] A. Barzilai. *Improving a Geophone to Produce an Affordable, Broadband Seismometer.* PhD thesis, Stanford University, USA, June 2000.

[4] J. Edminister. *Schaum's Theory and Problems, "Electromagnetics"*. Schaum's Outline Series. McGraw-Hill, Inc., 1993 .

[5] J. Kraus. *Electromagnetics*. Electrical Engineering Series. McGraw-Hill, International editions, 4th edition, 1992.

[6] W. Thomson. *Theory of Vibration with Applications*. George Allen and Unwin, 1981.

General Bibliography

[1] A. Abu Hanieh, M. Horodinca, and A. Preumont. Six-degree-of-freedom hexapods for active damping and active isolation of vibrations. *Journal de Physique*, 12(Pr11-41), December 2002.

[2] A. Abu Hanieh, M. Horodinca, and A. Preumont. Six-degrees-of-freedom parallel robots for active damping and active isolation of vibrations. In *1st Conference: Model Experiment Interactions in Solid Mechanics*, Besançon, France, July 2002. Published in *Journal de Physique* .

[3] A. Abu Hanieh, M. Horodinca, and A. Preumont. A soft-actuator active hexapod for the purpose of vibration isolation. In *International Conference on Noise and Vibration Engineering*, KUL, Leuven, Belgium, September 2002.

[4] A. Abu Hanieh, M. Horodinca, A. Preumont, N. Loix, and J.Ph. Verschueren. Stiff and soft Stewart platforms for active damping and active isolation of vibrations. In *Actuator 2002*, Bremen, Germany, June 2002.

[5] A. Abu Hanieh, A. Preumont, and N. Loix. Piezoelectric Stewart platform for general purpose active damping and precision control. In *9th European Space Mechanism and Tribology Symposium*, Liege, Belgium, September 2001.

[6] A. Abu Hanieh, A. Preumont, and N. Loix. Six-axis active damping and precision pointing interface based on Stewart platform. In *Inter Active 2001 Online Conference (Active Control of Sound and Vibration)*, Southampton, UK, November 2001.

[7] A. Abu Hanieh, A. Preumont, and N. Loix. Six-axis active damping and precision pointing interface based on a Stewart platform. *Computing and Control Engineering Journal of the IEE*, accepted in October 2002.

[8] Y. Achkire. *Active Tendon Control of Cable-Stayed Bridges*. PhD thesis, Université Libre de Beuxelles, Brussels, Belgium, 1996-1997.

[9] W. Anderson, N. Groom, and C. Woolley. Annular suspension and pointing system. *AIAA, J. Guidance and Control*, 2(5):367–373, September-October 1979.

[10] L. Baron and J. Angeles. The kinematic decoupling of parallel manipulators using joint-sensor data. *IEEE Transactions on Robotics and Automation*, 16(6):644–651, December 2000.

[11] A. Barzilai. *Improving a Geophone to Produce an Affordable, Broadband Seismometer*. PhD thesis, Stanford University, USA, June 2000.

[12] C. Blanche, A. Fontanet, and P. Lombard. *Cours de Magnetisme*. Cedrat Recherche, 2000.

[13] I. Bonev and J. Ryu. A new method for solving the direct kinematics of general 6-6 Stewart platforms using three linear extra sensors. *Mechanism and Machine Theory*, 35:423–436, 2000.

[14] F. Bossens. *Amortissement actif des structures cablées: de la théorie à l'implémentation.* PhD thesis, Université Libre de Bruxelles, Brussels, Belgium, October 2001.

[15] F. Bossens and A. Preumont. Active tendon control of cable-stayed bridges. *Earthquake Engineering and Structural Dynamics*, 30:961–979, 2001.

[16] K. Bouanane and R. Fenton. Kinematic analysis of parallel manipulators. In *3rd International Workshope on Adnvances in Robot Kinematics*, Italy, September 1992.

[17] Bruel and Kjaer. Bruel and kjaer catalogue of shakers. Bruel and Kjaer, 1992.

[18] K. Cappel. Six degrees of freedom. In *Mechanical Engineering Magazine*, page 6. November 2002.

[19] R.M. Chalasani. Ride performance potential of active suspension systems - PART 1: Simplified analysis based on a quarter-car model. In *Symposium on Simulation and Control of Ground Vehicles and Transportation Systems*, pages 187–204. ASME, December 1986.

[20] Y. Chen and J. McInroy. Identification and decoupling control of flexure jointed hexapods. In *International Conference on Robotics and Automation*, San Francisco, April 2000.

[21] S.B. Choi, H.K. Lee, and E.G. Chang. Field test results of a semi-active ER suspension system associated with skyhook controller. In *Mechatronics*, pages 345–353. Elsevier Science Ltd., 2001.

[22] K. Cleary and T. Arai. A prototype parallel manipulator: Kinematics, construction, software, workspace results and singularity analysis. In *Proceedings of the 1991 IEEE, International Conference on Robotics and Automation*, pages 566–571, Sacramento, California, April 1991.

[23] S.A. Collins and A.H. von Flotow. Active vibration isolation for spacecraft. In *42nd Congress of the International Astronautical Federation*, volume IAF-91-289, Montreal, Canada, October 1991.

[24] BARRY Controls. *Isolator selection guide.*

[25] TECH Products Corporation. *Vibration and noise control products.*

[26] J. Craig. *Introduction to Robotics.* Addison-Wisley, 1986.

[27] C. Crede. *Vibration and shock isolation.* John Wiley and Sons Inc., New York, 1951.

[28] A. Darby. Modeling and control of a felxible structure incorporating inertial slip-stick actuator. *Journal of Guidance, Control and Dynamics*, 22(1):36–42, January-February 1999.

[29] B. Dasgupta and T. Mruthyunjaya. Closed-form dynamic equations of the general Stewart platform through the Newton-Euler approach. *Mech. Mach. Theory*, 33(7):993–1012, 1998.

[30] B. Dasgupta and T. Mruthyunjaya. A Newton-Euler formulation for the inverse

dynamics of the Stewart platform manipulator. *Mach. Mach. Theory*, 33(8):1135–1152, 1998.

[31] B. Dasgupta and T. Mruthyunjaya. The Stewart platform manipulator: A review. *Mach. Mach. Theory*, 35:15–40, 2000.

[32] A. Defendini, L. Vaillon, F. Trouve, Th. Rouze, B. Sanctorum, G. Griseri, and M. Von Alerti. Technology predevelopment for active control of vibration and very high accuracy pointing system.

[33] BEI-Kimco Magnetic Division. Voice coil actuators and applications guide. BEI technologies Inc., 1998.

[34] Micromega Dynamics. http://www.micromega-dynamics.com.

[35] D. Edberg and B. Wilson. Design and testing of reduced-stiffness umbilicals for space station microgravity isolation. *Journal of Spacecraft and Rockets*, 38(4):563–568, August 2001.

[36] J. Edminister. *Schaum's Theory and Problems, "Electromagnetics"*. Schaum's Outline Series. McGraw-Hill, Inc., 1993 .

[37] M.M. El-Madany and M.I. Al-Majed. Quadratic synthesis of active controls for a quarter-car model. *Journal of Vibration and Control*, 7:1237–1252, 2001.

[38] A. El-Sinawi and R. Kashani. Active isolation using Kalman estimator-based controller. *Journal of Vibration and Control*, 7, May 2001.

[39] S. Elliott, L. Benassi, M. Brennan, P. Gardonio, and X. Huang. A mobility analysis of active isolation systems with absolute velocity or integrated force feedback. Technical Report 02/01, University of Southampton, Institute of Sound and Vibration Research, Signal Processing and Control Group (ISVR), January, 2002.

[40] CSA Engineering. Internet. Http://www.csaengineering.com, January 2001.

[41] J. Fochage, T. Davis, J. Sullivan, T. Hoffman, and A. Das. Hybrid active/passive actuator for spacecraft vibration isolation and suppression. *SPIE*, 2865:104–122, March 1996.

[42] A. Fouille. *Electrotechnique a I'usage Des Ingenieurs*. Dunod, Paris, 1961.

[43] P. Galeone, R. Trucco, F. Pepe, and L. Genovese. The hexapod pointing system. In *ESA Symposium Proceedings on "Space Station Utilisation", ESOC*, volume 118, pages 643–646, Darmstadt, Germany, September-October 1996.

[44] W. Gawronski. *Dynamics and Control of Structures, A Modal Approach*. Springer-Verlag, New York, 1998.

[45] Z. Geng and L. Haynes. Six-degree-of-freedom active vibration isolation using a Stewart platform mechanism. *Journal of Robotic Systems*, 10(5):725–744, 1993.

[46] Z. Geng and L. Haynes. Six degrees-of-freedom active vibration control using the Stewart platforms. *IEEE Transactions on Control Systems Technology*, 2(1):45–53, March 1994.

[47] Geospace. Geospace geophones. http://www.geospacelp.com, 2000.

[48] R. Gloess. Hexapod parallel kinematics with sub-micrometer accuracy. In *International Conference on New Actuators*, volume 15, Bremen, Germany, June 2000.

[49] GMT. *Gummi-Metal-Technik catalogue*.

[50] C. Gosselin. Determination of the workspace of 6-DOF parallel manipulators. *Journal of Mechanical Design*, 112:331–336, September 1990.

[51] V.E. Gough and S.G. Whitehall. Universal tyre testing machine. *Proc. Ninth International Technical Congress F.I.S.I.T.A.*, 117, May 1962.

[52] D. Grant and V. Hayward. Vibration isolation with high strain shape memory alloys; actuators: Case of the impulse disturbance. http://www.citeseer.nj.com/289361.html.

[53] C.M. Grodsinsky and M. Whorton. Survey of active vibration isolation systems for microgravity applications. *Journal of Spacecraft and Rockets*, 37(5):586–596, September-October 2000.

[54] C. Hartwig, H. Haase, M. Hofmann, and H-J. Karkosch. Electromagnetic actuators for active engine vibration cancellation. In *International Conference on New Actuators*, Bremen, Germany, June 2000.

[55] G. Hauge and M. Campbell. Shaping the transmissibility for six-axis active vibration isolators. *AIAA*, 1287, 1999.

[56] J. Holterman. *Vibration Control of High-Precision Machines with Active Structural Element*. PhD thesis, Twente University, The Netherlands, 2002.

[57] M. Horodinca, A. Abu Hanieh, and A. Preumont. A soft six degrees of freedom active vibration isolator based on Stewart platform. In *International Symposium on Active Control of Sound and Vibration (Active 2002)*, Southampton, UK, July 2002.

[58] M.H. Hsiao, E.J. Haug JR., and J.S. Arora. A state space method for optimal design of vibration isolators. *Journal of Mechanical Design*, 101:309–313, April 1979.

[59] A. Huba. Mechatronic vibration isolator for the microtechnics with real-time interaction. http://www.citeseer.nj.nec.com/355140.html.

[60] P.C. Hughes and T.M. Abdel-Rahman. Stability of proprtional-plus-derivative-plus-integral control of flexible spacecraft. *Journal of guidance and control*, 2(6):499–503, November-December 1979.

[61] M. Husty. An algorithm for solving the direct kinematic of Stewart-Gough-type platforms. In *CIM94*, volume 14, Montreal, Canada, June 1994.

[62] T. Hyde and E. Anderson. Actuator with built-in viscous damping for isolation and structural control. *AIAA Journal*, 34(1):129–135, January 1996.

[63] Physik Instruments. *Physik Instruments catalogue*.

[64] C.E. Kaplow and J.R. Velman. Active local vibration isolation applied to a flexible space telescope. *AIAA J. Guidance and Control*, 3(3):227–233, May-June 1980.

[65] A. Karger. Classification of all self-motions of the original Stewart-Gough platform. *Computer Aided Design*, 30(3):205–215, 1998.

[66] D. Karnopp, M.J. Crospy, and R.A. Harwood. Vibration control using semi-active force generators. *Trans. of ASME, Journal of Engineering for Industry*, pages 619–629, May 1974.

[67] D. Karnopp and A.K. Trikha. Comparative study of optimization techniques for shock and vibration isolation. *Trans. of ASME, Journal of Engineering for Industry*, pages 1128–1132, November 1969.

[68] C. Keckler. ASPS preformance with large payloads onboard shuttle orbiter. *AIAA, J. Guidance*, 5(1):32–36, January-February 1979.

[69] K.Y. Kim and Y.P. Park. Robust vibration control of air-spring isolation table. In *MOVIC 2000*, Sydney, Australia, December 2000.

[70] Y.S. Kim, K.W. Wang, and H.S. Lee. Structural vibration suppression via adaptable damping and stiffness. In *ADPA/AIAA/ASME/SPIE Conf. On Active Materials and Adaptive Structures*, pages 473–478. IOP Publishers Ltd., 1992.

[71] J. Kraus. *Electromagnetics*. Electrical Engineering Series. McGraw-Hill, International editions, 4th edition, 1992.

[72] G. Kuo, G-S. Chen, P. Pham, and B. Wada. On-orbit system identification using active members. *AIAA*, 1129-CP, 1990.

[73] R. Laskin and S. Sirlin. Future payload isolation and pointing system technology. *AIAA, J. Guidance and Control*, 9(4):469–477, July-August 1986.

[74] N. Loix, A. Abu Hanieh, and A. Preumont. Piezoelectric Stewart platform for general purpose active damping interface and precision control. In *3rd International Conference of the European Society for Precision Engineering and Nanotechnology*, Euspen, Eindhoven, The Netherlands, May 2002.

[75] N. Loix and A. Preumont. Remarks on the modelling of active structures with collocated piezo electric actuators and sensors. In *ASME Conference on Mechanical Vibration and Noise*, Boston, September 1995.

[76] C. Luh, F. Adkins, E. Haug, and C. Qiu. Working capability analysis of Stewart platforms. *Transactions of the ASME*, 118:220–227, June 1996.

[77] O. Ma and J. Angeles. Optimum architecture design of platform manipulators. *IEEE*, 1991.

[78] Bakker Magnetics. Catalogue de matriaux magnetiques permanents. Bakker Magnetics (BM).

[79] G. D. Martin. *On the Control of Flexible Mechanical Systems*. PhD thesis, Stanford University, 1978.

[80] J. McInroy. Dynamic modeling of flexure jointed hexapods for control purposes. In *Proceedings of the 1999 IEEE International Conference on Control Applications*, pages 508–513, Kohala Coast-Island of Hawaii, USA, August 1999.

[81] J. McInroy. Modeling and design of flexure jointed Stewart platforms for control purposes. *IEEE/ASME Transactions on Mechatronics*, 7(1), March 2002.

[82] J. McInroy and J. Hamann. Design and control of flexure jointed hexapods. *IEEE Transaction on Robotics*, 16(4):372–381, August 2000.

[83] J. McInroy, G. Neat, and J. O'Brien. A robotic approach to fault-tolerant, precision pointing. *IEEE Robotics and Automation Magazine*, pages 24–37, December 1999.

[84] J. McInroy, J. O'Brien, and G. Neat. Precise, fault-tolerant pointing using a Stewart

platform. *IEEE/ASME Transactions on mechatronics*, 4:91–95, March 1999.

[85] J.-P. Merlet. An algorithm for the forward kinematics of general parallel manipulators. *IEEE*, pages 1136–1140, 1991.

[86] J P Merlet. *Les Robots Paralleles*. Hermes, 2nd edition, 1997.

[87] J. Moerschell. *Micropositioning Course*. Swiss Foundation for Research in Microtechnology, Switzerland, 1999.

[88] P. Nelson. An active vibration isolation system for inertial reference and precision measurement. *Rev. Sci. Instrm, American Institute of Physics.*, 62(9), September 1991.

[89] J. O'Brien, G. Neat, J. Melody, and R. Calvet. Six-axis vibration isolation technology applied to spaceborne interferometers. *IEEE Transaction on Robotics*.

[90] J. Onoda and N. Watanabe. Vibration suppression by variable-stiffness member. *AIAA Journal*, 29(6):977–983, June 1991.

[91] F. Park and J. Kim. Kinematic manipulability of closed chains. In J. Lenarcic and V. Parenti-Castelli, editors, *Recent Advances in Robot Kinematics*, pages 99–108, The Netherlands, 1996. Kluwer Academic Publishers.

[92] PAULSTRA. *Paulstra and Hutchison Catalogue*.

[93] B. Petitjean and D. Lebihan. Robust control of a satellite truss structure. In *ICAST '99*, volume 117, Paris, October 1999.

[94] V. Piefort. *Finite Element Modelling of Piezoelectric Active Structures*. PhD thesis, Université Libre de Beuxelles, Brussels, Belgium, June 2001.

[95] K.H. Pittens and R.P. Podhorodeski. A family of Stewart platforms with optimal dexterity. *Journal of Robotic Systems*, 10(4):463–479, 1993.

[96] V. Portman, B. Sandler, and E. Zahavi. Rigid 6x6 parallel platform for precision 3-d micromanipulation: Theory and design application. *IEEE Transaction on Robotics and Automation*, 16(6):629–643, December 2000.

[97] A. Preumont. Modular payload isolation mounts based on Stewart platforms. Draft report prepared in support of the GSTP proposal, 1999.

[98] A. Preumont. *Vibration Control of Active Structures*. Kluwer Academic Publishers, Netherlands, 2nd edition, 2002.

[99] A. Preumont and Y. Achkire. Active damping of structures with guy cables. *AIAA Journal of Guidance, Control and Dynamics*, 20(2):320–326, March-April 1997.

[100] A. Preumont, Y. Achkire, and F. Bossens. Active tendon control of large trusses. *AIAA Journal*, 38(3), March 2000.

[101] A. Preumont and F. Bossens. Active tendon control of vibration of truss structure. *Journal of Intelligent Materials Systems and Structures*, 2(11):91–99, February 2000.

[102] A. Preumont, J.-P. Dufour, and C. Malekian. Active damping by a local force feedback with piezoelectric actuators. *AIAA, J. Guidance, Control and Dynamics*, 15(2):390–395, March-April 1992.

[103] A. Preumont, J.P. Dufour, and C. Malekian. Active damping by local force feedback

with piezoelectric actuators. In *AIAA/ASME/SDM Conference*, Baltimor, MD, April 1991.

[104] A. Preumont, A. François, F. Bossens, and A. Abu-Hanieh. Force feedback vs. acceleration feedback in active vibration isolation. *Journal of Sound and Vibration*, 257(4), October 2002.

[105] A. Preumont and N. Loix. Some perspectives of applications of active control to large structures. In *International Conference on Motion and Vibration Control (MOVIC2000)*, volume 15, Sydney, Australia, December 2000.

[106] A. Preumont, N. Loix, D. Malaise, and O. Lecrenier. Active damping of optical test benches with acceleration feedback. *Machine Vibration*, 2:119–124, 1993.

[107] Mark Products. Mark geophones. http://psn.quake.net/geophone/, 2000.

[108] Z. Rahman, J. Spanos, and D. Bayard. Multi-tone adaptive vibration isolation of engineering structures. In *36th AIAA/ASME/ASCE/AHS Structures, Structural Dynamics and Materials Conference*, New Orleans, USA, April 1995.

[109] Z. Rahman, J. Spanos, and G. Blackwood. Active narrow-band vibration isolation of large engineering structures. In *Proceedings of the First World Conference on Structural Control*, Pasadena, USA, August 1994.

[110] Z. Rahman, J. Spanos, and R. Laskin. Multi-axis vibration isolation, suppression and steering system for space observational applications. In *SPIE International Symposium on Astronomical Telescopes and Instrumentation*, Kona-Hawaii, March 1998.

[111] C. Reboulet and T. Berthomieu. Dynamic models of a six degree of freedom parallel manipulators. *IEEE*, pages 1153–1157, 1991.

[112] Cedrat Recherche. Cedrat, electrical engineering catalogue, 2000.

[113] Wilcoxon Research. Vibration sensors and instrumentation catalogue. Wilcoxon research, 1993.

[114] E.I. Rivin. Principles and criteria of vibration isolation of machinery. *Trans. of the ASME, Journal of Mechanical Engineering*, 101:682–692, October 1979.

[115] E.I. Rivin. Vibration isolation of precision equipment. In *Precision Engineering*, pages 41–56, New York, 1995. Elsevier Science Inc.

[116] L. Romdhane. Design and analysis of a hybrid serial-parallel manipulator. *Mach. Mach. Theory*, 34:1037–1055, July 1998.

[117] D. Schubert, A. Beard, S. Shedd, M. Earls, and A. von Flotow. Stiff actuator active vibration isolation system. In *United States Patent No. 5,660,255*. August 1997.

[118] A. Simon, A. Collins, H. Andreas, and A. von Flotow. Active vibration isolation for spacecraft. In *42nd Congress of the International Astronautical Federation*, pages Paper No. IAF–91–289, Montreal, Canada, October 1991.

[119] J.A. Snyman, P.S. Heyns, and P.J. Vermeulen. Vibration isolation of a mounted engine through optimization. *Mech. Mach. Theory*, 30(1):109–118, 1995.

[120] J. Spanos. Six axis vibration isolation. *Internet, http://www.jpl.nasa.gov*, 1995.

[121] J. Spanos, Z. Rahman, and G. Blackwood. A soft 6-axis active vibration isolator. In

Proceedings of the American Control Conference, Seattle, Washington, USA, June 1995.

[122] B. St-Onge and C. Gosselin. Singularity analysis and representation of spatial six-dof parallel manipulators. In J. Lenarcic and V. Paranti-Castelli, editors, *Recent Advances in Robot Kinematics*, The Netherlands, 1996. Kluwer Academic Publishers.

[123] D. Stewart. A platform with six degrees of freedom. *Proc. Instn. Mech. Engrs.*, 180(15):371–386, 1965-66.

[124] Y. Su, B. Duan, and C. Zheng. Genetic design of kinematically optimal fine tuning Stewart platform for large spherical radio telescope. *Mechatronics*, 11:821–835, 2001.

[125] C. Taranti, B. Agrawal, and R. Cristi. An efficient algorithm for vibration suppression to meet pointing requirements of optical payloads. *AIAA Guidance, Navigation and Control Conference and Exhibition*, August 2001.

[126] R. Taranti, C. Cristi and B. Agrawal. State-space equations for a high-precision pointing hexapod. *IEEE Conference on Control Applications (CCA)*, 2001.

[127] D. Thayer, M. Kampell, and J. Vagners. Six axis vibration isolation using modern control techniques. In *21st Annual AAS Guidance and Control Conference*, February 1998.

[128] D. Thayer, M. Kampell, J. Vagners, and A. von Flotow. Six axis vibration isolation system using soft actuators and multiple sensors. *Journal of Spacecraft and Rockets*, 39(2), March-April 2002.

[129] D. Thayer, J. Vagners, A. von Flotow, C. Hardham, and K. Scribner. Six-axis vibration isolation system using soft actuator and multiple sensors. *AAS*, 064:497–506, 1998.

[130] W. Thomson. *Theory of Vibration with Applications*. George Allen and Unwin, 1981.

[131] TMC. Technical background. Technical report, Technical Manufacturing Corporation.

[132] D. Trumper and T. Sato. A vibration isolation platform. In *Mechatronics*, pages 281–294. Elsevier Science Ltd., 2002.

[133] L. Tsai. Solving the inverse dynamics of a Stewart-Gough manipulator by the principle of virtual work. *Journal of Mechanical Design*, 122:3–9, March 2000.

[134] P.J. Veitch. Vibration isolation of distributed mechanical oscillators by mechanical suspensions with application to resonant-mass gravitational radiation antennae. *Rev. Sci. Instrum, American Institute of Physics*, 62(1):140–154, January 1991.

[135] B. Wada, Z. Rahman, and R. Kedikian. Vibration isolation, suppression, steering, and pointing (VISSP). In *Proc. Conference on Spacecraft Structures, Materials and Mechanical Testing*, volume 15, Noordwijk, The Netherlands, March 1996.

[136] C. Wampler. Forward displacement analysis of general six-in-parallel SPS (Stewart) platform manipulators using soma coordinates. *Mach. Mach. Theory*, 31(3):331–337, 1996.

[137] J. Watson, H. Bush, W. Heard Jr., M. Lake, J. Jensen, R. Wallsom, and J. Phelps. A mobile transporter concept for EVA assembly of future spacecraft. *AIAA*, 1049-CP, 1990.

[138] J. Yang and Z. Geng. Closed form forward kinematics solution to a class of hexapod robots. *IEEE Transactions on Robotics and Automation*, 14(3):503–508, June 1998.

[139] H. Yoshioka, Y. Takashashi, K. Katayama, T. Imazzawa, and N. Murai. An active microvibration isolation system for hi-tech manufacturing facilities. *Journal of Vibration and Acoustics*, 123:269–275, April 2001.

[140] Y. Yunhe, N.G. Naganathan, and R.V Dukkipati. A literature review of automotive vehicle engine mounting systems. *Mechanism and Machine Theory*, 36, 2001.

[141] C. Zhang and S. Song. Forward position analysis of nearly general Stewart platforms. *Transactions of the ASME*, 116:54–58, March 1994.

View publication stats